Non-orographic gravity waves in ground-based Rayleigh lidar observations

Michael Binder[1] and Andreas Dörnbrack[1]

[1]DLR, Institut für Physik der Atmosphäre

November 8, 2023

Abstract

Temperature measurements by vertically staring ground-based Rayleigh lidars are often used to detect middle atmospheric gravity waves. In time-height diagrams of temperature perturbations, stationary mountain waves are identifiable by horizontal phase lines. Vertically tilted phase lines, on the other hand, indicate that the wave source or the propagation conditions are transient. Idealized numerical simulations illustrate that and how a wave source moving in the direction of the mean wind entails upward-tilted phase lines. The inclination angle depends on the horizontal wavelength and the wave source's propagation speed. On this basis, the goal is to identify and characterize transient non-orographic gravity waves (NOGWs), e.g., from propagating upper-level jet/front systems, in virtual and actual Rayleigh lidar measurements. Compositions of selected atmospheric variables from a meteorological forecast or reanalysis are thoughtfully combined to associate NOGWs with processes in the troposphere and stratosphere. For a virtual observation over the Southern Ocean, upward-tilted phase lines indeed dominate the time-height diagram during the passage of an upper-level trough. The example also emphasizes that temporal filtering of temperature measurements is appropriate for NOGWs, especially in the presence of a strong polar night jet that implies large vertical wavelengths. During two selected observational periods of the COmpact Rayleigh Autonomous Lidar (CORAL) in the lee of the southern Andes, upward-tilted phase lines are mainly associated with mountain waves and transient background wind conditions. One nighttime measurement by CORAL coincides with the passage of an upper-level trough, but large-amplitude mountain waves superpose the small-amplitude NOGWs in the middle atmosphere.

Non-orographic gravity waves in ground-based Rayleigh lidar observations

Michael Binder and Andreas Dörnbrack

Deutsches Zentrum für Luft- und Raumfahrt, Institut für Physik der Atmosphäre, Oberpfaffenhofen, Germany

Weßling, November 5, 2023

Key Points:

- Tilted phase lines in temperature measurements of ground-based Rayleigh lidars can be related to a propagating non-orographic GW source
- Tailored compositions of selected meteorological variables guide the interpretation of virtual and actual Rayleigh lidar measurements
- Temporal filtering of temperature is suitable for identifying NOGWs in observations of vertically staring ground-based Rayleigh lidars

Corresponding author: Michael Binder, `michael.binder@dlr.de`

Abstract

Temperature measurements by vertically staring ground-based Rayleigh lidars are often used to detect middle atmospheric gravity waves. In time-height diagrams of temperature perturbations, stationary mountain waves are identifiable by horizontal phase lines. Vertically tilted phase lines, on the other hand, indicate that the wave source or the propagation conditions are transient. Idealized numerical simulations illustrate that and how a wave source moving in the direction of the mean wind entails upward-tilted phase lines. The inclination angle depends on the horizontal wavelength and the wave source's propagation speed. On this basis, the goal is to identify and characterize transient non-orographic gravity waves (NOGWs), e.g., from propagating upper-level jet/front systems, in virtual and actual Rayleigh lidar measurements. Compositions of selected atmospheric variables from a meteorological forecast or reanalysis are thoughtfully combined to associate NOGWs with processes in the troposphere and stratosphere. For a virtual observation over the Southern Ocean, upward-tilted phase lines indeed dominate the time-height diagram during the passage of an upper-level trough. The example also emphasizes that temporal filtering of temperature measurements is appropriate for NOGWs, especially in the presence of a strong polar night jet that implies large vertical wavelengths. During two selected observational periods of the COmpact Rayleigh Autonomous Lidar (CORAL) in the lee of the southern Andes, upward-tilted phase lines are mainly associated with mountain waves and transient background wind conditions. One nighttime measurement by CORAL coincides with the passage of an upper-level trough, but large-amplitude mountain waves superpose the small-amplitude NOGWs in the middle atmosphere.

Plain Language Summary

Atmospheric gravity waves are vertical oscillations of air parcels similar to the wave motion we can observe at the ocean surface. Vertical oscillations imply fluctuations in the air parcel's temperature, so studying these waves high up in the atmosphere is possible by measuring temperature with dedicated ground-based instruments. Different processes can cause gravity waves. Flow over mountains, for example, excites gravity waves and results in a specific pattern in these ground-based measurements, which differs for transient atmospheric conditions or propagating wave sources. In this context, this study aims to identify waves from propagating wave sources in temperature measurements by comparing the measured data to simulated data from weather models. If the modeled data matches the measurements, the entire weather model dataset is used to investigate the atmospheric processes causing the waves. The approach proved practical for a virtual measurement location over the Southern Ocean, where it was possible to associate wave patterns in the upper atmosphere with propagating weather phenomena in the lower atmosphere. However, interpreting actual measurements near the southern Andes mountains is more challenging. Mountain waves dominate the measurements with larger amplitudes, even in the presence of propagating gravity wave sources.

1 Introduction

Observations of gravity waves in the stratosphere and mesosphere, lower thermosphere (MLT) are sparse. Only a small number of satellite instruments provide temperature measurements in this altitude range applicable for gravity wave detection. For example, the High Resolution Dynamics Limb Sounder (HIRDLS) was only active between 2005 and 2008 (Gille et al., 2008). The Sounding of the Atmosphere using Broadband Emission Radiometry (SABER) is part of the Thermosphere-Ionosphere-Mesosphere Energetics and Dynamics (TIMED) mission and still operational, but only provides continuous measurements for the latitude range 50°N-50°S (Mlynczak, 1997; Ern et al., 2018). Other instruments are the Cross-Track Infrared Sounder (CrIS) on the Suomi National

Polar-Orbiting Partnership (NPP) satellite that launched on October 2011 (Goldberg et al., 2013) or the nadir-sounding Atmospheric Infrared Sounder (AIRS) on board of NASA's Aqua satellite (Hoffmann & Alexander, 2009; Hoffmann et al., 2013; Eckermann et al., 2019; Hindley et al., 2019, 2020). In the case of AIRS, measurements are available globally, but the temporal resolution is coarse, because each location is only observed twice a day. In addition, the instrument is sensitive to just a portion of the GW spectrum due to the so-called observational filter (e.g., Preusse et al., 2002; Alexander et al., 2010). However, high-temporal resolution and high-cadence of observations are potentially important for detecting gravity waves almost continuously and distinguishing whether they are stationary or transient modes, which in turn gives an indication of their sources (e.g., Reichert et al., 2021).

Vertical temperature profiles from ground-based Rayleigh lidars, often displayed in time-height diagrams, are one alternative available on a regular basis providing much higher vertical and temporal resolutions. Such observations, of course, are limited to a single location (point observation) and are possible only under clear skies and often only at night. Commonly, ground-based Rayleigh lidars are used to monitor middle atmospheric gravity wave activity with the aim to estimate the momentum deposition (wave drag) that drives part of the global atmospheric circulation (e.g., N. Kaifler et al., 2020). In many cases, the lidar observations of temperature and the derived temperature perturbations are compared with results from global circulation models (e.g., Le Pichon et al., 2015; Ehard et al., 2018; Strelnikova et al., 2021; Gisinger et al., 2022). Most analyses are carried out in a statistical manner to determine, among other things, mean vertical wavelengths, periods, amplitudes, and the seasonal variability at different sites (e.g., Yamashita et al., 2009; B. Kaifler et al., 2015; Zhao et al., 2017; Chu et al., 2018; Strelnikova et al., 2021; Reichert et al., 2021). Sometimes, the question arises about the actual atmospheric processes leading, for example, to an observed upward or downward phase progression in the time-height diagrams. To this end, we propose a possible, hopefully appropriate, and reasonable basis for identifying non-orographic gravity waves (NOGWs) in these ground-based Rayleigh lidar measurements by advocating specific displays of selected atmospheric variables retrieved from high-resolution numerical weather prediction (NWP) models. These variables are combined into a single composite figure for each available time to provide guidance on possible gravity wave sources and background conditions associated with weather systems.

We introduce and illustrate our approach by means of a case study on NOGWs over the Southern Ocean (Dörnbrack et al., 2022) during the DEEPWAVE campaign 2014 (Fritts et al., 2016). Generally, transient gravity waves can be generated by a multitude of atmospheric processes like deep convection (e.g., Lane et al., 2001), upper-level front/jet systems (e.g., Plougonven & Zhang, 2014), by an unbalanced polar night jet (PNJ, e.g., Dörnbrack et al., 2018), or by sudden pulsations like volcano eruptions (e.g., Wright et al., 2022). Here, Dörnbrack et al. (2022) propose that the stratospheric flow across zonally propagating upper-level troughs excites non-orographic, transient gravity waves like the flow over mountains excites stationary gravity waves. This connection is evident from the nearly simultaneous zonal propagation of Rossby waves over the Southern Oceans with the occurrence of transient gravity waves in the middle atmosphere. Their findings confirm the synoptic analyses of Hendricks et al. (2014) who correlated the baroclinic growth rates in the troposphere with gravity wave-induced stratospheric temperature perturbations near 60°S, also called the stratospheric gravity wave belt.

Far from any orographic gravity wave sources, the area studied by Dörnbrack et al. (2022) over the Southern Ocean south of Australia is ideal for identifying NOGWs. However, no ground-based Rayleigh lidar measurements exist for this or a similar location, so we also use our approach in the context of observations by the Compact Rayleigh Autonomous Lidar (CORAL) for the middle atmosphere (N. Kaifler et al., 2020; B. Kaifler & Kaifler, 2021) in the lee of the Andes in South America. Here, the predominant amplitudes are due to mountain waves excited by the westerly flow over the Andes and characterized by nearly horizontal phase lines in the time-height diagrams, indicating the quasi-steadiness of the stationary mountain waves (Reichert et al., 2021). On the other hand, there are numerous examples where stratospheric phase lines in the time-height diagrams are inclined; see and scroll the daily observations displayed in CORAL's measurement calendar under `http:\\container.kaifler.net/coral/index.php`. The reason for these inclinations can be manifold: transient ambient winds in the troposphere or stratosphere that affect the excitation and propagation conditions of mountain waves are one possibility. Transient gravity wave sources associated with eastward propagating mid-latitude weather systems in the Southern Hemisphere, as introduced above, are another (e.g., Dörnbrack et al., 2022; Plougonven & Zhang, 2014; Hendricks et al., 2014).

Although the idea of the excitation mechanism of NOGWs proposed by Dörnbrack et al. (2022) resembles the excitation of mountain waves, their actual appearance in time-height diagrams of ground-based Rayleigh lidar observations will be significantly different from that of mountain waves. The propagation of the wave source leads to an inclination of the phase lines. Therefore, Section 2 first deals with how transient NOGWs appear in time-height diagrams and how they could be interpreted utilizing idealized numerical simulations. Subsequently, Section 3 applies the conclusions of the previous section and proposes tailored visualizations of tropospheric and stratospheric flow quantities from state-of-the-art numerical weather prediction (NWP) data to identify and interpret NOGWs for a virtual lidar location over the Southern Ocean. We use the recent reanalyses version 5 (ERA5) of the European Centre for Medium-Range Weather Forecasts (ECMWF). ERA5 is computed by the Integrated Forecast System (IFS Cycle 41r2) (Hersbach et al., 2020). The section also discusses the appropriate filtering of temperature measurements from a vertically staring ground-based Rayleigh lidar before moving from the ideal location for investigating NOGWs far from orography to actual measurements in the lee of the southern Andes. Section 4 presents the same analysis for two periods with CORAL measurements showing similar tilted phase line signatures as the idealized simulations, and Section 5 summarizes and concludes this paper.

2 Lidar observations in idealized numerical simulations

A complete characterization of stationary mountain waves by ground-based Rayleigh lidar observations is very demanding (e.g., Strelnikova et al., 2021; Reichert et al., 2021). In a purely steady flow, the horizontal phase velocity of mountain waves vanishes ($c_{px} = 0$) together with the ground-based frequency ($\omega = 0$). As a result, phase lines of temperature perturbations derived from the ground-based Rayleigh lidar observations appear horizontal and only the vertical wavelength λ_z can be derived from the time-height diagrams. There is no information about horizontal scales (e.g., Dörnbrack et al., 2017; Reichert et al., 2021).

Dörnbrack et al. (2017) used idealized numerical simulations to show time-height diagrams of the atmospheric response of uniform flow over individual two-dimensional mountains of different widths. The simulated steady, horizontal phase lines of temperature perturbations recorded in the lee of the mountains resemble those found in many CORAL observations. Here we take a step further and employ an idea and the numerical development introduced by Wedi and Smolarkiewicz (2004); Prusa and Smolarkiewicz (2003). Prusa and Smolarkiewicz presented idealized numerical simulations of a moving frictionless lower boundary surface (such as a flexible membrane) in their numerical model that excites vertically propagating gravity waves. If the wave source propagates uniformly in one direction, the gravity waves have the same properties as stationary mountain waves within the frame of reference that moves with their source.

2.1 Setup and comparison of three different EULAG simulations

Here, results are presented that are simulated with the nonlinear EUlerian/semi-LAGrangian fluid solver (EULAG) applying a similar numerical set-up as in Prusa and Smolarkiewicz (2003). EULAG solves the anelastic set of equations (Lipps & Hemler, 1982) consisting of the momentum equations for the Cartesian velocity components (u, v, w), the thermodynamic equation for the potential temperature perturbation $\Theta' = \Theta - \Theta_0$, and the mass continuity equation in generalized time-dependent coordinates (Prusa & Smolarkiewicz, 2003, Eqs. 4-7). A comprehensive description of the advection scheme is given in P. K. Smolarkiewicz and Margolin (1997, 1998). In addition, EULAG features a robust elliptic solver (P. Smolarkiewicz & Margolin, 1993) and a generalized coordinate formulation that enables grid adaptivity technology (Wedi & Smolarkiewicz, 2004; Prusa et al., 2008; Kühnlein et al., 2012).

The anelastic equations are written such that hydrostatically balanced reference profiles $u_0(z)$, $v_0(z)$, $\rho_0(z)$, $p_0(z)$, and $\Theta_0(z)$ are subtracted from the prognostic variables (Clark, 1977; Lipps & Hemler, 1982). For the idealized simulations presented here, the thermodynamic reference profiles define an isothermal atmosphere with constant stability according to (Bacmeister & Schoeberl, 1989):

$$\begin{aligned} &\Theta_0(z) = \Theta_{00} e^{\frac{z}{H_\Theta}} \quad \text{with} \quad \Theta_{00} = T_{00}\left(\frac{p_0}{p_{00}}\right)^{R/c_p}, \quad \text{and} \quad H_\Theta = \frac{g}{N^2} = \frac{c_p T_{00}}{g}, \\ &\rho_0(z) = \rho_{00} e^{-\frac{z}{H_\rho}} \quad \text{with} \quad H_\rho = \frac{RT_{00}}{g}, \quad \text{and} \\ &p_0(z) = p_{00} e^{-\frac{z}{H_\rho}} \end{aligned} \tag{1}$$

with the Brunt-Väisälä frequency $N = 0.02\,\mathrm{s}^{-1}$, the specific gas constant $R = 287.04\,\mathrm{J\,kg^{-1}\,K^{-1}}$, and the specific heat capacity at constant pressure $c_p = \frac{2}{7} R$. The values at the lower boundary, an isentropic surface of $\Theta_{00} \approx 361\,\mathrm{K}$, are: $T_{00} = 239.39\,\mathrm{K}$, $p_{00} = 235\,\mathrm{hPa}$, and $\rho_{00} = 0.3454\,\mathrm{kg\,m^{-3}}$. These values are characteristic for the stably stratified lower stratosphere at mid-latitudes (Gettelman et al., 2011). The exponential profiles (1) avoid physical restrictions towards higher altitudes and are, thus, well suited for investigating deep gravity wave propagation.

The results of the 3D numerical simulations presented in Figure 1 are initialized with zero potential temperature perturbations Θ' and vertical profiles of the three velocity components $(u_0(z), 0, 0)$. The zonal wind profiles $u(z)$ are either uniform with magnitudes of $u_0 = 20$ or $45\,\mathrm{m\,s^{-1}}$ (purple profiles in Figures 1a and c). In a third simulation, $u_0(z)$ is a superposition of a constant wind with the tropopause and polar night jet streams, whose shapes are both based on a Gaussian distribution:

$$u_{jet}(z) = u_{jet,max} e^{-\frac{1}{2}\left(\frac{z - z_{jet}}{\sigma_{jet}}\right)^2} \tag{2}$$

with a maximum wind speed $u_{jet,max}$ at z_{jet} and a standard deviation σ_{jet}. The tropopause jet is centered at the lower boundary with $\sigma_{jet} = 5\,\mathrm{km}$ and the PNJ is centered at $z_{jet} = 40\,\mathrm{km}$ with $\sigma_{jet} = 13\,\mathrm{km}$ (purple line in Figure 1e).

A time-dependent lower boundary (Prusa et al., 1996; Wedi & Smolarkiewicz, 2004) is implemented to mimic the stratospheric flow across a propagating upper-level trough. The physical idea of this approach was already suggested by Pfister et al. (1993) for convective thermals and has been simulated previously by Prusa and Smolarkiewicz (2003). The shape of the upper-level trough or, more precisely, the shape $z_s(x, t)$ of a frictionless, isentropic surface that dips and rises above the upper-level trough can be approximated by an $1{+}\cos(\frac{\pi}{4L}x)$ shape with the width L. The function $z_s(x, t)$ drops to 0 for $|\frac{x}{4L}| = 1$, so the surrounding field can be set to 0 for $|\frac{x}{4L}| \leq 1$ without sacrificing its continuity and differentiability, an essential prerequisite for the numerically stable implementation of a transient boundary condition in the model. Prusa and Smolarkiewicz

(2003) already used a form of the above cosine function to mimic a moving tropopause fold in simplified 2D simulations with EULAG. Here, we use a different variant:

$$z_s(x,t) = \begin{cases} -\frac{h_m}{16}\left(1+\cos(\frac{\pi}{4L}(x-x_0(t))\right)^4 & \text{for} \quad |\frac{x-x_0(t)}{4L}| < 1 \\ 0 & \text{for} \quad |\frac{x-x_0(t)}{4L}| \geq 1, \end{cases} \qquad (3)$$

where $h_m = 300\,\mathrm{m}$, $x_0(t)$ is the time-dependent center of the undulated lower boundary that moves uniformly with a speed c_{tf}. The quantity $c_{tf} = 0$ for the results in the upper row of Figure 1 and $c_{tf} = 13.88\,\mathrm{m\,s^{-1}}$ for the middle and bottom panels. Similar versions of Equation (3) have already been used for prescribing idealized orography (see, Epifanio & Durran, 2001; Metz & Durran, 2021).

Our idealized simulations start with a flat surface $z_s(x,0) = 0$ and homogeneous horizontal flow instead of initializing the flow field with a potential flow over an already implemented lower boundary $z_s(x,0)$ according to Eq. (3). The amplitude h_m of the lower model surface $z_s(x,t)$ slowly changes for a given period $t_{spinup} = 12$ h by multiplying h_m with $tt^3\left(10 - 15tt + 6tt^2\right)$, where $tt = t/t_{spinup}$ for $t \leq t_{spinup}$ in all numerical simulations. The effect of this transient initialization can be seen in the decreasing height z_s during the first 12 hours in Figure 1(b).

Figure 1 illustrates how a transient gravity wave source alters the inclination of phase lines of gravity wave-induced stratospheric temperature perturbations in time-height diagrams. Measurements of a vertically pointing ground-based lidar are emulated by tracking the vertical temperature profile at $x = 7500\,\mathrm{km}$ in the computational domains. Figure 1(a), (c), and (e) show the wave-induced perturbations in the middle plane of 3D computational domain for three different simulations, Figure 1(b), (d), and (f) show the corresponding time-height diagrams. The first row emulates a mountain wave scenario with a non-propagating obstacle at the lower boundary. After 72 h simulation time, vertically propagating inertia-gravity waves are located above the upside-down mountain and extend downstream (Figure 1(a)). In the corresponding time-height diagram, the phase lines of the mountain waves appear as horizontal stripes whose amplitude is increasing with height until they are numerically damped in the sponge layer starting at $z = 48\,\mathrm{km}$ altitude.

In contrast, phase lines in the time-height diagrams differ significantly for simulations with a moving lower boundary (middle and bottom rows of Figure 1). The phase lines tilt upward for a wave source moving in the same direction as the background wind (Figure 1(d) and (f)). The steepness of the phase lines depends on the vertical wind profile. For an idealized stratospheric wintertime wind profile, the phase lines' angle between 30 and 40 km in the time-height diagram in Figure 1(f) is approximately 10 km over 6-7 h. Due to the presence of the PNJ, the phase lines become steeper above 20 km as the vertical wavelength λ_z is proportional to u/N (Figure 1(e)).

2.2 Derivation of wave properties in time-height diagrams

Do the results of the transient wave source allow for a derivation of horizontal wave properties? Yes and no! Clearly, tilted phase lines enable the quantification of a ground-based period T from the time-height diagram, but linking this period to wave properties depends on the wave source and on the atmospheric background conditions. Multiple phenomena could explain upward-tilted phase lines in ground-based lidar observations, so their interpretation requires additional knowledge on the prevailing atmospheric processes and the synoptic situation. Examples are:

- downward propagating wave packets caused by reflection at turning levels (e.g., Schoeberl, 1985),
- wave breaking in the upper atmosphere exciting secondary waves that travel up and down from their source region (e.g., Dörnbrack et al., 2017; Vadas et al., 2003),

- transient background conditions mainly in the form of a varying wind speed or direction (e.g., Chen et al., 2005, 2007; Portele et al., 2018),
- a gravity wave source moving in the same direction as the background wind as illustrated in Figures 1d and 1f.

For this work, we explore the last possibility and focus on the gravity wave characterization for the simplified case of a constant wind profile shown in Figure 1c and 1d following the terminology and derivations of Gill (1982); Fritts and Alexander (2003); Dörnbrack et al. (2017). To recap, a constant stratification with N was used for all simulations starting at the 361 K isentropic surface simplifying the dispersion relation for Boussinesq flows to

$$\hat{\omega}^2 = N^2 \frac{k^2}{k^2 + m^2} + f^2 \frac{m^2}{k^2 + m^2} \tag{4}$$

with $\hat{\omega}$ being the intrinsic frequency and $f = -1.195\,10^{-4}\,\mathrm{s}^{-1}$ is the Coriolis parameter to consider the influence of Earth's rotation at a latitude of 55°S. A constant background wind leads to a ground-based frequency

$$\omega = \hat{\omega} + uk, \tag{5}$$

and, in addition, Gill (1982) defines the useful aspect ratio

$$\alpha = \frac{\text{vertical scale}}{\text{horizontal scale}} = \frac{\lambda_z}{\lambda_x} = \sqrt{\frac{\hat{\omega}^2 - f^2}{N^2 - \hat{\omega}^2}}, \tag{6}$$

which simplifies the approximation of $\hat{\omega}$ for the relevant hydrostatic rotating wave regime to

$$\hat{\omega}^2 \approx f^2 + N^2\alpha^2. \tag{7}$$

As labeled in Figure 1d, the vertical distance between troughs or ridges in the time-height diagram yields the vertical wavelength $\lambda_z = 9.25\,\mathrm{km}$ and a wavenumber $m = 2\pi/\lambda_z$, the horizontal distance at 40 km altitude provides a period $T = 13.92\,\mathrm{h}$ and ground-based frequency ω. How can this frequency be interpreted? Dörnbrack et al. (2017) clarify that in the presence of a background wind this question can only be answered by consulting further information or by proceeding with assumptions.

For the case of a propagating upper-level trough, we can assume a stationary wave field within a moving reference frame. Then, the tilt of the phase lines within the ground-based lidar observation depends on the propagation speed of the gravity wave source and the horizontal wavelength λ_x. A constant propagation speed c_{tf} leads to $\lambda_x = T{\cdot}c_{tf} = 695\,\mathrm{km}$, which is in the range of wavelengths labeled in the vertical cross-section (Figure 1c) at the same height with $\lambda_x = 525\,\mathrm{km}$ to $712\,\mathrm{km}$. The ratio of λ_z to λ_x gives $\alpha = 0.0133$. The angle ϕ between lines of constant phases and the z-axis is

$$\phi = \tan^{-1}(\frac{\lambda_x}{\lambda_z}) = 89.24°. \tag{8}$$

From Equation (7) $\hat{\omega} \approx 2.92\,10^{-4}\,\mathrm{s}^{-1}$, so $\hat{\omega}$ is of $\mathcal{O}(f)$ and $\hat{\omega} \geq f$, which is in full compliance with the hydrostatic rotating wave regime described by Gill (1982). It follows the intrinsic horizontal group velocity

$$c_{gx} \approx \frac{N^2\alpha}{m\sqrt{f^2 + N^2\alpha^2}} \approx -26.9\,\mathrm{m\,s^{-1}} \tag{9}$$

with a negative m for upward propagating waves and the vertical group velocity

$$c_{gz} \approx -\alpha c_{gx} \approx 0.36\,\mathrm{m\,s^{-1}} \tag{10}$$

Again, this is consistent with inertia-gravity waves in the hydrostatic rotating wave regime, where c_{gx} does not offset the background wind resulting in a downstream propagation of these inertia-gravity waves (e.g., Dörnbrack, 2002). Knowledge of $u = 45\,\mathrm{m\,s^{-1}}$

allows the calculation of $U_{MW} = U - c_{tf} = 31.12\,\mathrm{m\,s^{-1}} > |c_{gx}|$, indicating a downstream propagation of gravity waves relative to the propagating upper-level trough. Considering the superimposed propagation of the wave source, the ground-based group velocity is $c_{Gx} = U + c_{gx} = 18.1\,\mathrm{m\,s^{-1}}$ and according to the above assumptions, the ground-based horizontal phase velocity must be identical to the velocity of the wave source ($c_{Px} = c_{tf}$).

The vertical propagation of the gravity waves is independent of the background wind. According to c_{gz} in Equation (10), it takes approximately 31 hours until the gravity waves reach an altitude of 40 km above z_s, but c_{gz} is very sensitive to the derived horizontal and vertical wavelengths: A $\lambda_x = 525\,\mathrm{km}$ (lower limit based on Figure 1c) with the same λ_z already results in 22.6 hours and higher λ_z further increases c_{gz}. The time-height diagram in Figure 1b confirms these estimates: Maximum amplitudes at 40 km appear roughly 20 to 30 hours after the completed spin-up of the simulation.

3 Lidar observations of non-orographic gravity waves in ERA5

After a first investigation of the phase lines' shapes in time-height sections due to transient gravity wave excitation by means of idealized numerical simulations, the approach presented in this and the following section goes one step further: We attempt to identify patterns of NOGWs from a propagating source in actual ground-based Rayleigh lidar measurements of stratospheric and mesospheric temperatures. To this end, we propose to combine time-height sections that emulate the measurements with a series of meteorological analyses in a single figure utilizing state-of-the-art NWP model data as, e.g., the ERA5 reanalysis dataset (Hersbach et al., 2020). As shown by Gupta et al. (2021); Pahlavan et al. (2023), ERA5 is the first global reanalysis that partially resolves the gravity wave spectrum. Here, the 1-hourly ERA5 analyses on model, pressure, and potential vorticity levels at a horizontal resolution of $0.25° \times 0.25°$ ($\approx 30\,\mathrm{km}$) are used. For the native output grid, this corresponds to a minimum resolved wavelength of about 60 km. However, due to scale-selective hyperdiffusion, the effective minimum physical wavelength will be quite larger (Polichtchouk et al., 2023). ERA5 employs a total of 137 unevenly spaced full model levels. Level spacings above the troposphere vary from about 250 m in the lower stratosphere to about 1500 m near 1 hPa (Ehard et al., 2018). Alternatively, and not used in this study, hourly fields of the IFS high-resolution short-term forecasts and the 6 hourly analyses could be combined to visualize the diurnal cycle of the meteorological fields.

We will discuss selected CORAL measurements in Section 4, but it can be anticipated that the presence of mountain waves due to CORAL's proximity to the Andean Mountain Range complicates the identification of NOGWs. Ideal and best placed to obtain suitable observations of NOGWs would be a lidar station far from any orography. For example, to investigate the origins of the gravity waves found in the stratospheric gravity wave belt around 60°S (e.g., Hendricks et al., 2014; Dörnbrack et al., 2022), a place in the Southern Ocean would be perfect. Though no such instruments exist, it is possible to emulate the measurements of a vertical starring ground-based lidar at such a location with the model data. Since Dörnbrack et al. (2022) documented the spatial and temporal evolution of transient NOGWs over the Southern Ocean during research flight RF25 of the DEEPWAVE campaign 2014, we use their groundwork to determine a virtual lidar location that captures these waves in the respective period. By means of this case study, Section 3a establishes a guideline for retrieving NOGWs in temperature time-height diagrams before Section 3b introduces a composite figure for investigating the meteorological processes leading to the gravity wave signal.

3.1 Gravity wave retrievals in time-height diagrams

In Section 2, potential temperature and temperature perturbations are obtained by subtracting the prescribed vertical ambient profiles of the idealized simulations. This background state is unknown when transitioning to measurements of the real atmosphere. For time-height temperature diagrams from vertically staring ground-based lidars, one must rely on, e.g., the temporal mean temperature or vertical spectral filtering (e.g., Ehard et al., 2015; Strelnikova et al., 2021) to obtain the background state. Data gaps often prevent the application of temporal spectral filtering. Figure 2 illustrates how these different filters considerably alter the appearance of gravity waves, especially NOGWs, in time-height diagrams.

Since the ERA5 dataset is based on ECMWF's IFS, a spectral model, obtaining model fields truncated at a specific spectral resolution is possible. For example, the T21-field only includes wavenumber 21 and smaller, all larger wavenumbers are removed. Following Dörnbrack et al. (2022), we use T21 as the background field and obtain temperature perturbations by subtracting it from the full temperature. This procedure mimics spatial horizontal filtering and is a suitable approach to separate the temperature field into a background state comparable to the background of an idealized simulation and perturbations. Figure 2(a) displays the resulting temperature perturbations for a virtual lidar location in the Southern Ocean at 140°E and 53.75°S. Relatively large amplitudes between the dotted vertical lines stand out because it is the only period with a vertically connected wave signal throughout the stratosphere. The upward tilt of the corresponding phase lines is apparent and we can anticipate that these are NOGWs above an eastward propagating upper-level trough as described by Dörnbrack et al. (2022). Their vertical wavelength is small in the lower stratosphere ($\approx 6\,\mathrm{km}$) and significantly increases towards higher altitudes ($\approx 20\,\mathrm{km}$ above $30\,\mathrm{km}$).

Figure 2(c) now introduces a first filter option that is also reproducible with actual point observations of a vertically starring ground-based Rayleigh lidar. The vertical temperature profile is subtracted by a 12 h running mean, which effectively removes the temperature background but also filters spatially stationary signatures like mountain waves persisting for multiple hours. However, this approach is valuable for investigating transient NOGWs with tilted phase lines in time-height diagrams. The overall wave pattern is similar to the horizontal filtering in Figure 2(a) and the gravity wave between the dotted lines is captured throughout the entire altitude range.

In contrast, a vertical Butterworth filter with a cutoff wavelength of $\lambda_{z,cut} = 15\,\mathrm{km}$ (Figure 2(e)) suppresses the large wavelengths in the upper stratosphere, so the NOGWs are only observable up to an altitude of roughly 30 km. Ehard et al. (2015), Reichert et al. (2021), or Strelnikova et al. (2021) use $\lambda_{z,cut} = 15\,\mathrm{km}$ for studying gravity waves in the stratosphere and mesosphere but Reichert et al. (2021) also state that vertical wavelengths may exceed 15 and even 20 km in the presence of a strong polar night jet. Figure 2 substantiates this finding and illustrates in panels (g) and (h) why increasing $\lambda_{z,cut}$ to 20 km is not generally applicable. Horizontal phase lines persisting for the entire period with a vertical wavelength of roughly 20 km dominate the time-height diagram in Fig. 2(g). A transient wave signal with tilted phase lines between the dotted lines is barely visible. The explanation of these broad phase lines follows from panel 2(f). The mean absolute temperature (thick black line) has a pronounced minimum below the stratopause. This minimum between 35 and 55 km persists for the entire period and results in a pronounced bias (mean T' in Panel 2(h)) of the vertical 20 km Butterworth filter. Combined with tropopause and stratopause, it creates stationary temperature perturbations with a λ_z between 20 and 25 km and amplitudes of 4-10 K. Small biases also exist for the 15 km Butterworth filter in panel 2(f) at the tropopause (10 km) and stratopause (55 km) level, but the temperature minimum in the upper stratosphere mainly affects the 20 km filter.

Figures 9 and 10 in the appendix complement the comparison of different filters showing ERA5 time-height diagrams for CORAL's location in the vicinity of the Andes Mountains for two periods with measurements. Here, the vertical background temperature profiles do not show a pronounced minimum below the stratopause, and the Butterworth filters in the respective panels (e) and (g) prove helpful for identifying horizontal phase lines of stationary mountain waves.

Figure 3 presents additional vertical profiles of absolute temperature for 20 different locations in the Southern Hemisphere outlining the spatial distribution of the temperature minimum in the upper stratosphere for the July 2014 period. The virtual lidar location of Figure 2 is right in the center of the regular latitude-longitude grid. The temperature minimum is widely spread towards the north and west of the virtual lidar location but also exists southward and eastward in the immediate surroundings. The pattern becomes less pronounced towards the southeast and completely vanishes within the polar vortex indicated by the blue shading, highlighting the cold stratospheric temperatures between 10 and 35 km.

Without going into further details on the associated atmospheric processes (consult the discussion about planetary waves in Section 5b of Gisinger et al. (2017)), Figure 3 demonstrates that the temperature minimum below the stratopause is not a local phenomenon but a widespread feature of the background temperature profile at the time that can significantly affect the gravity wave retrieval. More specifically, ambient profiles modified by large-scale atmospheric processes may limit the gravity wave retrieval with vertical filters (see also, e.g., Rapp et al., 2018; Harvey & Knox, 2019). Being insensitive to these patterns of the vertical background temperature profile is a clear advantage of the temporal filtering in Figure 2(c) and (d) and makes it particularly helpful to detect transient gravity waves with large vertical wavelengths in the presence of the PNJ. Therefore, the 12 h running mean will be the foundation for the ERA5 composition introduced in the following subsection to investigate NOGWs in the context of ground-based Rayleigh lidar measurements. However, other filters may be considered for different applications.

3.2 ERA5 overview for a virtual lidar location over the Southern Ocean

In the previous subsection, we elaborated a suitable retrieval for transient NOGWs in time-height diagrams from vertically staring ground-based Rayleigh lidar instruments. Now, we complement these observed time-height sections of temperature perturbations with different meteorological analyses in a single figure to facilitate the interpretation of the measurements. Figure 4 is composed out of seven different panels based on 1-hourly ERA5 reanalyses. Similar to panels (c) and (d) in Figure 2, panel (a) of Figure 4 is the time-height diagram that emulates the lidar measurements showing temperature perturbations after subtracting a 12 h running mean and Figure 4(b) is the absolute temperature profile. The black line in Figure 4(a) refers to the timestamp visualized in panels (c) to (g).

In Figure 4 and in following figures of the same kind, panels (c) to (f) display vertical sections along selected sectors of the latitude circle (c, e) and of the meridian (d, f) intersecting at the lidar location. The panels (c) and (d) depict the stratospheric gravity wave fields in terms of temperature perturbations, potential temperature, and horizontal wind from 14 to 61 km altitude. The temperature perturbations are plotted after applying a horizontal one-dimensional Gaussian filter with $\lambda_{xy,cut} = 900$ km. Both lower panels (e) and (f) display the thermal stability from 3 km to 14 km altitude and allow the localization of the tropopause. Additionally, isentropic lines and zonal and meridional winds are depicted. It must be noted that all four panels exaggerate the height. Panel (c), for example, would be about 120 times longer in the horizontal direction if the aspect ratio were realistic. The vertical dashed lines in panels (c) to (f) refer to the location of the time-height diagram in (a), the virtual lidar location.

The final bottom panel (g) combines a so-called tropopause map (Morgan & Nielsen-Gammon, 1998) with the geopotential height and wind field at 850 hPa. This visualization indicates the position of upper-level troughs and ridges. Furthermore, it displays the direction and strength of the wind in the lower troposphere so that periods with cross-mountain flows and the excitation of mountain waves can be detected. Dashed lines refer to the cross sections in panels (c) to (f). Examining panels (c) through (g) at successive time steps reveals the temporal evolution of the tropospheric and stratospheric flow conditions, the upper-level troughs, and the gravity wave-induced flow response in the middle atmosphere. The synoptic examination of the composite figure may provide an indication of the dynamical processes in the atmosphere associated with possible transient or steady wave sources. For this purpose, the series of identical composite figures for the whole period in panel (a) has been animated[1].

Consistent with Dörnbrack et al. (2022), in the animation of Figure 4, the largest gravity wave amplitudes in the upper stratosphere in panel (c) repeatedly appear above the eastward propagating upper-level trough in panel (e). In the time-height diagram (a), this gravity wave signal appears gradually at lower altitudes before it almost simultaneously appears above 30 km. The timestamp in Figure 4(c) reveals that the waves propagate up and upstream with rather horizontally oriented phase lines in the presence of weaker winds in the lower stratosphere. Above 30 km, the phase lines lean into the stronger winds of the polar night jet, the vertical wavelength increases and the upstream propagation vanishes. In addition, panel 4(d) emphasizes the refraction of these NOGWs southward into the polar night jet.

At this point, we can test the derivation of wave properties in time-height diagrams for gravity waves excited by a propagating source introduced in Section 2b and partly validate it with Figure 4(c). At z $\approx$ 25 and 45 km, we estimate vertical wavelengths $\lambda_z \approx 9$ and 20 km and about 10 and 12 h between two consecutive maxima. Following the procedure in Section 2b, these periods imply horizontal wavelengths λ_x of 500 and 600 km, respectively, which are reasonable approximations compared with phase lines in Panel (c). The corresponding vertical group velocities are 0.49 and 2.1 m s^{-1} and depict a consistent picture with idealized theories that the vertical propagation speed increases in the presence of larger horizontal wind speeds (e.g., Gill, 1982).

4 Gravity waves in Rayleigh lidar observations and ERA5

Since 2018, the Compact Autonomous Rayleigh Lidar (CORAL) of the DLR conducts measurements at the southern tip of South America (53.79°S) in Río Grande, Argentina (B. Kaifler & Kaifler, 2021). Its automated operation provides a unique data set of observations near 60°S. But its proximity to the Andes is no coincidence. It is a very suitable location to study the Earth strongest hot spot of large-amplitude mountain waves in the middle atmosphere (Rapp et al., 2021; Reichert et al., 2021). And, as is often the case, reality is not perfect and the conditions for identifying non-orographic gravity waves are not ideal at this place.

Nevertheless, it may be possible to detect signatures of NOGWs from transient wave sources in these Rayleigh lidar measurements, even though CORAL measurements are dominated by mountain waves in austral winter (N. Kaifler et al., 2020; Reichert et al., 2021). In the following, we present two selected CORAL observations that show similar phase line patterns in the time-height diagrams as the simulated ones in Section 2 or the virtual lidar over the Southern Ocean in Section 3. More specifically, they show upward-tilted phase lines.

4.1 CORAL observations

Figures 5 and 6 show night-time temperature measurements for selected days in June 2018 and August 2020. A background state $\bar{T}$ is computed by calculating the nightly mean temperature and temperature perturbations T' in panels (b) are determined by subtracting $\bar{T}$ from the absolute temperature measurements as shown in panels (a) of Figures 5 and 6, respectively. This approach is similar to the approach used for the ERA5 data as shown in panels (c) of Figures 2, 9, and 10, respectively. In addition, panels (c) of Figures 5 and 6 show T' after applying a vertical Butterworth highpass filter with a cutoff wavelength of $\lambda_{z,cut} = 20$ km (e.g., Ehard et al., 2015) to identify stationary mountain waves. Though multiple studies suggest $\lambda_{z,cut} = 15$ km for mountain waves, we adapt to recent results of Reichert (2022), who discovered that more than 50% of the waves in the analyzed CORAL dataset have vertical wavelengths larger than 16.5 km. Most likely, Reichert's finding is a result of the very strong horizontal winds in the PNJ above Río Grande in austral winter and it is consistent with our analysis in Section 3. In Figure 2(e), the 15 km-Butterworth filter did not resolve the NOGWs above 30 km because their vertical wavelength exceeded 20 km in the upper stratosphere. The increase of λ_z for a vertically increasing PNJ wind was clearly identified in the idealized simulations and is visible by comparing panels (c) and (d) with (e) and (f) of Figure 1.

Such an increase in λ_z is also apparent in the June 2018 measurement period (Figure 5(b) and (c)): After 05:00 UTC, distinct upward-tilted phase lines are observed, and λ_z is between 10 and 12 km in the stratosphere up to about 35 km altitude and between 15-20 km above. The phase lines' angle is approximately 10 km over 5-6 h, so it is in the same range as the angle in the idealized simulation in panel 1(f). The nearly horizontal phase lines observed before 05:00 UTC suggest that these waves are most probably due to mountain waves entering CORAL's field of view. To explore possible reasons for the following ascending phase lines, we associate them with non-steady atmospheric processes. Therefore, a detailed analysis of the synoptic evolution during the event proves essential to enable meaningful physical interpretations in the following section.

The August 2020 case in Figure 6 comprises nightly measurements for two consecutive nights. Unfortunately, these nights were temporarily cloudy at Río Grande, preventing continuous measurements. On the other hand, knowledge of cloud cover could prove promising as these clouds are associated with a passing surface low and an upper-level front and indicate a possible transient wave source. During the first night, Figure 6(b) and (c) show upward-tilted phase lines, which are most pronounced between 40 and 60 km altitude. For the second night, temperature perturbations vary significantly after applying temporal or vertical filtering, but again, subtracting the temporal mean results in distinct upward-tilted phase lines between 30 and 55 km and 22:00 and 07:00 UTC on August 9 in Figure 6(b).

In the following section, we present the composite Figures 7 and 8 based on ERA5 data, which are similar to Figure 4, to support further interpretations of the CORAL measurements. Phase lines in both time-height diagrams (a) of Figures 7 and 8 agree well with the observations. The waves' phases match the overlaid measurements and the phase lines also tilt upward for the measurement periods. This initial visual inspection strongly suggests that the atmospheric processes causing the upward slope in these CORAL measurements are represented in ERA5 and are adequately covered by the dynamics of the underlying IFS model. A closer look at each case and its animated ERA5 composition[1] may be instructive.

[1] https://doi.org/10.5281/zenodo.8319370

4.2 ERA5 overview for June 2018 measurements

First, we determine whether the upward-tilted phase lines in Figures 5(b) and (c) and Figure 7(a) are related to the gravity wave excitation near a propagating upper-level trough. Stratospheric temperature perturbations, as shown in panel 5(c), are tilted upstream into the dominant zonal wind, reaching more than 165 m s^{-1}, see panel 7(d). This finding clearly illustrates that most of the stratospheric gravity wave activity is confined to the PNJ. In panel 7(c), other coherent gravity wave patterns can be identified west of 100°W and east of the CORAL site. At the time shown in Figure 7, the vertical section in panel (e) shows an upper-level trough west 100°W and near 60°W, in between, a ridge enhances the tropopause height to about 12.5 km. The upper-level trough at 60°W already passed CORAL's location 24 hours earlier, as seen in the preceding time steps[1]. The altitude of the dynamical tropopause, as shown by the blueish colors northeast of CORAL in Figure 7(g), indicates that the upper-level trough is located east of Río Grande.

Signatures of upward-tilted phase lines in the time-height diagram 7(a) in the ERA5 data and in the measurements occur well after the passage of the upper-level trough. Therefore, assuming that gravity wave-induced perturbations occur directly over the upper level trough, it appears that in this case the upward-tilted phase lines are not caused by NOGWs over an upper-level trough. Can alternative atmospheric processes be identified in the ERA5 data that led to the tilted phase lines?

During the period of the CORAL observations, the upper-level ridge (as marked by the dark red area in panel (g) of Figure 7) approaches the lidar station from the west. The associated tropospheric flow turns from southerly winds at 850 hPa to southwesterly and westerly winds, which can be observed in Figure 7(g) over several time steps. As a result, the wind component perpendicular to the mountain range becomes stronger, leading to a temporary increase in the winds at mountain crests. Subsequently, the forcing winds remain almost the same, causing a nearly steady regime that favors the excitation of mountain waves on the southernmost mountain range of the Andes, the Cordillera Darwin. The time-height diagrams in Figure 9(e) and (g) related to Figure 7 support this interpretation. The upward-tilted phase lines of the ERA5 data turn into horizontal phase lines that persist for nearly 12 h after the CORAL measurement period. The ERA5 data, therefore, give a clear indication of stationary mountain waves. In addition, phase lines at the bottom edge (≈ 15 km) of panels 7(c) and (d) also indicate an excitation of mountain waves southwest of CORAL's location. This deduction becomes clearer by comparing the phase lines, particularly their location, for different timestamps[1].

A similar explanation can be found for the descending phase lines in the first 12-15 hours of Figure 7(a): The wind at the mountain tops decreases due to the departure of the low-pressure system and the associated low-level wind change to southerlies. The descending phase lines are only briefly interrupted between 15 UTC and 21 UTC on June 22, 2018, before the excitation of mountain waves intensifies, as discussed above. All in all, these virtual observations in the ERA5 data provide a conclusive picture and suggest that the upward tilt of phase lines in the June 2018 CORAL measurements (Figure 5(b) and (c)) was caused by transient wind forcing that resulted in non-stationary mountain waves. Properties of transient mountain waves under unsteady large-scale forcing have been discussed previously (e.g., Chen et al., 2005, 2007; Portele et al., 2018).

4.3 ERA5 overview for August 2020 measurements: first night

As with the June 2018 CORAL observations, we first check for the presence of an upper-level trough during the August 2020 period in panels (e) and (g) of Figure 8. Visualized is a point in time during the first measurement night, as indicated by the black vertical line in panel 8(a). The funnel-like shape of the PVU contour lines in panel (e) and the green-blue colors in panel (g) of Figure 8 indeed show the existence of a textbook upper-level trough upstream of CORAL at 85°W. The timing of the passage of the upper-level trough does not match the first measurement period with upward-tilted phase lines, but the animation[1] reveals that it could fit with CORAL observations during the second night from August 8 to 9. Upward-tilted phase lines are also apparent in ERA5 above 25 km during this second measurement period (Figure 8(a)). The pattern is not as distinct as in Figure 4, but at CORAL's location, it could be related to a superposition of mountain waves impeding explicit conclusions. Section 4d will focus on this second measurement period and examine whether it is possible to associate the corresponding phase line pattern with NOGWs. Within this section, we focus on analyzing the first measurement night. Could a transient wind forcing again explain the phase lines' upward tilt?

As depicted in the meridional section of Figure 8(d), the PNJ is centered directly above CORAL. Considering the horizontal refraction of gravity waves into the jet, as discussed for example by Sato et al. (2012), phase lines at higher altitudes as depicted in the extended time-height diagram in panel 8(a) could indeed belong to mountain waves excited by the cross-mountain flow further north or south. Actually, the southward tilt of the phase lines in panel 8(d) suggests that waves observed by CORAL above 40 km altitude originate farther north at latitudes around 40° to 50°S. At these latitudes, the Andes run almost exactly north-south and are a reliable source of mountain waves. In fact, the direction of the wind changes from a westerly to a northwesterly flow and the strength of the prevailing wind blowing over the Andes in this area increases before and during the observation period. However, the conditions are not as unambiguous as in the first case of June 2018. Wind speed and direction at lower levels still change afterwards, and another feature in the ERA5 data should be noted.

Meridional winds in Figure 8(c) show a wind turning from a westerly towards a more southwesterly flow between 40 and 60 km altitude and between 35° to 50°W. This change in the meridional wind component indicates a meandering of the PNJ that passed CORAL at around 19:00 UTC, just three hours before the lidar started its measurements. Observing the phase lines in Figure 8(c) for several successive timestamps, a shortening of the vertical wavelengths is noticeable, which appears to follow the meandering of the PNJ. These changes in stratospheric propagation conditions occur at the same times when the upward-sloping phase lines in 8(a) appear. The vertical wavelengths decrease toward the end of the upward tilt before increasing again.

In conclusion, the interpretation of the ERA5 data is not as clear for the August 2020 CORAL measurements. NOGWs excited above a propagating upper-level trough can be most likely ruled out as the source for the upward-tilted phase lines. The analysis so far seems to indicate that the propagation conditions have changed during the observations. This is not surprising, since the waves certainly also deposit momentum and reduce the strength of the PNJ: Panel (d) of Figure 8 shows very impressively a local deceleration of the PNJ at about 50 km altitude at the position of CORAL. In addition, the transient low-level winds altered the forcing conditions for mountain waves, making it difficult to make a definite statement about the ascending phase lines in Figure 8(a).

4.4 ERA5 overview for August 2020 measurements: second night

The dotted rectangle in panels (c) and (e) of Figure 8 frames gravity waves in the stratosphere above a westward propagating upper-level trough. These NOGWs are already visible in the lower stratosphere, and their phase line pattern is very similar to the ERA5 analysis of NOGWs over the Southern Ocean in Figure 4 and Figure 17 in Dörnbrack et al. (2022). The local coincidence of the NOGWs in the stratosphere and the underlying upper-level trough at successive times is even more evident in the time sequence of Figure 8[1]: It reveals that and how these stratospheric gravity waves propagate eastward in concert with the upper-level trough. The phase lines shape and the nearly uniform propagation of these waves in ERA5 again resemble the results of the idealized numerical simulations presented in Section 2. In addition to the case of Dörnbrack et al. (2022) in Section 3, this finding represents another example of NOGWs over a propagating upper-level trough that mimics the pattern of mountain waves. This supports the hypothesis that an upper-level trough, particularly the undulated isentropes near and above the tropopause, could be a wave-generating internal boundary to the stratospheric flow aloft, just as mountains at the surface are to the tropospheric flow. The difference lies in the fact that the undulated isentropes are part of the atmospheric flow and change width and depth depending on the stage of the baroclinic life cycle.

In this second example, the upper-level trough propagates over the Pacific Ocean, and its vicinity to the southern tip of South America allows a direct comparison of these NOGWs to mountain waves over the Andes in Figure 8(c). The maximum amplitudes of the NOGWs are ≈ 3 K between 40 and 45 km altitude and are much lower than the amplitudes of the mountain waves at the same altitude, latitude, and time over the Andes, which are ≈ 12 K. This finding is consistent with a recent climatological analysis using AIRS satellite observations that reveals significantly smaller momentum fluxes for NOGWs over the ocean (Hindley et al., 2020). Also, Hendricks et al. (2014) concluded that the wave amplitudes are much weaker across the mid-latitude Pacific Ocean.

The preceding results of this section 4 have shown that these eastward propagating NOGWs indeed lead to upward sloping phase lines in time-height diagrams as anticipated from the idealized simulations (Figure 1). However, detecting these NOGWs in ground-based Rayleigh lidar measurements becomes complicated at locations where mountain waves dominate and superimpose other wave signals, as in the case of CORAL. The upper-level trough framed by the dotted rectangle in Figure 8(e) passes CORAL's location between 17:00 and 21:00 UTC on August 8, just before the lidar started measuring around 22:00 UTC. The corresponding gravity waves in the stratosphere in Panel (c) appear slightly upstream of the trough at multiple timestamps[1], so CORAL's measurements exactly match the passage of these NOGWs.

As previously stated, the wave signals in the ERA5 data and measurements fit qualitatively, but measured amplitudes are generally a factor 2 higher. Phase lines in the time-height diagram in Figure 8(a) tilt upward during the whole measurement period from 22:00 UTC to 09:00 UTC on August 9, but the pattern is less distinct compared to the event over the Southern Ocean in Figure 4(a). With some imagination, phase lines are less steep and vertical wavelengths smaller below 30 km which would be consistent with the Southern Ocean case. At the same time, the animation of Figure 8[1], particularly panels (c) and (d), illustrate that mountain waves excited by the Andes Mountains are regularly affecting CORAL's field of view. Panels (e) and (g) in Figure 10 complement this interpretation, and horizontal phase lines above 30 km suggest the presence of stationary mountain waves during the second CORAL measurement. In this period, the Butterworth filter is reliable because the vertical background temperature profile in Figure 8(b) or the right column in Figure 10 does not contain any small-scale oscillations in the upper stratosphere.

In both, the animation[1] and Figure 10, these stationary mountain waves are less pronounced at the beginning of the measurements between 21:00 and 01:00 UTC but amplitudes increase again after 01:00 UTC. Such transient processes also influence the temperature perturbations in time-height diagrams after applying a temporal filter in Figure 4(a) or 10(b) and complicate the identification of NOGWs in Rayleigh lidar measurements. Combined with the fact that NOGWs have relatively smaller amplitudes, an identification seems only feasible when measurements overlap with the passage of an upper-level trough during a period with negligible mountain wave forcing. Or, put another way, a lidar location far from significant orographic gravity wave sources would simplify the investigation of NOGWs.

5 Summary and Conclusions

This article addresses how NOGWs excited by propagating upper-level troughs can be identified in time-height diagrams of ground-based Rayleigh lidar observations. Idealized numerical simulations were first presented to show the difference between stratospheric temperature perturbations in simulated lidar signals resulting from stationary and transient wave sources. Upward-tilted phase lines are the main characteristics of simulated lidar signals for the case when the wave source moves in the direction of the mean wind. The angle of the tilt depends on the source's propagation speed and the gravity wave's horizontal wavelength. If the source moves in the opposite direction to the wind, the phase lines decrease in height with progressing time, a case not shown and discussed here. In the time-height diagrams, the sloping phase lines differ notably from the horizontal phase lines typically found for stationary mountain waves. Thus, sloping phase lines in ground-based lidar data can potentially be associated with transient wave sources. It must be noted, however, that other atmospheric processes, such as increasing or decreasing winds, i.e. transient propagation conditions, also lead to tilted phase lines.

Therefore, it is very helpful and actually just necessary to relate the observed time-height diagram to meteorological variables from available high-resolution NWP models and their temporal evolution in the vicinity of the lidar site. To this end, we have proposed a composite figure that combines the temporal evolution in a time-height diagram with spatial illustrations in vertical and horizontal sections. This composite figure is produced for all available times provided by the respective meteorological analyses or forecasts. Animations of the composite figure help to identify transient and steady modes of gravity waves as well as propagating upper-level troughs. Here, the most recent ECMWF reanalyses ERA5 data (Hersbach et al., 2020) are used as they partially resolve atmospheric gravity waves (e.g., Gupta et al., 2021; Pahlavan et al., 2023). The ERA5 data only give an indication of gravity waves produced by primary sources such as flows over mountains, frontal systems aloft, convection, etc. Due to numerical vorticity and divergence damping of motion fields above 10 hPa, most vertically propagating gravity wave modes are attenuated, and the generation of secondary waves cannot be represented by IFS (Polichtchouk et al., 2023, Sec. 2).

Subsequent to the idealized simulations, the composite figure was introduced by means of NOGWs above an upper-level trough over the Southern Ocean, which were already discussed by Dörnbrack et al. (2022). Here, the composite plots were produced for a virtual lidar location far away from any orography and the ERA5 data was used to emulate the measurements of a vertically starring ground-based lidar. As predicted by the idealized simulations, a distinct pattern of upward-tilted phase lines dominated the time-height diagram during the passage of the upper-level trough and corresponding NOGWs in the stratosphere. The proposed procedure was confirmed and it could also be clarified that a temporal filtering is advantageous for the identification of these NOGWs, particularly in the presence of a strong PNJ and large vertical wavelengths which limit the application of a vertical Butterworth filter.

In a final step, it was the goal to identify NOGWs in actual ground-based Rayleigh lidar measurements. The analysis of two selected periods with CORAL observations revealed the full complexity of the real atmospheric flow at the lidar site in Argentine Patagonia in the lee of the Andes. For two out of the three measurement nights, the composite figures revealed that propagating upper-level troughs did not cause the upward-tilted phase lines in the CORAL measurements. Inspection of the vertical and horizontal sections for successive times, however, suggested that mountain waves interacted with transient background wind conditions. The third measurement exactly matched the passage of an upper-level trough and corresponding NOGWs, but the small-amplitude NOGWs were superimposed by large-amplitude mountain waves and clear identification of gravity waves excited by an upper-level trough was not feasible. In fact, a direct comparison of these NOGWs identified upstream over the Pacific Ocean with mountain waves over the southern Andes revealed that the amplitudes of these NOGWs are about a factor of 4 smaller than the amplitudes of mountain waves.

Nevertheless, the analysis showed that the proposed composite plots are extremely useful for placing the CORAL observations in a meteorological context with relatively little effort. As such, they can be a helpful starting point to develop hypotheses about the origins of the observed waves and their sources before using other, more elaborate methods such as ray tracing or numerical simulations.

In most cases, it will be difficult to effectively isolate NOGWs in Rayleigh lidar measurements at sites commonly dominated by strong mountain waves, such as CORAL in Río Grande, Argentina. A lidar site less influenced by mountain waves, like the virtual lidar location over the Southern Ocean in Section 3, could show whether the discussed signatures can be identified over propagating upper-level troughs and provide further insight into the proposed excitation process. A flat island would be the ideal environment, but options are limited, and islands like South Georgia, the Islas Malvina (Falkland Islands), or Auckland islands are also prone to mountain waves (e.g., Vosper, 2015; Hindley et al., 2021; Mixa et al., 2021).

Appendix A Open Research

The ERA5 reanalysis dataset is publicly available at `https://cds.climate.copernicus.eu` and cited as required.

Animations of figures in this work showing compositions of weather prediction data (ERA5 data) support the discussion and are available at `https://doi.org/10.5281/zenodo.10073388` via 10.5281/zenodo.10073388. Corresponding CORAL measurements are also included and the underlying source code for the ERA5 visualizations is publicly available at `https://github.com/michibinder/eratools`.

Acknowledgments
We gratefully acknowledge the work of Bernd Kaifler and his team who built and operate the COmpact Rayleigh Autonomous Lidar in Río Grande and provide the temperature measurements.

References

Alexander, M. J., Geller, M., McLandress, C., Polavarapu, S., Preusse, P., Sassi, F., ... Watanabe, S. (2010, July). Recent developments in gravity-wave effects in climate models and the global distribution of gravity-wave momentum flux from observations and models: Recent Developments in Gravity-Wave Effects. *Quarterly Journal of the Royal Meteorological Society*, *136*(650), 1103–1124. Retrieved 2021-05-11, from `http://doi.wiley.com/10.1002/qj.637` doi: 10.1002/qj.637

Bacmeister, J., & Schoeberl, M. (1989). Breakdown of Vertically Propagating Two-Dimensional Gravity Waves Forced by Orography. *Journal of the Atmospheric Sciences*, *46*. doi: 10.1175/1520-0469(1989)046⟨2109:BOVPTD⟩2.0.CO;2

Chen, C.-C., Durran, D. R., & Hakim, G. J. (2005). Mountain-Wave Momentum Flux in an Evolving Synoptic-Scale Flow. *Journal of the Atmospheric Sciences*, *62*(9), 3213 - 3231. Retrieved from `https://journals.ametsoc.org/view/journals/atsc/62/9/jas3543.1.xml` doi: https://doi.org/10.1175/JAS3543.1

Chen, C.-C., Hakim, G. J., & Durran, D. R. (2007). Transient Mountain Waves and Their Interaction with Large Scales. *Journal of the Atmospheric Sciences*, *64*(7), 2378 - 2400. Retrieved from `https://journals.ametsoc.org/view/`

journals/atsc/64/7/jas3972.1.xml doi: https://doi.org/10.1175/JAS3972.1

Chu, X., Zhao, J., Lu, X., Harvey, V. L., Jones, R. M., Becker, E., ... Dörnbrack, A. (2018). Lidar Observations of Stratospheric Gravity Waves From 2011 to 2015 at McMurdo (77.84°S, 166.69°E), Antarctica: 2. Potential Energy Densities, Lognormal Distributions, and Seasonal Variations. *Journal of Geophysical Research: Atmospheres*, *123*(15), 7910-7934. Retrieved from https://agupubs.onlinelibrary.wiley.com/doi/abs/10.1029/2017JD027386 doi: https://doi.org/10.1029/2017JD027386

Clark, T. L. (1977). A small-scale dynamic model using a terrain-following coordinate transformation. *Journal of Computational Physics*, *24*(2), 186-215. Retrieved from https://www.sciencedirect.com/science/article/pii/0021999177900572 doi: https://doi.org/10.1016/0021-9991(77)90057-2

Dörnbrack, A., Gisinger, S., Kaifler, N., Portele, T. C., Bramberger, M., Rapp, M., ... Jelić, D. (2018). Gravity waves excited during a minor sudden stratospheric warming. *Atmospheric Chemistry and Physics*, *18*(17), 12915–12931. Retrieved from https://acp.copernicus.org/articles/18/12915/2018/ doi: 10.5194/acp-18-12915-2018

Dörnbrack, A. (2002). Evidence for inertia gravity waves forming polar stratospheric clouds over Scandinavia. *Journal of Geophysical Research*, *107*(D20), 8287. Retrieved 2022-12-09, from http://doi.wiley.com/10.1029/2001JD000452 doi: 10.1029/2001JD000452

Dörnbrack, A., Eckermann, S. D., Williams, B. P., & Haggerty, J. (2022, February). Stratospheric Gravity Waves Excited by a Propagating Rossby Wave Train—A DEEPWAVE Case Study. *Journal of the Atmospheric Sciences*, *79*(2), 567–591. Retrieved 2022-03-20, from https://journals.ametsoc.org/view/journals/atsc/79/2/JAS-D-21-0057.1.xml doi: 10.1175/JAS-D-21-0057.1

Dörnbrack, A., Gisinger, S., & Kaifler, B. (2017, March). On the Interpretation of Gravity Wave Measurements by Ground-Based Lidars. *Atmosphere*, *8*(12), 49. Retrieved 2021-03-08, from http://www.mdpi.com/2073-4433/8/3/49 doi: 10.3390/atmos8030049

Eckermann, S. D., Doyle, J. D., Reinecke, P. A., Reynolds, C. A., Smith, R. B., Fritts, D. C., & Dörnbrack, A. (2019, September). Stratospheric Gravity Wave Products from Satellite Infrared Nadir Radiances in the Planning, Execution, and Validation of Aircraft Measurements during DEEPWAVE. *Journal of Applied Meteorology and Climatology*, *58*(9), 2049–2075. Retrieved 2023-02-12, from https://journals.ametsoc.org/view/journals/apme/58/9/jamc-d-19-0015.1.xml doi: 10.1175/JAMC-D-19-0015.1

Ehard, B., Kaifler, B., Kaifler, N., & Rapp, M. (2015, November). Evaluation of methods for gravity wave extraction from middle-atmospheric lidar temperature measurements. *Atmospheric Measurement Techniques*, *8*(11), 4645–4655. Retrieved 2022-08-27, from https://amt.copernicus.org/articles/8/4645/2015/ doi: 10.5194/amt-8-4645-2015

Ehard, B., Malardel, S., Dörnbrack, A., Kaifler, B., Kaifler, N., & Wedi, N. (2018). Comparing ECMWF high-resolution analyses with lidar temperature measurements in the middle atmosphere. *Quarterly Journal of the Royal Meteorological Society*, *144*(712), 633-640. Retrieved from https://rmets.onlinelibrary.wiley.com/doi/abs/10.1002/qj.3206 doi: https://doi.org/10.1002/qj.3206

Epifanio, C. C., & Durran, D. R. (2001). Three-dimensional effects in high-drag-state flows over long ridges. *Journal of the atmospheric sciences*, *58*(9), 1051–1065. doi: https://doi.org/10.1175/1520-0469(2001)058⟨1051:TDEIHD⟩2.0.CO;2

Ern, M., Trinh, Q. T., Preusse, P., Gille, J. C., Mlynczak, M. G., Russell III, J. M., & Riese, M. (2018, April). GRACILE: a comprehensive climatology of atmospheric gravity wave parameters based on satellite limb soundings. *Earth System Science Data*, *10*(2), 857–892. Retrieved 2022-11-19, from https://essd.copernicus.org/articles/10/857/2018/ doi: 10.5194/essd-10-857-2018

Fritts, D. C., & Alexander, M. J. (2003). Gravity wave dynamics and effects in the middle atmosphere. *Reviews of Geophysics*, *41*(1), 1003. Retrieved 2021-03-22, from http://doi.wiley.com/10.1029/2001RG000106 doi: 10.1029/2001RG000106

Fritts et al. (2016, March). The Deep Propagating Gravity Wave Experiment (DEEPWAVE): An Airborne and Ground-Based Exploration of Gravity Wave Propagation and Effects from Their Sources throughout the Lower and Middle Atmosphere. *Bulletin of the American Meteorological Society*, *97*(3), 425–453. Retrieved 2021-05-14, from https://journals.ametsoc.org/doi/10.1175/BAMS-D-14-00269.1 doi: 10.1175/BAMS-D-14-00269.1

Gettelman, A., Hoor, P., Pan, L. L., Randel, W. J., Hegglin, M. I., & Birner, T. (2011). THE EXTRATROPICAL UPPER TROPOSPHERE AND LOWER STRATOSPHERE. *Reviews of Geophysics*, *49*(3). Retrieved from https://agupubs.onlinelibrary.wiley.com/doi/abs/10.1029/2011RG000355 doi: https://doi.org/10.1029/2011RG000355

Gill, A. E. (1982). *Atmosphere-Ocean Dynamics.* New York: Academic Press.

Gille, J., Barnett, J., Arter, P., Barker, M., Bernath, P., Boone, C., … Young, G. (2008, June). High Resolution Dynamics Limb Sounder: Experiment overview, recovery, and validation of initial temperature data. *Journal of Geophysical Research*, *113*(D16), D16S43. Retrieved 2023-02-12, from http://doi.wiley.com/10.1029/2007JD008824 doi: 10.1029/2007JD008824

Gisinger, S., Dörnbrack, A., Matthias, V., Doyle, J. D., Eckermann, S. D., Ehard, B., … Rapp, M. (2017). Atmospheric Conditions during the Deep Propagating Gravity Wave Experiment (DEEPWAVE). *Monthly Weather Review*, *145*(10), 4249 - 4275. Retrieved from https://journals.ametsoc.org/view/journals/mwre/145/10/mwr-d-16-0435.1.xml doi: https://doi.org/10.1175/MWR-D-16-0435.1

Gisinger, S., Polichtchouk, I., Dörnbrack, A., Reichert, R., Kaifler, B., Kaifler, N., … Sandu, I. (2022). Gravity-Wave-Driven Seasonal Variability of Temperature Differences Between ECMWF IFS and Rayleigh Lidar Measurements in the Lee of the Southern Andes. *Journal of Geophysical Research: Atmospheres*, *127*(13), e2021JD036270. Retrieved from https://agupubs.onlinelibrary.wiley.com/doi/abs/10.1029/2021JD036270 (e2021JD036270 2021JD036270) doi: https://doi.org/10.1029/2021JD036270

Goldberg, M. D., Kilcoyne, H., Cikanek, H., & Mehta, A. (2013, December). Joint Polar Satellite System: The United States next generation civilian polar-orbiting environmental satellite system: USA NEXT GENERATION SATELLITE SYSTEM. *Journal of Geophysical Research: Atmospheres*, *118*(24), 13,463–13,475. Retrieved 2023-02-12, from http://doi.wiley.com/10.1002/2013JD020389 doi: 10.1002/2013JD020389

Gupta, A., Birner, T., Dörnbrack, A., & Polichtchouk, I. (2021). Importance of Gravity Wave Forcing for Springtime Southern Polar Vortex Breakdown as Revealed by ERA5. *Geophysical Research Letters*, *48*(10), e2021GL092762. Retrieved from https://agupubs.onlinelibrary.wiley.com/doi/abs/10.1029/2021GL092762 (e2021GL092762 2021GL092762) doi: https://doi.org/10.1029/2021GL092762

Harvey, V. L., & Knox, J. A. (2019). Beware of inertial instability masquerading as gravity waves in stratospheric temperature perturbations. *Geophysical Research Letters*, *46*(3), 1740-1745. Retrieved from https://agupubs.onlinelibrary.wiley.com/doi/abs/10.1029/2018GL081142 doi: https://doi.org/10.1029/2018GL081142

Hendricks, E. A., Doyle, J. D., Eckermann, S. D., Jiang, Q., & Reinecke, P. A. (2014, May). What Is the Source of the Stratospheric Gravity Wave Belt in Austral Winter? *Journal of the Atmospheric Sciences*, *71*(5), 1583–1592. Retrieved 2021-07-05, from https://journals.ametsoc.org/doi/10.1175/JAS-D-13-0332.1 doi: 10.1175/JAS-D-13-0332.1

Hersbach et al. (2020, July). The ERA5 global reanalysis. *Quarterly Journal of the Royal Meteorological Society*, *146*(730), 1999–2049. Retrieved 2023-02-10, from https://onlinelibrary.wiley.com/doi/10.1002/qj.3803 doi: 10.1002/qj.3803

Hindley, N. P., Wright, C. J., Gadian, A. M., Hoffmann, L., Hughes, J. K., Jackson, D. R., ... Ross, A. N. (2021). Stratospheric gravity waves over the mountainous island of South Georgia: testing a high-resolution dynamical model with 3-D satellite observations and radiosondes. *Atmospheric Chemistry and Physics*, *21*(10), 7695–7722. Retrieved from https://acp.copernicus.org/articles/21/7695/2021/ doi: 10.5194/acp-21-7695-2021

Hindley, N. P., Wright, C. J., Hoffmann, L., Moffat-Griffin, T., & Mitchell, N. J. (2020, November). An 18-Year Climatology of Directional Stratospheric Gravity Wave Momentum Flux From 3-D Satellite Observations. *Geophysical Research Letters*, *47*(22). Retrieved 2020-12-15, from https://onlinelibrary.wiley.com/doi/10.1029/2020GL089557 doi: 10.1029/2020GL089557

Hindley, N. P., Wright, C. J., Smith, N. D., Hoffmann, L., Holt, L. A., Alexander, M. J., ... Mitchell, N. J. (2019, December). Gravity waves in the winter stratosphere over the Southern Ocean: high-resolution satellite observations and 3-D spectral analysis. *Atmospheric Chemistry and Physics*, *19*(24), 15377–15414. Retrieved 2021-05-13, from https://acp.copernicus.org/articles/19/15377/2019/ doi: 10.5194/acp-19-15377-2019

Hoffmann, L., & Alexander, M. J. (2009). Retrieval of stratospheric temperatures from Atmospheric Infrared Sounder radiance measurements for gravity wave studies. *Journal of Geophysical Research: Atmospheres*, *114*(D7). Retrieved from https://agupubs.onlinelibrary.wiley.com/doi/abs/10.1029/2008JD011241 doi: https://doi.org/10.1029/2008JD011241

Hoffmann, L., Xue, X., & Alexander, M. J. (2013). A global view of stratospheric gravity wave hotspots located with Atmospheric Infrared Sounder observations. *Journal of Geophysical Research: Atmospheres*, *118*(2), 416-434. Retrieved from https://agupubs.onlinelibrary.wiley.com/doi/abs/10.1029/2012JD018658 doi: https://doi.org/10.1029/2012JD018658

Kaifler, B., & Kaifler, N. (2021, March). A Compact Rayleigh Autonomous Lidar (CORAL) for the middle atmosphere. *Atmospheric Measurement Techniques*, *14*(2), 1715–1732. Retrieved 2021-05-18, from https://amt.copernicus.org/articles/14/1715/2021/ doi: 10.5194/amt-14-1715-2021

Kaifler, B., Lübken, F.-J., Höffner, J., Morris, R. J., & Viehl, T. P. (2015). Lidar observations of gravity wave activity in the middle atmosphere over Davis (69°S, 78°E), Antarctica. *Journal of Geophysical Research: Atmospheres*, *120*(10), 4506-4521. Retrieved from https://agupubs.onlinelibrary.wiley.com/doi/abs/10.1002/2014JD022879 doi: https://doi.org/10.1002/2014JD022879

Kaifler, N., Kaifler, B., Dörnbrack, A., Rapp, M., Hormaechea, J. L., & de la Torre, A. (2020, December). Lidar observations of large-amplitude mountain waves in the stratosphere above Tierra del Fuego, Argentina. *Scientific Reports*, *10*(1), 14529. Retrieved 2020-09-30, from http://www.nature.com/articles/s41598-020-71443-7 doi: 10.1038/s41598-020-71443-7

Kühnlein, C., Smolarkiewicz, P. K., & Dörnbrack, A. (2012, April). Modelling atmospheric flows with adaptive moving meshes. *Journal of Computational Physics*, *231*(7), 2741–2763. Retrieved 2021-03-29, from https://linkinghub.elsevier.com/retrieve/pii/S0021999111007224 doi: 10.1016/j.jcp.2011.12.012

Lane, T. P., Reeder, M. J., & Clark, T. L. (2001). Numerical Modeling of Gravity Wave Generation by Deep Tropical Convection. *Journal of the Atmospheric Sciences*, *58*(10), 1249 - 1274. Retrieved from https://journals.ametsoc.org/view/journals/atsc/58/10/1520-0469_2001_058_1249_nmogwg_2.0.co_2.xml doi: https://doi.org/10.1175/1520-0469(2001)058⟨1249:NMOGWG⟩2.0.CO;2

Le Pichon, A., Assink, J. D., Heinrich, P., Blanc, E., Charlton-Perez, A., Lee, C. F., ... Claud, C. (2015). Comparison of co-located independent ground-based middle atmospheric wind and temperature measurements with numerical weather prediction models. *Journal of Geophysical Research: Atmospheres*, *120*(16), 8318-8331. Retrieved from https://agupubs.onlinelibrary.wiley.com/doi/abs/10.1002/2015JD023273 doi: https://doi.org/10.1002/2015JD023273

Lipps, F. B., & Hemler, R. S. (1982). A Scale Analysis of Deep Moist Convection and Some Related Numerical Calculations. *Journal of the Atmospheric Sciences*, *39*, 2192–2210.

Metz, J. J., & Durran, D. R. (2021, May). Are finite-amplitude effects important in non-breaking mountain waves? *Quarterly Journal of the Royal Meteorological Society*, qj.4045. Retrieved 2021-07-07, from https://onlinelibrary.wiley.com/doi/10.1002/qj.4045 doi: 10.1002/qj.4045

Mixa, T., Dörnbrack, A., & Rapp, M. (2021, May). Nonlinear Simulations of Gravity Wave Tunneling and Breaking over Auckland Island. *Journal of the Atmospheric Sciences*, *78*(5), 1567–1582. Retrieved 2022-12-04, from https://journals.ametsoc.org/view/journals/atsc/78/5/JAS-D-20-0230.1.xml doi: 10.1175/JAS-D-20-0230.1

Mlynczak, M. G. (1997, January). Energetics of the mesosphere and lower thermosphere and the SABER experiment. *Advances in Space Research*, *20*(6), 1177–1183. Retrieved 2023-02-12, from https://linkinghub.elsevier.com/retrieve/pii/S0273117797007692 doi: 10.1016/S0273-1177(97)00769-2

Morgan, M. C., & Nielsen-Gammon, J. W. (1998). Using tropopause maps to diagnose midlatitude weather systems. *Monthly Weather Review*, *126*(10), 2555 - 2579. Retrieved from https://journals.ametsoc.org/view/journals/mwre/126/10/1520-0493_1998_126_2555_utmtdm_2.0.co_2.xml doi: https://doi.org/10.1175/1520-0493(1998)126⟨2555:UTMTDM⟩2.0.CO;2

Pahlavan, H. A., Wallace, J. M., & Fu, Q. (2023). Characteristics of Tropical Convective Gravity Waves Resolved by ERA5 Reanalysis. *Journal of the Atmospheric Sciences*, *80*(3), 777 - 795. Retrieved from https://journals.ametsoc.org/view/journals/atsc/80/3/JAS-D-22-0057.1.xml doi: https://doi.org/10.1175/JAS-D-22-0057.1

Pfister, L., Chan, K. R., Bui, T. P., Bowen, S., Legg, M., Gary, B., ... Starr, W. (1993, May). Gravity waves generated by a tropical cyclone during the STEP tropical field program: A case study. *Journal of Geophysical Research: Atmospheres*, *98*(D5), 8611–8638. Retrieved 2021-06-22, from http://doi.wiley.com/10.1029/92JD01679 doi: 10.1029/92JD01679

Plougonven, R., & Zhang, F. (2014, March). Internal gravity waves from atmospheric jets and fronts. *Reviews of Geophysics*, *52*(1), 33–76. Retrieved 2021-03-23, from http://doi.wiley.com/10.1002/2012RG000419 doi: 10.1002/2012RG000419

Polichtchouk, I., van Niekerk, A., & Wedi, N. (2023). Resolved gravity waves in the extratropical stratosphere: Effect of horizontal resolution increase from o(10) to o(1) km. *Journal of the Atmospheric Sciences*, *80*(2), 473 - 486. Retrieved from https://journals.ametsoc.org/view/journals/atsc/80/2/JAS-D-22-0138.1.xml doi: https://doi.org/10.1175/JAS-D-22-0138.1

Portele, T. C., Dörnbrack, A., Wagner, J. S., Gisinger, S., Ehard, B., Pautet, P.-D., & Rapp, M. (2018). Mountain-Wave Propagation under Transient Tropospheric Forcing: A DEEPWAVE Case Study. *Monthly Weather Review*, *146*(6), 1861 - 1888. Retrieved from `https://journals.ametsoc.org/view/journals/mwre/146/6/mwr-d-17-0080.1.xml` doi: https://doi.org/10.1175/MWR-D-17-0080.1

Preusse, P., Dörnbrack, A., Eckermann, S. D., Riese, M., Schaeler, B., Bacmeister, J. T., ... Grossmann, K. U. (2002, December). Space-based measurements of stratospheric mountain waves by CRISTA 1. Sensitivity, analysis method, and a case study: STRATOSPHERIC MOUNTAIN WAVE MEASUREMENTS BY CRISTA, 1. *Journal of Geophysical Research: Atmospheres*, *107*(D23), CRI 6–1–CRI 6–23. Retrieved 2021-03-22, from `http://doi.wiley.com/10.1029/2001JD000699` doi: 10.1029/2001JD000699

Prusa, J. M., Smolarkiewicz, P., & Garcia, R. (1996, September). Propagation and Breaking at High Altitudes of Gravity Waves Excited by Tropospheric Forcing. *Journal of the Atmospheric Sciences*, *53*. doi: 10.1175/1520-0469(1996)053⟨2186:PABAHA⟩2.0.CO;2

Prusa, J. M., & Smolarkiewicz, P. K. (2003, September). An all-scale anelastic model for geophysical flows: dynamic grid deformation. *Journal of Computational Physics*, *190*(2), 601–622. Retrieved 2021-03-21, from `https://linkinghub.elsevier.com/retrieve/pii/S0021999103002997` doi: 10.1016/S0021-9991(03)00299-7

Prusa, J. M., Smolarkiewicz, P. K., & Wyszogrodzki, A. A. (2008, October). EULAG, a computational model for multiscale flows. *Computers & Fluids*, *37*(9), 1193–1207. Retrieved 2020-12-15, from `https://linkinghub.elsevier.com/retrieve/pii/S004579300700206X` doi: 10.1016/j.compfluid.2007.12.001

Rapp, M., Dörnbrack, A., & Preusse, P. (2018). Large midlatitude stratospheric temperature variability caused by inertial instability: A potential source of bias for gravity wave climatologies. *Geophysical Research Letters*, *45*(19), 10,682-10,690. Retrieved from `https://agupubs.onlinelibrary.wiley.com/doi/abs/10.1029/2018GL079142` doi: https://doi.org/10.1029/2018GL079142

Rapp et al. (2021, April). SOUTHTRAC-GW: An Airborne Field Campaign to Explore Gravity Wave Dynamics at the World's Strongest Hotspot. *Bulletin of the American Meteorological Society*, *102*(4), E871–E893. Retrieved 2021-05-03, from `https://journals.ametsoc.org/view/journals/bams/102/4/BAMS-D-20-0034.1.xml` doi: 10.1175/BAMS-D-20-0034.1

Reichert, R. (2022). *Characterization of gravity waves in the lee of the southern Andes utilizing an autonomous Rayleigh lidar system* (Doctoral dissertation, Ludwig-Maximilians-Universität München). Retrieved 2022-11-10, from `https://edoc.ub.uni-muenchen.de/id/eprint/30211`

Reichert, R., Kaifler, B., Kaifler, N., Dörnbrack, A., Rapp, M., & Hormaechea, J. L. (2021, November). High-Cadence Lidar Observations of Middle Atmospheric Temperature and Gravity Waves at the Southern Andes Hot Spot. *Journal of Geophysical Research: Atmospheres*, *126*(22). Retrieved 2022-08-28, from `https://onlinelibrary.wiley.com/doi/10.1029/2021JD034683` doi: 10.1029/2021JD034683

Sato, K., Tateno, S., Watanabe, S., & Kawatani, Y. (2012, April). Gravity Wave Characteristics in the Southern Hemisphere Revealed by a High-Resolution Middle-Atmosphere General Circulation Model. *Journal of the Atmospheric Sciences*, *69*(4), 1378–1396. Retrieved 2021-03-21, from `https://journals.ametsoc.org/doi/10.1175/JAS-D-11-0101.1` doi: 10.1175/JAS-D-11-0101.1

Schoeberl, M. R. (1985). The Penetration of Mountain Waves into the Middle Atmosphere. *Journal of Atmospheric Sciences*, *42*(24), 2856 - 2864. Retrieved from https://journals.ametsoc.org/view/journals/atsc/42/24/1520-0469_1985_042_2856_tpomwi_2_0_co_2.xml doi: https://doi.org/10.1175/1520-0469(1985)042⟨2856:TPOMWI⟩2.0.CO;2

Smolarkiewicz, P., & Margolin, L. (1993). On Forward-in-Time Differencing for Fluids: Extension to a Curvilinear Framework. *Mon. Weather Rev.*, *121*, 1847–1859. doi: 10.1175/1520-0493(1993)121⟨1847:OFITDF⟩2.0.CO;2

Smolarkiewicz, P. K., & Margolin, L. G. (1997, January). On Forward-in-Time Differencing for Fluids: an Eulerian/Semi-Lagrangian Non-Hydrostatic Model for Stratified Flows. *Atmosphere-Ocean*, *35*(sup1), 127–152. Retrieved 2020-12-15, from http://www.tandfonline.com/doi/abs/10.1080/07055900.1997.9687345 doi: 10.1080/07055900.1997.9687345

Smolarkiewicz, P. K., & Margolin, L. G. (1998, March). MPDATA: A Finite-Difference Solver for Geophysical Flows. *Journal of Computational Physics*, *140*(2), 459–480. Retrieved 2020-12-15, from https://linkinghub.elsevier.com/retrieve/pii/S0021999198959010 doi: 10.1006/jcph.1998.5901

Strelnikova, I., Almowafy, M., Baumgarten, G., Baumgarten, K., Ern, M., Gerding, M., & Lübken, F.-J. (2021). Seasonal Cycle of Gravity Wave Potential Energy Densities from Lidar and Satellite Observations at 54° and 69°N. *Journal of the Atmospheric Sciences*, *78*(4), 1359 - 1386. Retrieved from https://journals.ametsoc.org/view/journals/atsc/78/4/JAS-D-20-0247.1.xml doi: https://doi.org/10.1175/JAS-D-20-0247.1

Vadas, S. L., Fritts, D. C., & Alexander, M. J. (2003, January). Mechanism for the Generation of Secondary Waves in Wave Breaking Regions. *Journal of the Atmospheric Sciences*, *60*(1), 194–214. Retrieved 2022-04-09, from http://journals.ametsoc.org/doi/10.1175/1520-0469(2003)060<0194:MFTGOS>2.0.CO;2 doi: 10.1175/1520-0469(2003)060⟨0194:MFTGOS⟩2.0.CO;2

Vosper, S. B. (2015). Mountain waves and wakes generated by South Georgia: implications for drag parametrization. *Quarterly Journal of the Royal Meteorological Society*, *141*(692), 2813-2827. Retrieved from https://rmets.onlinelibrary.wiley.com/doi/abs/10.1002/qj.2566 doi: https://doi.org/10.1002/qj.2566

Wedi, N. P., & Smolarkiewicz, P. K. (2004). Extending Gal-Chen and Somerville terrain-following coordinate transformation on time-dependent curvilinear boundaries. *Journal of Computational Physics*, *193*(1), 1-20. Retrieved from https://www.sciencedirect.com/science/article/pii/S0021999103003942 doi: https://doi.org/10.1016/j.jcp.2003.07.034

Wright, C. J., Hindley, N. P., Alexander, M. J., Barlow, M., Hoffmann, L., Mitchell, C. N., … Yue, J. (2022). Surface-to-space atmospheric waves from Hunga Tonga–Hunga Ha'apai eruption. *Nature*, *609*, 741–746. doi: https://doi.org/10.1038/s41586-022-05012-5

Yamashita, C., Chu, X., Liu, H.-L., Espy, P. J., Nott, G. J., & Huang, W. (2009). Stratospheric gravity wave characteristics and seasonal variations observed by lidar at the South Pole and Rothera, Antarctica. *Journal of Geophysical Research: Atmospheres*, *114*(D12). Retrieved from https://agupubs.onlinelibrary.wiley.com/doi/abs/10.1029/2008JD011472 doi: https://doi.org/10.1029/2008JD011472

Zhao, J., Chu, X., Chen, C., Lu, X., Fong, W., Yu, Z., … Dörnbrack, A. (2017). Lidar observations of stratospheric gravity waves from 2011 to 2015 at McMurdo (77.84°S, 166.69°E), Antarctica: 1. Vertical wavelengths, periods, and frequency and vertical wave number spectra. *Journal of Geophysical Research: Atmospheres*, *122*(10), 5041-5062. Retrieved from https://agupubs.onlinelibrary.wiley.com/doi/abs/10.1002/2016JD026368 doi: https://doi.org/10.1002/2016JD026368

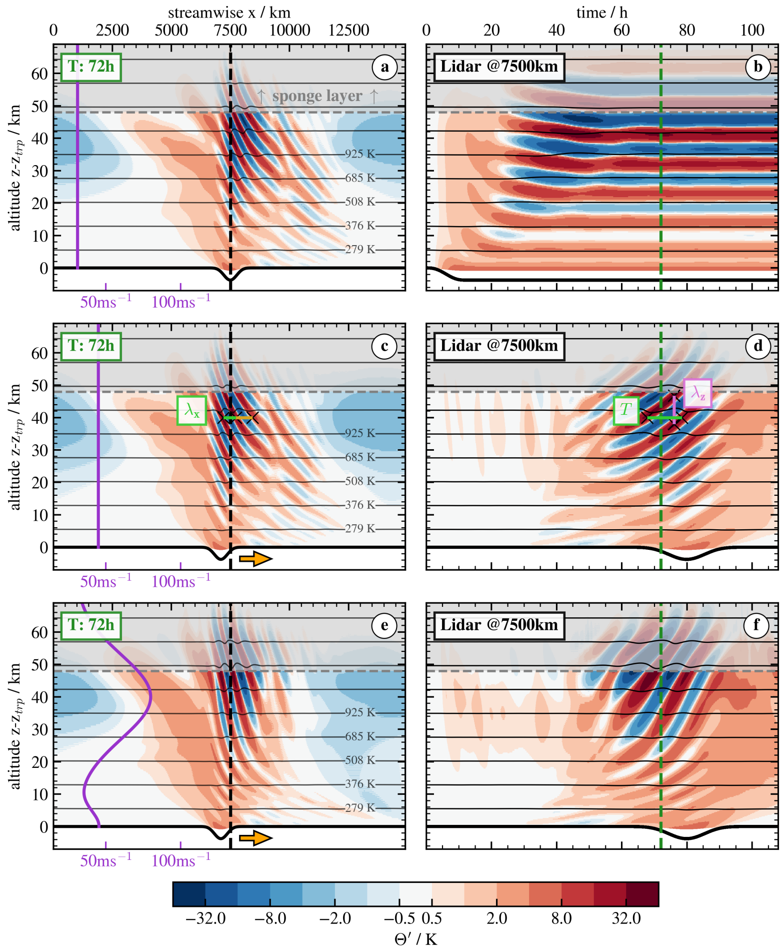

Figure 1. Vertical cross-sections (a, c, e) after $t = 72\,\mathrm{h}$ with ambient wind profiles in purple and time-height diagrams (b, d, f) at the outlined position for three different simulations. The first simulation (a, b) features a stationary obstacle at the lower boundary and a constant wind profile. In the second simulation (c, d) the trough moves to the right with a constant speed $c_{tf} = 13.88\,\mathrm{m\,s^{-1}}$ and the wind is increased by the same amount. The last simulation (e, f) represents a simulation with a more realistic stratospheric wintertime wind profile. The assessment of λ_z and period T from the time-height diagram is labeled in (d), two consecutive λ_x are labeled in (c). Contour lines represent constant potential temperature and the amplitude of the lower boundary is scaled by a factor of 5.

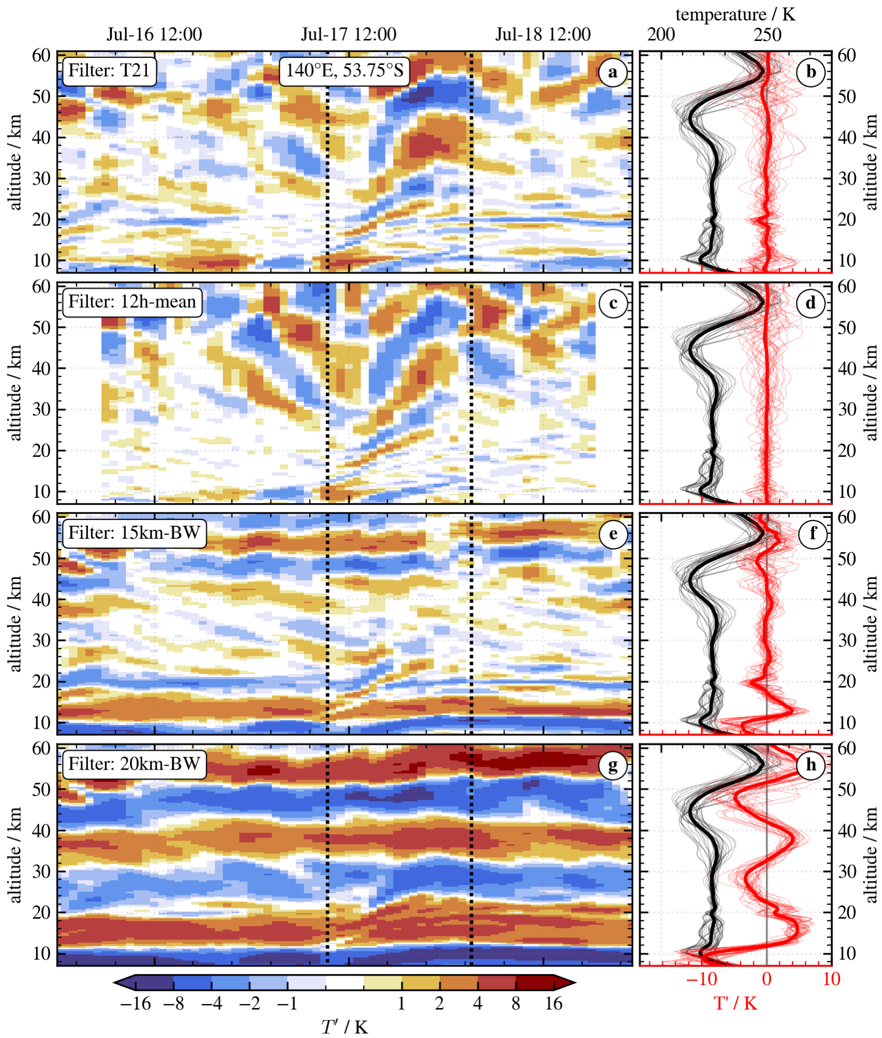

Figure 2. Time-height diagrams of stratospheric ERA5 T' for a location (140°E, 53.75°S) over the Southern Ocean (left column) and corresponding vertical profiles of absolute temperature and temperature perturbations (right column). Thick black and red lines in (b),(d),(f) and (h) are temporal mean profiles of absolute temperature and T', respectively. Thin lines are individual profiles every 2 h. Panels (a) and (b) show temperature perturbations after subtracting the truncated temperature field T21 (horizontally filtered by removing wave numbers larger than 21) of the ERA5 dataset. (c) and (d) show T' after removing a temporal running mean of 12 h. (e) and (f) display the result of a vertical highpass Butterworth filter with a cutoff wavelength $\lambda_{cut} = 15\,\text{km}$ and panels (g) and (h) with $\lambda_{cut} = 20\,\text{km}$.

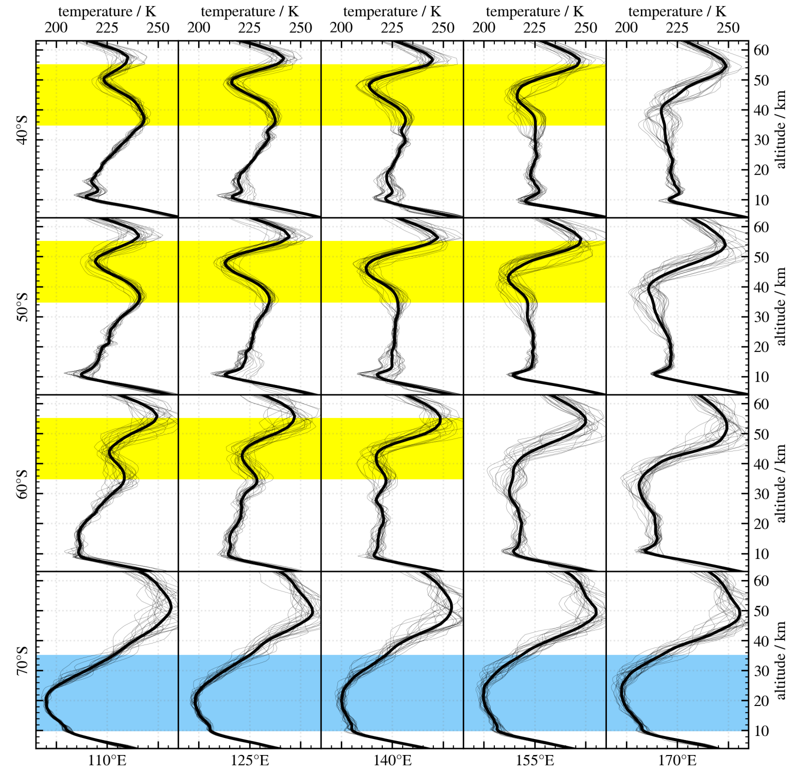

Figure 3. Latitude-longitude matrix of vertical temperature profiles of ERA5 at 20 evenly spaced locations in the Southern Hemisphere. The period July 07, 2014 - July 09, 2014 includes DEEPWAVE research flight RF25. Thick black lines are temporal mean profiles, thin black lines represent individual profiles every 2 h for the 3-day period. The yellow band indicates profiles with a pronounced temperature minimum between 35 and 55 km complicating the application of vertical filters to separate the signal into background and GWs. The blue band marks profiles with a significant temperature decrease in the stratosphere due to the polar vortex.

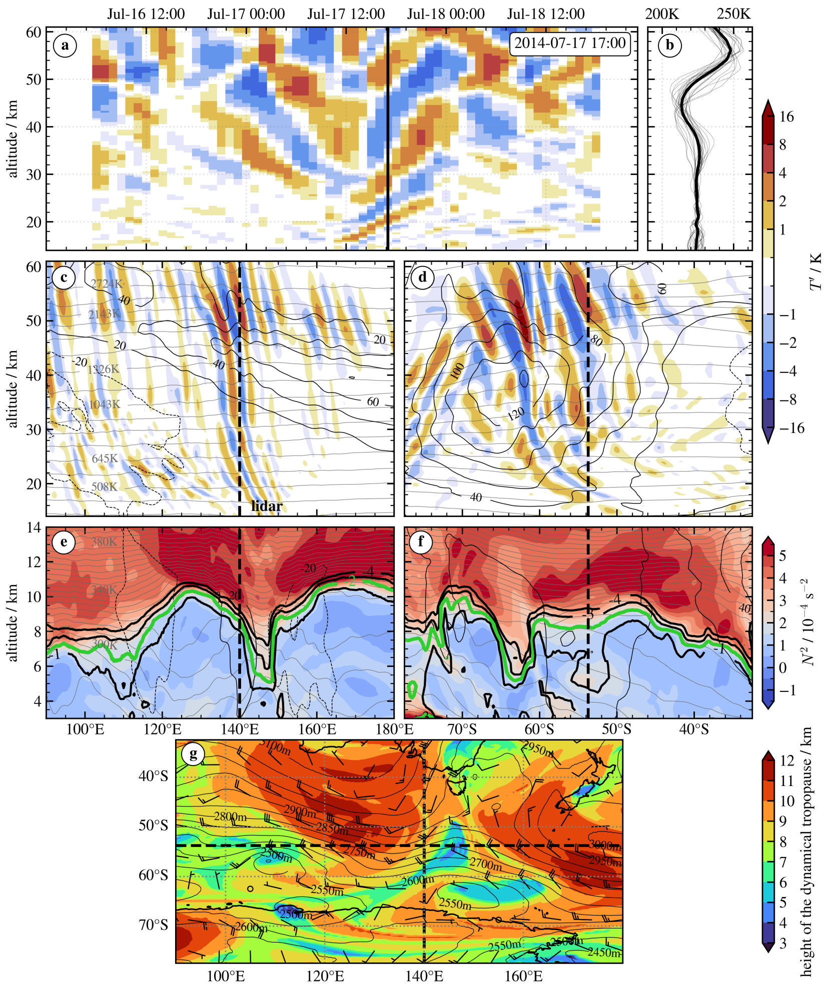

Figure 4. ERA5 overview for a location over the Southern Ocean (53.75°S, 140°E) during research flight RF25 of the DEEPWAVE campaign. Panels (a) and (b) are similar to Figure 2(c) and (d) emulating the measurements of a vertically staring ground-based lidar. Panels (c) and (d) are vertical sections of stratospheric T' along sectors of the latitude circle (c) and meridian (d) of the virtual lidar location. (e) and (f) are corresponding vertical sections of thermal stability N^2 ($10^{-4}\,\mathrm{s}^{-2}$, color-coded), potential temperature (K, thin grey lines), and potential vorticity (1, 2, 4 PVU: black, 2 PVU: green) in the vicinity of the dynamical tropopause. Thin black lines in the vertical sections are zonal (d, f) and meridional (c, e) wind components (solid: positive, dashed: negative). Panel (g) is a horizontal section of the height of the 2 PVU surface (km, color-coded), geopotential height (m, solid lines) and wind barbs at the 850 hPa level. The black vertical line in (a) marks the time (July 17, 2014, 17 UTC) for (c)-(g) and dashed lines in (c)-(g) highlight the location of the virtual lidar and profiles in (a) and (b).

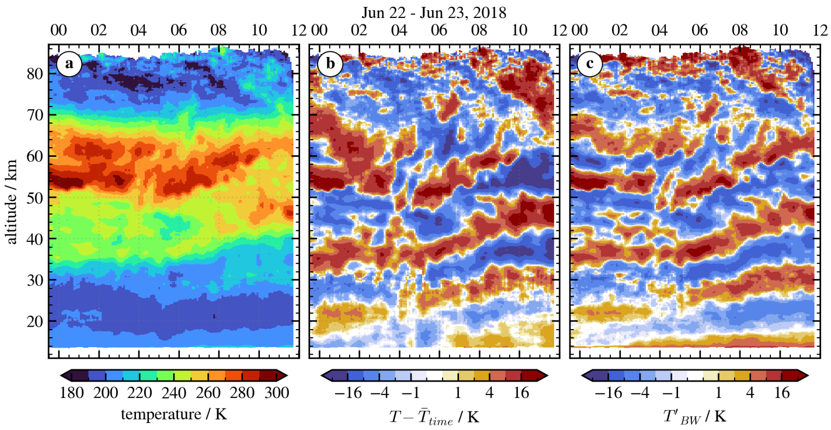

Figure 5. Night-time temperature measurements of CORAL located in Río Grande, Argentina (53.79°S, 67.75°W) from June 22 to 23, 2018. Shown are retrieved temperature profiles (a), temperature perturbations $T' = T - \bar{T}_{time}$ after subtracting a nightly (temporal) mean (b) and T' after applying a vertical high-pass Butterworth filter with a cutoff wavelength of $\lambda_{z,cut} = 20\,\mathrm{km}$ (c).

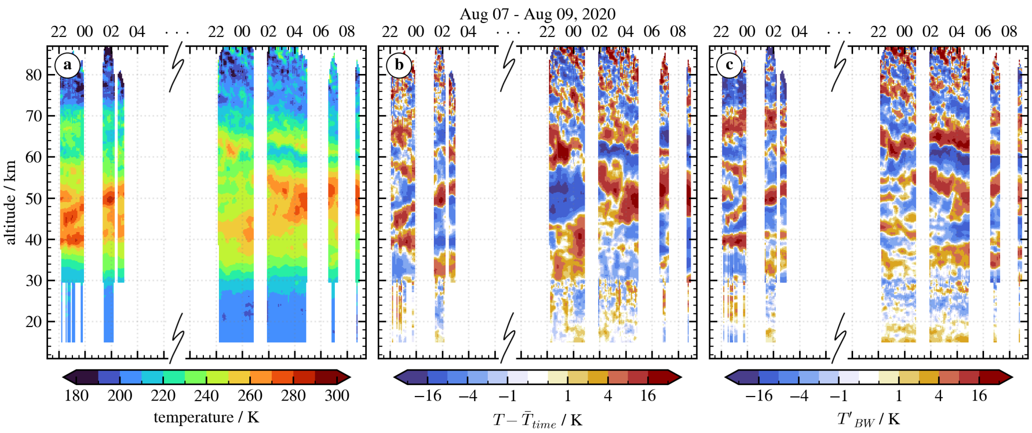

Figure 6. Identical to Figure 5 showing night-time measurements for two consecutive nights from August 7 to 9, 2020. The time frame between the measurements (06:00-20:00 UTC on August 8, 2020) is removed and periods of missing data are related to cloud coverage.

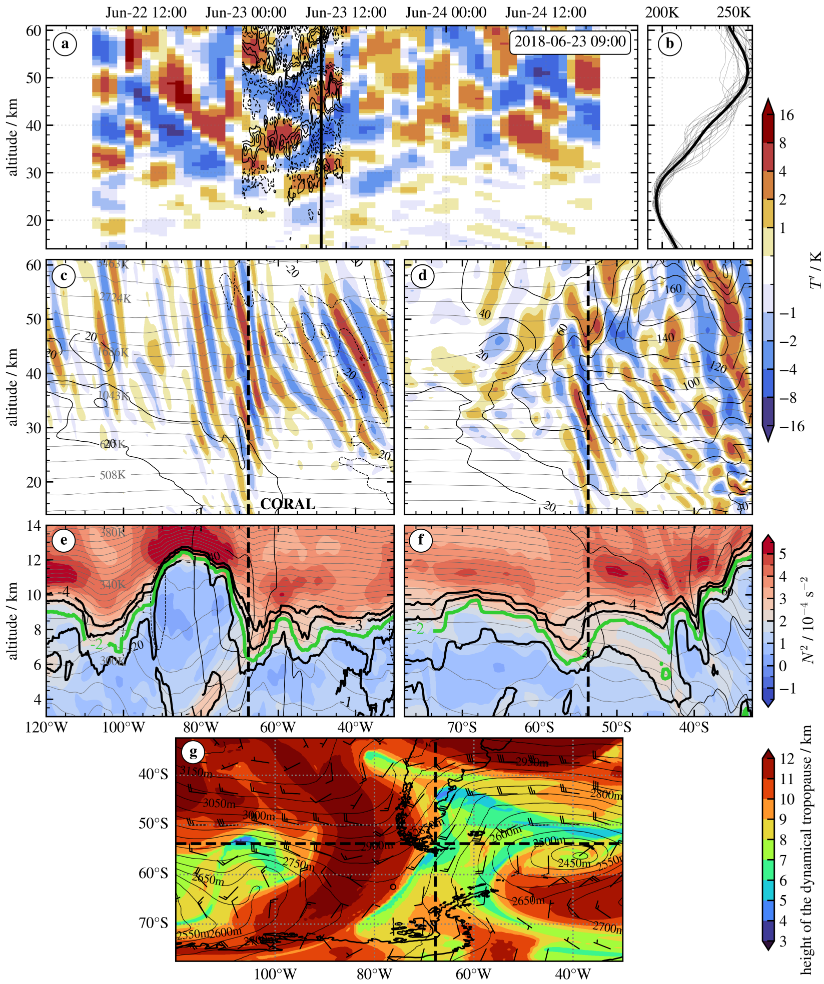

Figure 7. ERA5 overview similar to Figure 4 for CORAL's location and a period around the nightly measurement from June 22 to 23, 2018 in Figure 5. Thin black lines in (a) overlay CORAL observations (solid lines: $T' > 0$, dashed lines: $T' < 0$).

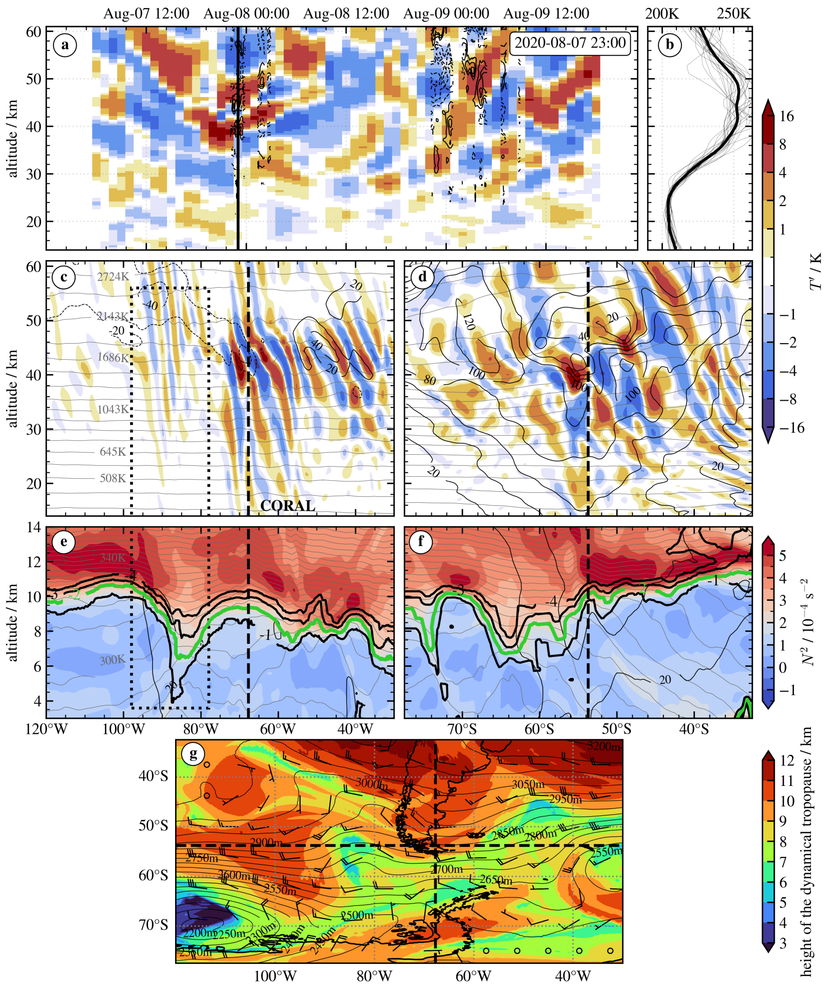

Figure 8. Identical to Figure 7 showing an ERA5 overview for two consecutive nights with CORAL measurements from August 7 to 9, 2020. The dotted rectangle in (c) and (e) frames NOGWs in the stratosphere above an upper-level trough upstream of CORAL's location over the Pacific Ocean.

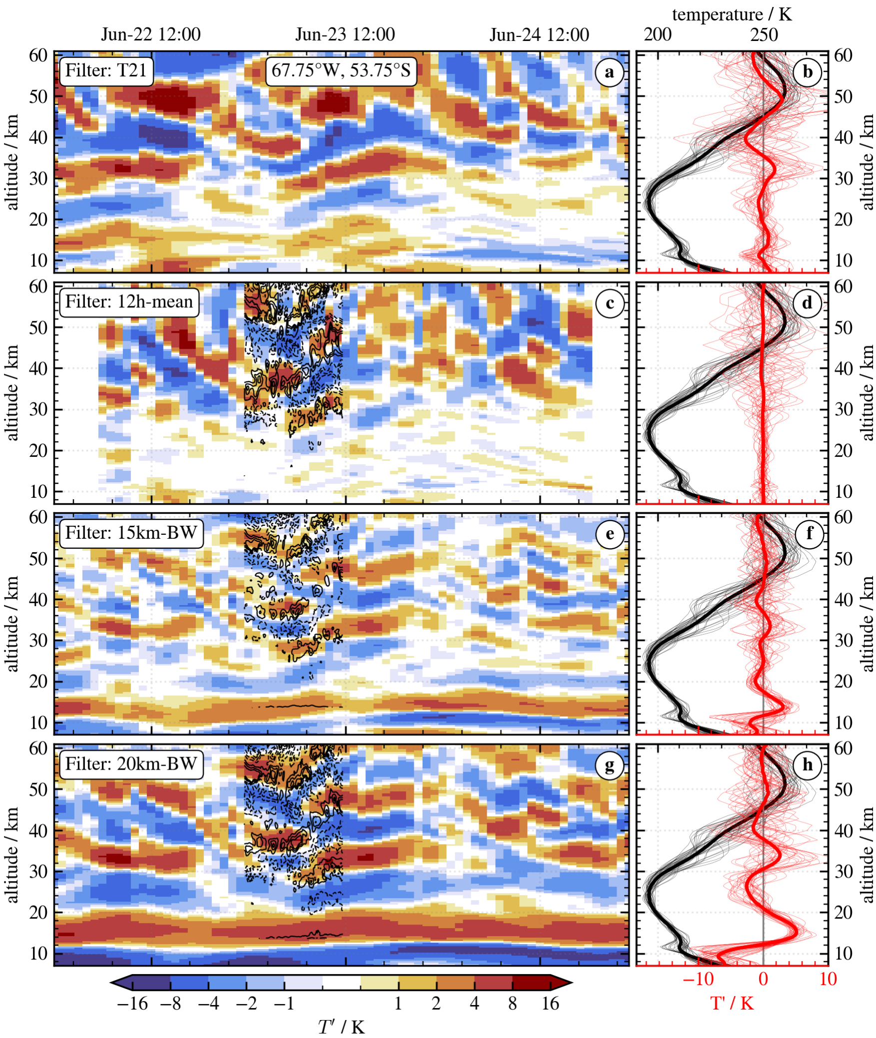

Figure 9. Similar composition as Figure 2 showing time-height diagrams for CORAL's location for a 3-day period in June 2018. Thin black lines show corresponding temperature perturbations from CORAL measurements. Solid lines refer to positive, dashed lines to negative perturbations.

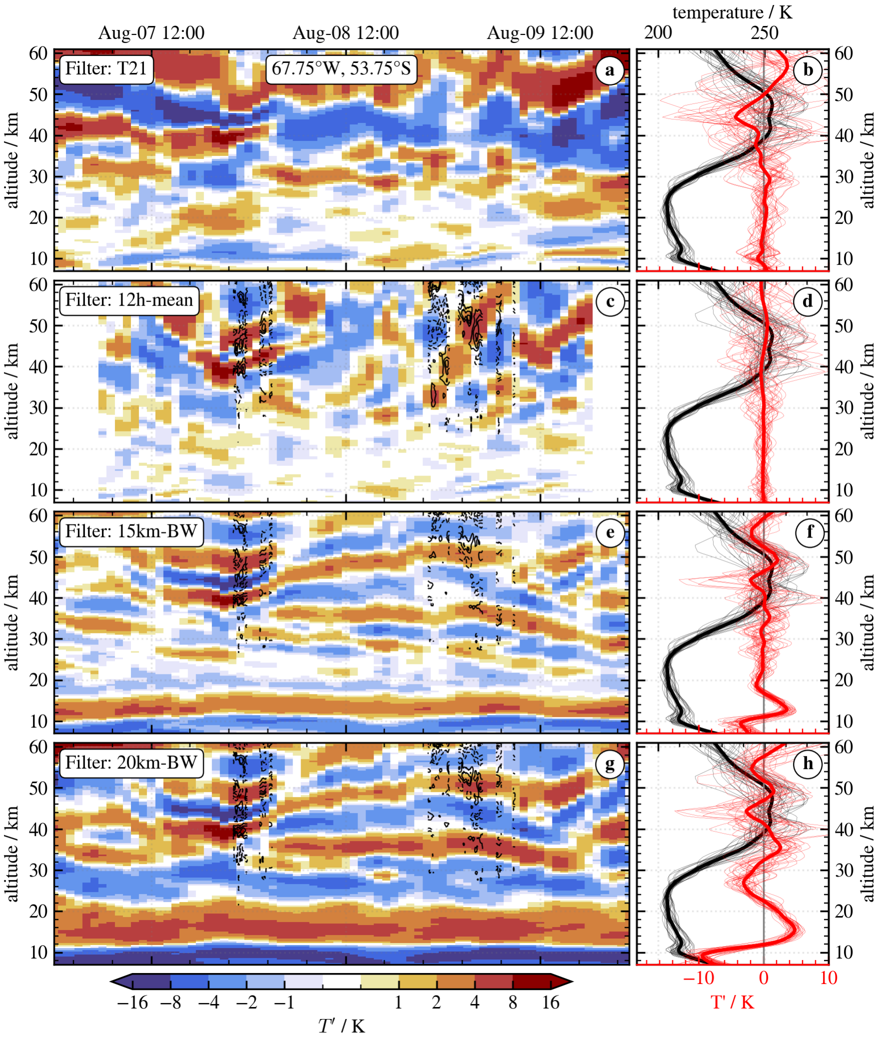

Figure 10. Identical to Figure 9 showing time-height diagrams for CORAL's location for a 3-day period in August 2020 with two consecutive nights with CORAL measurements.

Non-orographic gravity waves in ground-based Rayleigh lidar observations

Michael Binder and Andreas Dörnbrack

Deutsches Zentrum für Luft- und Raumfahrt, Institut für Physik der Atmosphäre, Oberpaffenhofen, Germany

Weßling, November 5, 2023

Key Points:

- Tilted phase lines in temperature measurements of ground-based Rayleigh lidars can be related to a propagating non-orographic GW source
- Tailored compositions of selected meteorological variables guide the interpretation of virtual and actual Rayleigh lidar measurements
- Temporal filtering of temperature is suitable for identifying NOGWs in observations of vertically staring ground-based Rayleigh lidars

Corresponding author: Michael Binder, `michael.binder@dlr.de`

Abstract

Temperature measurements by vertically staring ground-based Rayleigh lidars are often used to detect middle atmospheric gravity waves. In time-height diagrams of temperature perturbations, stationary mountain waves are identifiable by horizontal phase lines. Vertically tilted phase lines, on the other hand, indicate that the wave source or the propagation conditions are transient. Idealized numerical simulations illustrate that and how a wave source moving in the direction of the mean wind entails upward-tilted phase lines. The inclination angle depends on the horizontal wavelength and the wave source's propagation speed. On this basis, the goal is to identify and characterize transient non-orographic gravity waves (NOGWs), e.g., from propagating upper-level jet/front systems, in virtual and actual Rayleigh lidar measurements. Compositions of selected atmospheric variables from a meteorological forecast or reanalysis are thoughtfully combined to associate NOGWs with processes in the troposphere and stratosphere. For a virtual observation over the Southern Ocean, upward-tilted phase lines indeed dominate the time-height diagram during the passage of an upper-level trough. The example also emphasizes that temporal filtering of temperature measurements is appropriate for NOGWs, especially in the presence of a strong polar night jet that implies large vertical wavelengths. During two selected observational periods of the COmpact Rayleigh Autonomous Lidar (CORAL) in the lee of the southern Andes, upward-tilted phase lines are mainly associated with mountain waves and transient background wind conditions. One nighttime measurement by CORAL coincides with the passage of an upper-level trough, but large-amplitude mountain waves superpose the small-amplitude NOGWs in the middle atmosphere.

Plain Language Summary

Atmospheric gravity waves are vertical oscillations of air parcels similar to the wave motion we can observe at the ocean surface. Vertical oscillations imply fluctuations in the air parcel's temperature, so studying these waves high up in the atmosphere is possible by measuring temperature with dedicated ground-based instruments. Different processes can cause gravity waves. Flow over mountains, for example, excites gravity waves and results in a specific pattern in these ground-based measurements, which differs for transient atmospheric conditions or propagating wave sources. In this context, this study aims to identify waves from propagating wave sources in temperature measurements by comparing the measured data to simulated data from weather models. If the modeled data matches the measurements, the entire weather model dataset is used to investigate the atmospheric processes causing the waves. The approach proved practical for a virtual measurement location over the Southern Ocean, where it was possible to associate wave patterns in the upper atmosphere with propagating weather phenomena in the lower atmosphere. However, interpreting actual measurements near the southern Andes mountains is more challenging. Mountain waves dominate the measurements with larger amplitudes, even in the presence of propagating gravity wave sources.

1 Introduction

Observations of gravity waves in the stratosphere and mesosphere, lower thermosphere (MLT) are sparse. Only a small number of satellite instruments provide temperature measurements in this altitude range applicable for gravity wave detection. For example, the High Resolution Dynamics Limb Sounder (HIRDLS) was only active between 2005 and 2008 (Gille et al., 2008). The Sounding of the Atmosphere using Broadband Emission Radiometry (SABER) is part of the Thermosphere-Ionosphere-Mesosphere Energetics and Dynamics (TIMED) mission and still operational, but only provides continuous measurements for the latitude range 50°N-50°S (Mlynczak, 1997; Ern et al., 2018). Other instruments are the Cross-Track Infrared Sounder (CrIS) on the Suomi National

Polar-Orbiting Partnership (NPP) satellite that launched on October 2011 (Goldberg et al., 2013) or the nadir-sounding Atmospheric Infrared Sounder (AIRS) on board of NASA's Aqua satellite (Hoffmann & Alexander, 2009; Hoffmann et al., 2013; Eckermann et al., 2019; Hindley et al., 2019, 2020). In the case of AIRS, measurements are available globally, but the temporal resolution is coarse, because each location is only observed twice a day. In addition, the instrument is sensitive to just a portion of the GW spectrum due to the so-called observational filter (e.g., Preusse et al., 2002; Alexander et al., 2010). However, high-temporal resolution and high-cadence of observations are potentially important for detecting gravity waves almost continuously and distinguishing whether they are stationary or transient modes, which in turn gives an indication of their sources (e.g., Reichert et al., 2021).

Vertical temperature profiles from ground-based Rayleigh lidars, often displayed in time-height diagrams, are one alternative available on a regular basis providing much higher vertical and temporal resolutions. Such observations, of course, are limited to a single location (point observation) and are possible only under clear skies and often only at night. Commonly, ground-based Rayleigh lidars are used to monitor middle atmospheric gravity wave activity with the aim to estimate the momentum deposition (wave drag) that drives part of the global atmospheric circulation (e.g., N. Kaifler et al., 2020). In many cases, the lidar observations of temperature and the derived temperature perturbations are compared with results from global circulation models (e.g., Le Pichon et al., 2015; Ehard et al., 2018; Strelnikova et al., 2021; Gisinger et al., 2022). Most analyses are carried out in a statistical manner to determine, among other things, mean vertical wavelengths, periods, amplitudes, and the seasonal variability at different sites (e.g., Yamashita et al., 2009; B. Kaifler et al., 2015; Zhao et al., 2017; Chu et al., 2018; Strelnikova et al., 2021; Reichert et al., 2021). Sometimes, the question arises about the actual atmospheric processes leading, for example, to an observed upward or downward phase progression in the time-height diagrams. To this end, we propose a possible, hopefully appropriate, and reasonable basis for identifying non-orographic gravity waves (NOGWs) in these ground-based Rayleigh lidar measurements by advocating specific displays of selected atmospheric variables retrieved from high-resolution numerical weather prediction (NWP) models. These variables are combined into a single composite figure for each available time to provide guidance on possible gravity wave sources and background conditions associated with weather systems.

We introduce and illustrate our approach by means of a case study on NOGWs over the Southern Ocean (Dörnbrack et al., 2022) during the DEEPWAVE campaign 2014 (Fritts et al., 2016). Generally, transient gravity waves can be generated by a multitude of atmospheric processes like deep convection (e.g., Lane et al., 2001), upper-level front/jet systems (e.g., Plougonven & Zhang, 2014), by an unbalanced polar night jet (PNJ, e.g., Dörnbrack et al., 2018), or by sudden pulsations like volcano eruptions (e.g., Wright et al., 2022). Here, Dörnbrack et al. (2022) propose that the stratospheric flow across zonally propagating upper-level troughs excites non-orographic, transient gravity waves like the flow over mountains excites stationary gravity waves. This connection is evident from the nearly simultaneous zonal propagation of Rossby waves over the Southern Oceans with the occurrence of transient gravity waves in the middle atmosphere. Their findings confirm the synoptic analyses of Hendricks et al. (2014) who correlated the baroclinic growth rates in the troposphere with gravity wave-induced stratospheric temperature perturbations near 60°S, also called the stratospheric gravity wave belt.

Far from any orographic gravity wave sources, the area studied by Dörnbrack et al. (2022) over the Southern Ocean south of Australia is ideal for identifying NOGWs. However, no ground-based Rayleigh lidar measurements exist for this or a similar location, so we also use our approach in the context of observations by the Compact Rayleigh Autonomous Lidar (CORAL) for the middle atmosphere (N. Kaifler et al., 2020; B. Kaifler & Kaifler, 2021) in the lee of the Andes in South America. Here, the predominant amplitudes are due to mountain waves excited by the westerly flow over the Andes and characterized by nearly horizontal phase lines in the time-height diagrams, indicating the quasi-steadiness of the stationary mountain waves (Reichert et al., 2021). On the other hand, there are numerous examples where stratospheric phase lines in the time-height diagrams are inclined; see and scroll the daily observations displayed in CORAL's measurement calendar under `http:\\container.kaifler.net/coral/index.php`. The reason for these inclinations can be manifold: transient ambient winds in the troposphere or stratosphere that affect the excitation and propagation conditions of mountain waves are one possibility. Transient gravity wave sources associated with eastward propagating mid-latitude weather systems in the Southern Hemisphere, as introduced above, are another (e.g., Dörnbrack et al., 2022; Plougonven & Zhang, 2014; Hendricks et al., 2014).

Although the idea of the excitation mechanism of NOGWs proposed by Dörnbrack et al. (2022) resembles the excitation of mountain waves, their actual appearance in time-height diagrams of ground-based Rayleigh lidar observations will be significantly different from that of mountain waves. The propagation of the wave source leads to an inclination of the phase lines. Therefore, Section 2 first deals with how transient NOGWs appear in time-height diagrams and how they could be interpreted utilizing idealized numerical simulations. Subsequently, Section 3 applies the conclusions of the previous section and proposes tailored visualizations of tropospheric and stratospheric flow quantities from state-of-the-art numerical weather prediction (NWP) data to identify and interpret NOGWs for a virtual lidar location over the Southern Ocean. We use the recent reanalyses version 5 (ERA5) of the European Centre for Medium-Range Weather Forecasts (ECMWF). ERA5 is computed by the Integrated Forecast System (IFS Cycle 41r2) (Hersbach et al., 2020). The section also discusses the appropriate filtering of temperature measurements from a vertically staring ground-based Rayleigh lidar before moving from the ideal location for investigating NOGWs far from orography to actual measurements in the lee of the southern Andes. Section 4 presents the same analysis for two periods with CORAL measurements showing similar tilted phase line signatures as the idealized simulations, and Section 5 summarizes and concludes this paper.

2 Lidar observations in idealized numerical simulations

A complete characterization of stationary mountain waves by ground-based Rayleigh lidar observations is very demanding (e.g., Strelnikova et al., 2021; Reichert et al., 2021). In a purely steady flow, the horizontal phase velocity of mountain waves vanishes ($c_{px} = 0$) together with the ground-based frequency ($\omega = 0$). As a result, phase lines of temperature perturbations derived from the ground-based Rayleigh lidar observations appear horizontal and only the vertical wavelength λ_z can be derived from the time-height diagrams. There is no information about horizontal scales (e.g., Dörnbrack et al., 2017; Reichert et al., 2021).

Dörnbrack et al. (2017) used idealized numerical simulations to show time-height diagrams of the atmospheric response of uniform flow over individual two-dimensional mountains of different widths. The simulated steady, horizontal phase lines of temperature perturbations recorded in the lee of the mountains resemble those found in many CORAL observations. Here we take a step further and employ an idea and the numerical development introduced by Wedi and Smolarkiewicz (2004); Prusa and Smolarkiewicz (2003). Prusa and Smolarkiewicz presented idealized numerical simulations of a moving frictionless lower boundary surface (such as a flexible membrane) in their numerical model that excites vertically propagating gravity waves. If the wave source propagates uniformly in one direction, the gravity waves have the same properties as stationary mountain waves within the frame of reference that moves with their source.

2.1 Setup and comparison of three different EULAG simulations

Here, results are presented that are simulated with the nonlinear EUlerian/semi-LAGrangian fluid solver (EULAG) applying a similar numerical set-up as in Prusa and Smolarkiewicz (2003). EULAG solves the anelastic set of equations (Lipps & Hemler, 1982) consisting of the momentum equations for the Cartesian velocity components (u, v, w), the thermodynamic equation for the potential temperature perturbation $\Theta' = \Theta - \Theta_0$, and the mass continuity equation in generalized time-dependent coordinates (Prusa & Smolarkiewicz, 2003, Eqs. 4-7). A comprehensive description of the advection scheme is given in P. K. Smolarkiewicz and Margolin (1997, 1998). In addition, EULAG features a robust elliptic solver (P. Smolarkiewicz & Margolin, 1993) and a generalized coordinate formulation that enables grid adaptivity technology (Wedi & Smolarkiewicz, 2004; Prusa et al., 2008; Kühnlein et al., 2012).

The anelastic equations are written such that hydrostatically balanced reference profiles $u_0(z)$, $v_0(z)$, $\rho_0(z)$, $p_0(z)$, and $\Theta_0(z)$ are subtracted from the prognostic variables (Clark, 1977; Lipps & Hemler, 1982). For the idealized simulations presented here, the thermodynamic reference profiles define an isothermal atmosphere with constant stability according to (Bacmeister & Schoeberl, 1989):

$$\begin{aligned} &\Theta_0(z) = \Theta_{00} e^{\frac{z}{H_\Theta}} \quad \text{with} \quad \Theta_{00} = T_{00}\left(\frac{p_0}{p_{00}}\right)^{R/c_p}, \quad \text{and} \quad H_\Theta = \frac{g}{N^2} = \frac{c_p T_{00}}{g}, \\ &\rho_0(z) = \rho_{00} e^{-\frac{z}{H_\rho}} \quad \text{with} \quad H_\rho = \frac{RT_{00}}{g}, \quad \text{and} \\ &p_0(z) = p_{00} e^{-\frac{z}{H_\rho}} \end{aligned} \tag{1}$$

with the Brunt-Väisälä frequency $N = 0.02\,\mathrm{s^{-1}}$, the specific gas constant $R = 287.04\,\mathrm{J\,kg^{-1}\,K^{-1}}$, and the specific heat capacity at constant pressure $c_p = \frac{2}{7}R$. The values at the lower boundary, an isentropic surface of $\Theta_{00} \approx 361\,\mathrm{K}$, are: $T_{00} = 239.39\,\mathrm{K}$, $p_{00} = 235\,\mathrm{hPa}$, and $\rho_{00} = 0.3454\,\mathrm{kg\,m^{-3}}$. These values are characteristic for the stably stratified lower stratosphere at mid-latitudes (Gettelman et al., 2011). The exponential profiles (1) avoid physical restrictions towards higher altitudes and are, thus, well suited for investigating deep gravity wave propagation.

The results of the 3D numerical simulations presented in Figure 1 are initialized with zero potential temperature perturbations Θ' and vertical profiles of the three velocity components $(u_0(z), 0, 0)$. The zonal wind profiles $u(z)$ are either uniform with magnitudes of $u_0 = 20$ or $45\,\mathrm{m\,s^{-1}}$ (purple profiles in Figures 1a and c). In a third simulation, $u_0(z)$ is a superposition of a constant wind with the tropopause and polar night jet streams, whose shapes are both based on a Gaussian distribution:

$$u_{jet}(z) = u_{jet,max} e^{-\frac{1}{2}\left(\frac{z - z_{jet}}{\sigma_{jet}}\right)^2} \tag{2}$$

with a maximum wind speed $u_{jet,max}$ at z_{jet} and a standard deviation σ_{jet}. The tropopause jet is centered at the lower boundary with $\sigma_{jet} = 5\,\mathrm{km}$ and the PNJ is centered at $z_{jet} = 40\,\mathrm{km}$ with $\sigma_{jet} = 13\,\mathrm{km}$ (purple line in Figure 1e).

A time-dependent lower boundary (Prusa et al., 1996; Wedi & Smolarkiewicz, 2004) is implemented to mimic the stratospheric flow across a propagating upper-level trough. The physical idea of this approach was already suggested by Pfister et al. (1993) for convective thermals and has been simulated previously by Prusa and Smolarkiewicz (2003). The shape of the upper-level trough or, more precisely, the shape $z_s(x,t)$ of a frictionless, isentropic surface that dips and rises above the upper-level trough can be approximated by an $1 + \cos(\frac{\pi}{4L}x)$ shape with the width L. The function $z_s(x,t)$ drops to 0 for $|\frac{x}{4L}| = 1$, so the surrounding field can be set to 0 for $|\frac{x}{4L}| \le 1$ without sacrificing its continuity and differentiability, an essential prerequisite for the numerically stable implementation of a transient boundary condition in the model. Prusa and Smolarkiewicz

(2003) already used a form of the above cosine function to mimic a moving tropopause fold in simplified 2D simulations with EULAG. Here, we use a different variant:

$$z_s(x,t) = \begin{cases} -\frac{h_m}{16}\left(1+\cos(\frac{\pi}{4L}(x-x_0(t))\right)^4 & \text{for} \quad |\frac{x-x_0(t)}{4L}| < 1 \\ 0 & \text{for} \quad |\frac{x-x_0(t)}{4L}| \geq 1, \end{cases} \tag{3}$$

where $h_m = 300\,\mathrm{m}$, $x_0(t)$ is the time-dependent center of the undulated lower boundary that moves uniformly with a speed c_{tf}. The quantity $c_{tf} = 0$ for the results in the upper row of Figure 1 and $c_{tf} = 13.88\,\mathrm{m\,s^{-1}}$ for the middle and bottom panels. Similar versions of Equation (3) have already been used for prescribing idealized orography (see, Epifanio & Durran, 2001; Metz & Durran, 2021).

Our idealized simulations start with a flat surface $z_s(x,0) = 0$ and homogeneous horizontal flow instead of initializing the flow field with a potential flow over an already implemented lower boundary $z_s(x,0)$ according to Eq. (3). The amplitude h_m of the lower model surface $z_s(x,t)$ slowly changes for a given period $t_{spinup} = 12$ h by multiplying h_m with $tt^3\left(10 - 15tt + 6tt^2\right)$, where $tt = t/t_{spinup}$ for $t \leq t_{spinup}$ in all numerical simulations. The effect of this transient initialization can be seen in the decreasing height z_s during the first 12 hours in Figure 1(b).

Figure 1 illustrates how a transient gravity wave source alters the inclination of phase lines of gravity wave-induced stratospheric temperature perturbations in time-height diagrams. Measurements of a vertically pointing ground-based lidar are emulated by tracking the vertical temperature profile at $x = 7500\,\mathrm{km}$ in the computational domains. Figure 1(a), (c), and (e) show the wave-induced perturbations in the middle plane of 3D computational domain for three different simulations, Figure 1(b), (d), and (f) show the corresponding time-height diagrams. The first row emulates a mountain wave scenario with a non-propagating obstacle at the lower boundary. After 72 h simulation time, vertically propagating inertia-gravity waves are located above the upside-down mountain and extend downstream (Figure 1(a)). In the corresponding time-height diagram, the phase lines of the mountain waves appear as horizontal stripes whose amplitude is increasing with height until they are numerically damped in the sponge layer starting at $z = 48\,\mathrm{km}$ altitude.

In contrast, phase lines in the time-height diagrams differ significantly for simulations with a moving lower boundary (middle and bottom rows of Figure 1). The phase lines tilt upward for a wave source moving in the same direction as the background wind (Figure 1(d) and (f)). The steepness of the phase lines depends on the vertical wind profile. For an idealized stratospheric wintertime wind profile, the phase lines' angle between 30 and 40 km in the time-height diagram in Figure 1(f) is approximately 10 km over 6-7 h. Due to the presence of the PNJ, the phase lines become steeper above 20 km as the vertical wavelength λ_z is proportional to u/N (Figure 1(e)).

2.2 Derivation of wave properties in time-height diagrams

Do the results of the transient wave source allow for a derivation of horizontal wave properties? Yes and no! Clearly, tilted phase lines enable the quantification of a ground-based period T from the time-height diagram, but linking this period to wave properties depends on the wave source and on the atmospheric background conditions. Multiple phenomena could explain upward-tilted phase lines in ground-based lidar observations, so their interpretation requires additional knowledge on the prevailing atmospheric processes and the synoptic situation. Examples are:

- downward propagating wave packets caused by reflection at turning levels (e.g., Schoeberl, 1985),
- wave breaking in the upper atmosphere exciting secondary waves that travel up and down from their source region (e.g., Dörnbrack et al., 2017; Vadas et al., 2003),

- transient background conditions mainly in the form of a varying wind speed or direction (e.g., Chen et al., 2005, 2007; Portele et al., 2018),
- a gravity wave source moving in the same direction as the background wind as illustrated in Figures 1d and 1f.

For this work, we explore the last possibility and focus on the gravity wave characterization for the simplified case of a constant wind profile shown in Figure 1c and 1d following the terminology and derivations of Gill (1982); Fritts and Alexander (2003); Dörnbrack et al. (2017). To recap, a constant stratification with N was used for all simulations starting at the 361 K isentropic surface simplifying the dispersion relation for Boussinesq flows to

$$\hat{\omega}^2 = N^2 \frac{k^2}{k^2+m^2} + f^2 \frac{m^2}{k^2+m^2} \tag{4}$$

with $\hat{\omega}$ being the intrinsic frequency and $f = -1.195\,10^{-4}\,\mathrm{s}^{-1}$ is the Coriolis parameter to consider the influence of Earth's rotation at a latitude of 55°S. A constant background wind leads to a ground-based frequency

$$\omega = \hat{\omega} + uk, \tag{5}$$

and, in addition, Gill (1982) defines the useful aspect ratio

$$\alpha = \frac{\text{vertical scale}}{\text{horizontal scale}} = \frac{\lambda_z}{\lambda_x} = \sqrt{\frac{\hat{\omega}^2 - f^2}{N^2 - \hat{\omega}^2}}, \tag{6}$$

which simplifies the approximation of $\hat{\omega}$ for the relevant hydrostatic rotating wave regime to

$$\hat{\omega}^2 \approx f^2 + N^2\alpha^2. \tag{7}$$

As labeled in Figure 1d, the vertical distance between troughs or ridges in the time-height diagram yields the vertical wavelength $\lambda_z = 9.25\,\mathrm{km}$ and a wavenumber $m = 2\pi/\lambda_z$, the horizontal distance at 40 km altitude provides a period $T = 13.92\,\mathrm{h}$ and ground-based frequency ω. How can this frequency be interpreted? Dörnbrack et al. (2017) clarify that in the presence of a background wind this question can only be answered by consulting further information or by proceeding with assumptions.

For the case of a propagating upper-level trough, we can assume a stationary wave field within a moving reference frame. Then, the tilt of the phase lines within the ground-based lidar observation depends on the propagation speed of the gravity wave source and the horizontal wavelength λ_x. A constant propagation speed c_{tf} leads to $\lambda_x = T \cdot c_{tf} = 695\,\mathrm{km}$, which is in the range of wavelengths labeled in the vertical cross-section (Figure 1c) at the same height with $\lambda_x = 525\,\mathrm{km}$ to $712\,\mathrm{km}$. The ratio of λ_z to λ_x gives $\alpha = 0.0133$. The angle ϕ between lines of constant phases and the z-axis is

$$\phi = \tan^{-1}\left(\frac{\lambda_x}{\lambda_z}\right) = 89.24°. \tag{8}$$

From Equation (7) $\hat{\omega} \approx 2.92\,10^{-4}\,\mathrm{s}^{-1}$, so $\hat{\omega}$ is of $\mathcal{O}(f)$ and $\hat{\omega} \geq f$, which is in full compliance with the hydrostatic rotating wave regime described by Gill (1982). It follows the intrinsic horizontal group velocity

$$c_{gx} \approx \frac{N^2\alpha}{m\sqrt{f^2 + N^2\alpha^2}} \approx -26.9\,\mathrm{m\,s^{-1}} \tag{9}$$

with a negative m for upward propagating waves and the vertical group velocity

$$c_{gz} \approx -\alpha c_{gx} \approx 0.36\,\mathrm{m\,s^{-1}} \tag{10}$$

Again, this is consistent with inertia-gravity waves in the hydrostatic rotating wave regime, where c_{gx} does not offset the background wind resulting in a downstream propagation of these inertia-gravity waves (e.g., Dörnbrack, 2002). Knowledge of $u = 45\,\mathrm{m\,s^{-1}}$

allows the calculation of $U_{MW} = U - c_{tf} = 31.12\,\mathrm{m\,s^{-1}} > |c_{gx}|$, indicating a downstream propagation of gravity waves relative to the propagating upper-level trough. Considering the superimposed propagation of the wave source, the ground-based group velocity is $c_{Gx} = U + c_{gx} = 18.1\,\mathrm{m\,s^{-1}}$ and according to the above assumptions, the ground-based horizontal phase velocity must be identical to the velocity of the wave source ($c_{Px} = c_{tf}$).

The vertical propagation of the gravity waves is independent of the background wind. According to c_{gz} in Equation (10), it takes approximately 31 hours until the gravity waves reach an altitude of 40 km above z_s, but c_{gz} is very sensitive to the derived horizontal and vertical wavelengths: A $\lambda_x = 525\,\mathrm{km}$ (lower limit based on Figure 1c) with the same λ_z already results in 22.6 hours and higher λ_z further increases c_{gz}. The time-height diagram in Figure 1b confirms these estimates: Maximum amplitudes at 40 km appear roughly 20 to 30 hours after the completed spin-up of the simulation.

3 Lidar observations of non-orographic gravity waves in ERA5

After a first investigation of the phase lines' shapes in time-height sections due to transient gravity wave excitation by means of idealized numerical simulations, the approach presented in this and the following section goes one step further: We attempt to identify patterns of NOGWs from a propagating source in actual ground-based Rayleigh lidar measurements of stratospheric and mesospheric temperatures. To this end, we propose to combine time-height sections that emulate the measurements with a series of meteorological analyses in a single figure utilizing state-of-the-art NWP model data as, e.g., the ERA5 reanalysis dataset (Hersbach et al., 2020). As shown by Gupta et al. (2021); Pahlavan et al. (2023), ERA5 is the first global reanalysis that partially resolves the gravity wave spectrum. Here, the 1-hourly ERA5 analyses on model, pressure, and potential vorticity levels at a horizontal resolution of $0.25^\circ \times 0.25^\circ$ ($\approx 30\,\mathrm{km}$) are used. For the native output grid, this corresponds to a minimum resolved wavelength of about 60 km. However, due to scale-selective hyperdiffusion, the effective minimum physical wavelength will be quite larger (Polichtchouk et al., 2023). ERA5 employs a total of 137 unevenly spaced full model levels. Level spacings above the troposphere vary from about 250 m in the lower stratosphere to about 1500 m near 1 hPa (Ehard et al., 2018). Alternatively, and not used in this study, hourly fields of the IFS high-resolution short-term forecasts and the 6 hourly analyses could be combined to visualize the diurnal cycle of the meteorological fields.

We will discuss selected CORAL measurements in Section 4, but it can be anticipated that the presence of mountain waves due to CORAL's proximity to the Andean Mountain Range complicates the identification of NOGWs. Ideal and best placed to obtain suitable observations of NOGWs would be a lidar station far from any orography. For example, to investigate the origins of the gravity waves found in the stratospheric gravity wave belt around 60°S (e.g., Hendricks et al., 2014; Dörnbrack et al., 2022), a place in the Southern Ocean would be perfect. Though no such instruments exist, it is possible to emulate the measurements of a vertical starring ground-based lidar at such a location with the model data. Since Dörnbrack et al. (2022) documented the spatial and temporal evolution of transient NOGWs over the Southern Ocean during research flight RF25 of the DEEPWAVE campaign 2014, we use their groundwork to determine a virtual lidar location that captures these waves in the respective period. By means of this case study, Section 3a establishes a guideline for retrieving NOGWs in temperature time-height diagrams before Section 3b introduces a composite figure for investigating the meteorological processes leading to the gravity wave signal.

3.1 Gravity wave retrievals in time-height diagrams

In Section 2, potential temperature and temperature perturbations are obtained by subtracting the prescribed vertical ambient profiles of the idealized simulations. This background state is unknown when transitioning to measurements of the real atmosphere. For time-height temperature diagrams from vertically staring ground-based lidars, one must rely on, e.g., the temporal mean temperature or vertical spectral filtering (e.g., Ehard et al., 2015; Strelnikova et al., 2021) to obtain the background state. Data gaps often prevent the application of temporal spectral filtering. Figure 2 illustrates how these different filters considerably alter the appearance of gravity waves, especially NOGWs, in time-height diagrams.

Since the ERA5 dataset is based on ECMWF's IFS, a spectral model, obtaining model fields truncated at a specific spectral resolution is possible. For example, the T21-field only includes wavenumber 21 and smaller, all larger wavenumbers are removed. Following Dörnbrack et al. (2022), we use T21 as the background field and obtain temperature perturbations by subtracting it from the full temperature. This procedure mimics spatial horizontal filtering and is a suitable approach to separate the temperature field into a background state comparable to the background of an idealized simulation and perturbations. Figure 2(a) displays the resulting temperature perturbations for a virtual lidar location in the Southern Ocean at 140°E and 53.75°S. Relatively large amplitudes between the dotted vertical lines stand out because it is the only period with a vertically connected wave signal throughout the stratosphere. The upward tilt of the corresponding phase lines is apparent and we can anticipate that these are NOGWs above an eastward propagating upper-level trough as described by Dörnbrack et al. (2022). Their vertical wavelength is small in the lower stratosphere (≈ 6 km) and significantly increases towards higher altitudes (≈ 20 km above 30 km).

Figure 2(c) now introduces a first filter option that is also reproducible with actual point observations of a vertically starring ground-based Rayleigh lidar. The vertical temperature profile is subtracted by a 12 h running mean, which effectively removes the temperature background but also filters spatially stationary signatures like mountain waves persisting for multiple hours. However, this approach is valuable for investigating transient NOGWs with tilted phase lines in time-height diagrams. The overall wave pattern is similar to the horizontal filtering in Figure 2(a) and the gravity wave between the dotted lines is captured throughout the entire altitude range.

In contrast, a vertical Butterworth filter with a cutoff wavelength of $\lambda_{z,cut} = 15$ km (Figure 2(e)) suppresses the large wavelengths in the upper stratosphere, so the NOGWs are only observable up to an altitude of roughly 30 km. Ehard et al. (2015), Reichert et al. (2021), or Strelnikova et al. (2021) use $\lambda_{z,cut} = 15$ km for studying gravity waves in the stratosphere and mesosphere but Reichert et al. (2021) also state that vertical wavelengths may exceed 15 and even 20 km in the presence of a strong polar night jet. Figure 2 substantiates this finding and illustrates in panels (g) and (h) why increasing $\lambda_{z,cut}$ to 20 km is not generally applicable. Horizontal phase lines persisting for the entire period with a vertical wavelength of roughly 20 km dominate the time-height diagram in Fig. 2(g). A transient wave signal with tilted phase lines between the dotted lines is barely visible. The explanation of these broad phase lines follows from panel 2(f). The mean absolute temperature (thick black line) has a pronounced minimum below the stratopause. This minimum between 35 and 55 km persists for the entire period and results in a pronounced bias (mean T' in Panel 2(h)) of the vertical 20 km Butterworth filter. Combined with tropopause and stratopause, it creates stationary temperature perturbations with a λ_z between 20 and 25 km and amplitudes of 4-10 K. Small biases also exist for the 15 km Butterworth filter in panel 2(f) at the tropopause (10 km) and stratopause (55 km) level, but the temperature minimum in the upper stratosphere mainly affects the 20 km filter.

Figures 9 and 10 in the appendix complement the comparison of different filters showing ERA5 time-height diagrams for CORAL's location in the vicinity of the Andes Mountains for two periods with measurements. Here, the vertical background temperature profiles do not show a pronounced minimum below the stratopause, and the Butterworth filters in the respective panels (e) and (g) prove helpful for identifying horizontal phase lines of stationary mountain waves.

Figure 3 presents additional vertical profiles of absolute temperature for 20 different locations in the Southern Hemisphere outlining the spatial distribution of the temperature minimum in the upper stratosphere for the July 2014 period. The virtual lidar location of Figure 2 is right in the center of the regular latitude-longitude grid. The temperature minimum is widely spread towards the north and west of the virtual lidar location but also exists southward and eastward in the immediate surroundings. The pattern becomes less pronounced towards the southeast and completely vanishes within the polar vortex indicated by the blue shading, highlighting the cold stratospheric temperatures between 10 and 35 km.

Without going into further details on the associated atmospheric processes (consult the discussion about planetary waves in Section 5b of Gisinger et al. (2017)), Figure 3 demonstrates that the temperature minimum below the stratopause is not a local phenomenon but a widespread feature of the background temperature profile at the time that can significantly affect the gravity wave retrieval. More specifically, ambient profiles modified by large-scale atmospheric processes may limit the gravity wave retrieval with vertical filters (see also, e.g., Rapp et al., 2018; Harvey & Knox, 2019). Being insensitive to these patterns of the vertical background temperature profile is a clear advantage of the temporal filtering in Figure 2(c) and (d) and makes it particularly helpful to detect transient gravity waves with large vertical wavelengths in the presence of the PNJ. Therefore, the 12 h running mean will be the foundation for the ERA5 composition introduced in the following subsection to investigate NOGWs in the context of ground-based Rayleigh lidar measurements. However, other filters may be considered for different applications.

3.2 ERA5 overview for a virtual lidar location over the Southern Ocean

In the previous subsection, we elaborated a suitable retrieval for transient NOGWs in time-height diagrams from vertically staring ground-based Rayleigh lidar instruments. Now, we complement these observed time-height sections of temperature perturbations with different meteorological analyses in a single figure to facilitate the interpretation of the measurements. Figure 4 is composed out of seven different panels based on 1-hourly ERA5 reanalyses. Similar to panels (c) and (d) in Figure 2, panel (a) of Figure 4 is the time-height diagram that emulates the lidar measurements showing temperature perturbations after subtracting a 12 h running mean and Figure 4(b) is the absolute temperature profile. The black line in Figure 4(a) refers to the timestamp visualized in panels (c) to (g).

In Figure 4 and in following figures of the same kind, panels (c) to (f) display vertical sections along selected sectors of the latitude circle (c, e) and of the meridian (d, f) intersecting at the lidar location. The panels (c) and (d) depict the stratospheric gravity wave fields in terms of temperature perturbations, potential temperature, and horizontal wind from 14 to 61 km altitude. The temperature perturbations are plotted after applying a horizontal one-dimensional Gaussian filter with $\lambda_{xy,cut} = 900$ km. Both lower panels (e) and (f) display the thermal stability from 3 km to 14 km altitude and allow the localization of the tropopause. Additionally, isentropic lines and zonal and meridional winds are depicted. It must be noted that all four panels exaggerate the height. Panel (c), for example, would be about 120 times longer in the horizontal direction if the aspect ratio were realistic. The vertical dashed lines in panels (c) to (f) refer to the location of the time-height diagram in (a), the virtual lidar location.

The final bottom panel (g) combines a so-called tropopause map (Morgan & Nielsen-Gammon, 1998) with the geopotential height and wind field at 850 hPa. This visualization indicates the position of upper-level troughs and ridges. Furthermore, it displays the direction and strength of the wind in the lower troposphere so that periods with cross-mountain flows and the excitation of mountain waves can be detected. Dashed lines refer to the cross sections in panels (c) to (f). Examining panels (c) through (g) at successive time steps reveals the temporal evolution of the tropospheric and stratospheric flow conditions, the upper-level troughs, and the gravity wave-induced flow response in the middle atmosphere. The synoptic examination of the composite figure may provide an indication of the dynamical processes in the atmosphere associated with possible transient or steady wave sources. For this purpose, the series of identical composite figures for the whole period in panel (a) has been animated[1].

Consistent with Dörnbrack et al. (2022), in the animation of Figure 4, the largest gravity wave amplitudes in the upper stratosphere in panel (c) repeatedly appear above the eastward propagating upper-level trough in panel (e). In the time-height diagram (a), this gravity wave signal appears gradually at lower altitudes before it almost simultaneously appears above 30 km. The timestamp in Figure 4(c) reveals that the waves propagate up and upstream with rather horizontally oriented phase lines in the presence of weaker winds in the lower stratosphere. Above 30 km, the phase lines lean into the stronger winds of the polar night jet, the vertical wavelength increases and the upstream propagation vanishes. In addition, panel 4(d) emphasizes the refraction of these NOGWs southward into the polar night jet.

At this point, we can test the derivation of wave properties in time-height diagrams for gravity waves excited by a propagating source introduced in Section 2b and partly validate it with Figure 4(c). At z $\approx$ 25 and 45 km, we estimate vertical wavelengths $\lambda_z \approx 9$ and 20 km and about 10 and 12 h between two consecutive maxima. Following the procedure in Section 2b, these periods imply horizontal wavelengths λ_x of 500 and 600 km, respectively, which are reasonable approximations compared with phase lines in Panel (c). The corresponding vertical group velocities are 0.49 and 2.1 m s^{-1} and depict a consistent picture with idealized theories that the vertical propagation speed increases in the presence of larger horizontal wind speeds (e.g., Gill, 1982).

4 Gravity waves in Rayleigh lidar observations and ERA5

Since 2018, the Compact Autonomous Rayleigh Lidar (CORAL) of the DLR conducts measurements at the southern tip of South America (53.79°S) in Río Grande, Argentina (B. Kaifler & Kaifler, 2021). Its automated operation provides a unique data set of observations near 60°S. But its proximity to the Andes is no coincidence. It is a very suitable location to study the Earth strongest hot spot of large-amplitude mountain waves in the middle atmosphere (Rapp et al., 2021; Reichert et al., 2021). And, as is often the case, reality is not perfect and the conditions for identifying non-orographic gravity waves are not ideal at this place.

Nevertheless, it may be possible to detect signatures of NOGWs from transient wave sources in these Rayleigh lidar measurements, even though CORAL measurements are dominated by mountain waves in austral winter (N. Kaifler et al., 2020; Reichert et al., 2021). In the following, we present two selected CORAL observations that show similar phase line patterns in the time-height diagrams as the simulated ones in Section 2 or the virtual lidar over the Southern Ocean in Section 3. More specifically, they show upward-tilted phase lines.

4.1 CORAL observations

Figures 5 and 6 show night-time temperature measurements for selected days in June 2018 and August 2020. A background state $\bar{T}$ is computed by calculating the nightly mean temperature and temperature perturbations T' in panels (b) are determined by subtracting $\bar{T}$ from the absolute temperature measurements as shown in panels (a) of Figures 5 and 6, respectively. This approach is similar to the approach used for the ERA5 data as shown in panels (c) of Figures 2, 9, and 10, respectively. In addition, panels (c) of Figures 5 and 6 show T' after applying a vertical Butterworth highpass filter with a cutoff wavelength of $\lambda_{z,cut} = 20\,\text{km}$ (e.g., Ehard et al., 2015) to identify stationary mountain waves. Though multiple studies suggest $\lambda_{z,cut} = 15\,\text{km}$ for mountain waves, we adapt to recent results of Reichert (2022), who discovered that more than 50% of the waves in the analyzed CORAL dataset have vertical wavelengths larger than 16.5 km. Most likely, Reichert's finding is a result of the very strong horizontal winds in the PNJ above Río Grande in austral winter and it is consistent with our analysis in Section 3. In Figure 2(e), the 15 km-Butterworth filter did not resolve the NOGWs above 30 km because their vertical wavelength exceeded 20 km in the upper stratosphere. The increase of λ_z for a vertically increasing PNJ wind was clearly identified in the idealized simulations and is visible by comparing panels (c) and (d) with (e) and (f) of Figure 1.

Such an increase in λ_z is also apparent in the June 2018 measurement period (Figure 5(b) and (c)): After 05:00 UTC, distinct upward-tilted phase lines are observed, and λ_z is between 10 and 12 km in the stratosphere up to about 35 km altitude and between 15-20 km above. The phase lines' angle is approximately 10 km over 5-6 h, so it is in the same range as the angle in the idealized simulation in panel 1(f). The nearly horizontal phase lines observed before 05:00 UTC suggest that these waves are most probably due to mountain waves entering CORAL's field of view. To explore possible reasons for the following ascending phase lines, we associate them with non-steady atmospheric processes. Therefore, a detailed analysis of the synoptic evolution during the event proves essential to enable meaningful physical interpretations in the following section.

The August 2020 case in Figure 6 comprises nightly measurements for two consecutive nights. Unfortunately, these nights were temporarily cloudy at Río Grande, preventing continuous measurements. On the other hand, knowledge of cloud cover could prove promising as these clouds are associated with a passing surface low and an upper-level front and indicate a possible transient wave source. During the first night, Figure 6(b) and (c) show upward-tilted phase lines, which are most pronounced between 40 and 60 km altitude. For the second night, temperature perturbations vary significantly after applying temporal or vertical filtering, but again, subtracting the temporal mean results in distinct upward-tilted phase lines between 30 and 55 km and 22:00 and 07:00 UTC on August 9 in Figure 6(b).

In the following section, we present the composite Figures 7 and 8 based on ERA5 data, which are similar to Figure 4, to support further interpretations of the CORAL measurements. Phase lines in both time-height diagrams (a) of Figures 7 and 8 agree well with the observations. The waves' phases match the overlaid measurements and the phase lines also tilt upward for the measurement periods. This initial visual inspection strongly suggests that the atmospheric processes causing the upward slope in these CORAL measurements are represented in ERA5 and are adequately covered by the dynamics of the underlying IFS model. A closer look at each case and its animated ERA5 composition[1] may be instructive.

[1] `https://doi.org/10.5281/zenodo.8319370`

4.2 ERA5 overview for June 2018 measurements

First, we determine whether the upward-tilted phase lines in Figures 5(b) and (c) and Figure 7(a) are related to the gravity wave excitation near a propagating upper-level trough. Stratospheric temperature perturbations, as shown in panel 5(c), are tilted upstream into the dominant zonal wind, reaching more than $165\,\mathrm{m\,s^{-1}}$, see panel 7(d). This finding clearly illustrates that most of the stratospheric gravity wave activity is confined to the PNJ. In panel 7(c), other coherent gravity wave patterns can be identified west of 100°W and east of the CORAL site. At the time shown in Figure 7, the vertical section in panel (e) shows an upper-level trough west 100°W and near 60°W, in between, a ridge enhances the tropopause height to about 12.5 km. The upper-level trough at 60°W already passed CORAL's location 24 hours earlier, as seen in the preceding time steps[1]. The altitude of the dynamical tropopause, as shown by the blueish colors northeast of CORAL in Figure 7(g), indicates that the upper-level trough is located east of Río Grande.

Signatures of upward-tilted phase lines in the time-height diagram 7(a) in the ERA5 data and in the measurements occur well after the passage of the upper-level trough. Therefore, assuming that gravity wave-induced perturbations occur directly over the upper level trough, it appears that in this case the upward-tilted phase lines are not caused by NOGWs over an upper-level trough. Can alternative atmospheric processes be identified in the ERA5 data that led to the tilted phase lines?

During the period of the CORAL observations, the upper-level ridge (as marked by the dark red area in panel (g) of Figure 7) approaches the lidar station from the west. The associated tropospheric flow turns from southerly winds at 850 hPa to southwesterly and westerly winds, which can be observed in Figure 7(g) over several time steps. As a result, the wind component perpendicular to the mountain range becomes stronger, leading to a temporary increase in the winds at mountain crests. Subsequently, the forcing winds remain almost the same, causing a nearly steady regime that favors the excitation of mountain waves on the southernmost mountain range of the Andes, the Cordillera Darwin. The time-height diagrams in Figure 9(e) and (g) related to Figure 7 support this interpretation. The upward-tilted phase lines of the ERA5 data turn into horizontal phase lines that persist for nearly 12 h after the CORAL measurement period. The ERA5 data, therefore, give a clear indication of stationary mountain waves. In addition, phase lines at the bottom edge (≈ 15 km) of panels 7(c) and (d) also indicate an excitation of mountain waves southwest of CORAL's location. This deduction becomes clearer by comparing the phase lines, particularly their location, for different timestamps[1].

A similar explanation can be found for the descending phase lines in the first 12-15 hours of Figure 7(a): The wind at the mountain tops decreases due to the departure of the low-pressure system and the associated low-level wind change to southerlies. The descending phase lines are only briefly interrupted between 15 UTC and 21 UTC on June 22, 2018, before the excitation of mountain waves intensifies, as discussed above. All in all, these virtual observations in the ERA5 data provide a conclusive picture and suggest that the upward tilt of phase lines in the June 2018 CORAL measurements (Figure 5(b) and (c)) was caused by transient wind forcing that resulted in non-stationary mountain waves. Properties of transient mountain waves under unsteady large-scale forcing have been discussed previously (e.g., Chen et al., 2005, 2007; Portele et al., 2018).

4.3 ERA5 overview for August 2020 measurements: first night

As with the June 2018 CORAL observations, we first check for the presence of an upper-level trough during the August 2020 period in panels (e) and (g) of Figure 8. Visualized is a point in time during the first measurement night, as indicated by the black vertical line in panel 8(a). The funnel-like shape of the PVU contour lines in panel (e) and the green-blue colors in panel (g) of Figure 8 indeed show the existence of a textbook upper-level trough upstream of CORAL at 85°W. The timing of the passage of the upper-level trough does not match the first measurement period with upward-tilted phase lines, but the animation[1] reveals that it could fit with CORAL observations during the second night from August 8 to 9. Upward-tilted phase lines are also apparent in ERA5 above 25 km during this second measurement period (Figure 8(a)). The pattern is not as distinct as in Figure 4, but at CORAL's location, it could be related to a superposition of mountain waves impeding explicit conclusions. Section 4d will focus on this second measurement period and examine whether it is possible to associate the corresponding phase line pattern with NOGWs. Within this section, we focus on analyzing the first measurement night. Could a transient wind forcing again explain the phase lines' upward tilt?

As depicted in the meridional section of Figure 8(d), the PNJ is centered directly above CORAL. Considering the horizontal refraction of gravity waves into the jet, as discussed for example by Sato et al. (2012), phase lines at higher altitudes as depicted in the extended time-height diagram in panel 8(a) could indeed belong to mountain waves excited by the cross-mountain flow further north or south. Actually, the southward tilt of the phase lines in panel 8(d) suggests that waves observed by CORAL above 40 km altitude originate farther north at latitudes around 40° to 50°S. At these latitudes, the Andes run almost exactly north-south and are a reliable source of mountain waves. In fact, the direction of the wind changes from a westerly to a northwesterly flow and the strength of the prevailing wind blowing over the Andes in this area increases before and during the observation period. However, the conditions are not as unambiguous as in the first case of June 2018. Wind speed and direction at lower levels still change afterwards, and another feature in the ERA5 data should be noted.

Meridional winds in Figure 8(c) show a wind turning from a westerly towards a more southwesterly flow between 40 and 60 km altitude and between 35° to 50°W. This change in the meridional wind component indicates a meandering of the PNJ that passed CORAL at around 19:00 UTC, just three hours before the lidar started its measurements. Observing the phase lines in Figure 8(c) for several successive timestamps, a shortening of the vertical wavelengths is noticeable, which appears to follow the meandering of the PNJ. These changes in stratospheric propagation conditions occur at the same times when the upward-sloping phase lines in 8(a) appear. The vertical wavelengths decrease toward the end of the upward tilt before increasing again.

In conclusion, the interpretation of the ERA5 data is not as clear for the August 2020 CORAL measurements. NOGWs excited above a propagating upper-level trough can be most likely ruled out as the source for the upward-tilted phase lines. The analysis so far seems to indicate that the propagation conditions have changed during the observations. This is not surprising, since the waves certainly also deposit momentum and reduce the strength of the PNJ: Panel (d) of Figure 8 shows very impressively a local deceleration of the PNJ at about 50 km altitude at the position of CORAL. In addition, the transient low-level winds altered the forcing conditions for mountain waves, making it difficult to make a definite statement about the ascending phase lines in Figure 8(a).

4.4 ERA5 overview for August 2020 measurements: second night

The dotted rectangle in panels (c) and (e) of Figure 8 frames gravity waves in the stratosphere above a westward propagating upper-level trough. These NOGWs are already visible in the lower stratosphere, and their phase line pattern is very similar to the ERA5 analysis of NOGWs over the Southern Ocean in Figure 4 and Figure 17 in Dörnbrack et al. (2022). The local coincidence of the NOGWs in the stratosphere and the underlying upper-level trough at successive times is even more evident in the time sequence of Figure 8[1]: It reveals that and how these stratospheric gravity waves propagate eastward in concert with the upper-level trough. The phase lines shape and the nearly uniform propagation of these waves in ERA5 again resemble the results of the idealized numerical simulations presented in Section 2. In addition to the case of Dörnbrack et al. (2022) in Section 3, this finding represents another example of NOGWs over a propagating upper-level trough that mimics the pattern of mountain waves. This supports the hypothesis that an upper-level trough, particularly the undulated isentropes near and above the tropopause, could be a wave-generating internal boundary to the stratospheric flow aloft, just as mountains at the surface are to the tropospheric flow. The difference lies in the fact that the undulated isentropes are part of the atmospheric flow and change width and depth depending on the stage of the baroclinic life cycle.

In this second example, the upper-level trough propagates over the Pacific Ocean, and its vicinity to the southern tip of South America allows a direct comparison of these NOGWs to mountain waves over the Andes in Figure 8(c). The maximum amplitudes of the NOGWs are ≈ 3 K between 40 and 45 km altitude and are much lower than the amplitudes of the mountain waves at the same altitude, latitude, and time over the Andes, which are ≈ 12 K. This finding is consistent with a recent climatological analysis using AIRS satellite observations that reveals significantly smaller momentum fluxes for NOGWs over the ocean (Hindley et al., 2020). Also, Hendricks et al. (2014) concluded that the wave amplitudes are much weaker across the mid-latitude Pacific Ocean.

The preceding results of this section 4 have shown that these eastward propagating NOGWs indeed lead to upward sloping phase lines in time-height diagrams as anticipated from the idealized simulations (Figure 1). However, detecting these NOGWs in ground-based Rayleigh lidar measurements becomes complicated at locations where mountain waves dominate and superimpose other wave signals, as in the case of CORAL. The upper-level trough framed by the dotted rectangle in Figure 8(e) passes CORAL's location between 17:00 and 21:00 UTC on August 8, just before the lidar started measuring around 22:00 UTC. The corresponding gravity waves in the stratosphere in Panel (c) appear slightly upstream of the trough at multiple timestamps[1], so CORAL's measurements exactly match the passage of these NOGWs.

As previously stated, the wave signals in the ERA5 data and measurements fit qualitatively, but measured amplitudes are generally a factor 2 higher. Phase lines in the time-height diagram in Figure 8(a) tilt upward during the whole measurement period from 22:00 UTC to 09:00 UTC on August 9, but the pattern is less distinct compared to the event over the Southern Ocean in Figure 4(a). With some imagination, phase lines are less steep and vertical wavelengths smaller below 30 km which would be consistent with the Southern Ocean case. At the same time, the animation of Figure 8[1], particularly panels (c) and (d), illustrate that mountain waves excited by the Andes Mountains are regularly affecting CORAL's field of view. Panels (e) and (g) in Figure 10 complement this interpretation, and horizontal phase lines above 30 km suggest the presence of stationary mountain waves during the second CORAL measurement. In this period, the Butterworth filter is reliable because the vertical background temperature profile in Figure 8(b) or the right column in Figure 10 does not contain any small-scale oscillations in the upper stratosphere.

In both, the animation[1] and Figure 10, these stationary mountain waves are less pronounced at the beginning of the measurements between 21:00 and 01:00 UTC but amplitudes increase again after 01:00 UTC. Such transient processes also influence the temperature perturbations in time-height diagrams after applying a temporal filter in Figure 4(a) or 10(b) and complicate the identification of NOGWs in Rayleigh lidar measurements. Combined with the fact that NOGWs have relatively smaller amplitudes, an identification seems only feasible when measurements overlap with the passage of an upper-level trough during a period with negligible mountain wave forcing. Or, put another way, a lidar location far from significant orographic gravity wave sources would simplify the investigation of NOGWs.

5 Summary and Conclusions

This article addresses how NOGWs excited by propagating upper-level troughs can be identified in time-height diagrams of ground-based Rayleigh lidar observations. Idealized numerical simulations were first presented to show the difference between stratospheric temperature perturbations in simulated lidar signals resulting from stationary and transient wave sources. Upward-tilted phase lines are the main characteristics of simulated lidar signals for the case when the wave source moves in the direction of the mean wind. The angle of the tilt depends on the source's propagation speed and the gravity wave's horizontal wavelength. If the source moves in the opposite direction to the wind, the phase lines decrease in height with progressing time, a case not shown and discussed here. In the time-height diagrams, the sloping phase lines differ notably from the horizontal phase lines typically found for stationary mountain waves. Thus, sloping phase lines in ground-based lidar data can potentially be associated with transient wave sources. It must be noted, however, that other atmospheric processes, such as increasing or decreasing winds, i.e. transient propagation conditions, also lead to tilted phase lines.

Therefore, it is very helpful and actually just necessary to relate the observed time-height diagram to meteorological variables from available high-resolution NWP models and their temporal evolution in the vicinity of the lidar site. To this end, we have proposed a composite figure that combines the temporal evolution in a time-height diagram with spatial illustrations in vertical and horizontal sections. This composite figure is produced for all available times provided by the respective meteorological analyses or forecasts. Animations of the composite figure help to identify transient and steady modes of gravity waves as well as propagating upper-level troughs. Here, the most recent ECMWF reanalyses ERA5 data (Hersbach et al., 2020) are used as they partially resolve atmospheric gravity waves (e.g., Gupta et al., 2021; Pahlavan et al., 2023). The ERA5 data only give an indication of gravity waves produced by primary sources such as flows over mountains, frontal systems aloft, convection, etc. Due to numerical vorticity and divergence damping of motion fields above 10 hPa, most vertically propagating gravity wave modes are attenuated, and the generation of secondary waves cannot be represented by IFS (Polichtchouk et al., 2023, Sec. 2).

Subsequent to the idealized simulations, the composite figure was introduced by means of NOGWs above an upper-level trough over the Southern Ocean, which were already discussed by Dörnbrack et al. (2022). Here, the composite plots were produced for a virtual lidar location far away from any orography and the ERA5 data was used to emulate the measurements of a vertically starring ground-based lidar. As predicted by the idealized simulations, a distinct pattern of upward-tilted phase lines dominated the time-height diagram during the passage of the upper-level trough and corresponding NOGWs in the stratosphere. The proposed procedure was confirmed and it could also be clarified that a temporal filtering is advantageous for the identification of these NOGWs, particularly in the presence of a strong PNJ and large vertical wavelengths which limit the application of a vertical Butterworth filter.

In a final step, it was the goal to identify NOGWs in actual ground-based Rayleigh lidar measurements. The analysis of two selected periods with CORAL observations revealed the full complexity of the real atmospheric flow at the lidar site in Argentine Patagonia in the lee of the Andes. For two out of the three measurement nights, the composite figures revealed that propagating upper-level troughs did not cause the upward-tilted phase lines in the CORAL measurements. Inspection of the vertical and horizontal sections for successive times, however, suggested that mountain waves interacted with transient background wind conditions. The third measurement exactly matched the passage of an upper-level trough and corresponding NOGWs, but the small-amplitude NOGWs were superimposed by large-amplitude mountain waves and clear identification of gravity waves excited by an upper-level trough was not feasible. In fact, a direct comparison of these NOGWs identified upstream over the Pacific Ocean with mountain waves over the southern Andes revealed that the amplitudes of these NOGWs are about a factor of 4 smaller than the amplitudes of mountain waves.

Nevertheless, the analysis showed that the proposed composite plots are extremely useful for placing the CORAL observations in a meteorological context with relatively little effort. As such, they can be a helpful starting point to develop hypotheses about the origins of the observed waves and their sources before using other, more elaborate methods such as ray tracing or numerical simulations.

In most cases, it will be difficult to effectively isolate NOGWs in Rayleigh lidar measurements at sites commonly dominated by strong mountain waves, such as CORAL in Río Grande, Argentina. A lidar site less influenced by mountain waves, like the virtual lidar location over the Southern Ocean in Section 3, could show whether the discussed signatures can be identified over propagating upper-level troughs and provide further insight into the proposed excitation process. A flat island would be the ideal environment, but options are limited, and islands like South Georgia, the Islas Malvina (Falkland Islands), or Auckland islands are also prone to mountain waves (e.g., Vosper, 2015; Hindley et al., 2021; Mixa et al., 2021).

Appendix A Open Research

The ERA5 reanalysis dataset is publicly available at `https://cds.climate.copernicus.eu` and cited as required.

Animations of figures in this work showing compositions of weather prediction data (ERA5 data) support the discussion and are available at `https://doi.org/10.5281/zenodo.10073388` via 10.5281/zenodo.10073388. Corresponding CORAL measurements are also included and the underlying source code for the ERA5 visualizations is publicly available at `https://github.com/michibinder/eratools`.

Acknowledgments
We gratefully acknowledge the work of Bernd Kaifler and his team who built and operate the COmpact Rayleigh Autonomous Lidar in Río Grande and provide the temperature measurements.

References

Alexander, M. J., Geller, M., McLandress, C., Polavarapu, S., Preusse, P., Sassi, F., ... Watanabe, S. (2010, July). Recent developments in gravity-wave effects in climate models and the global distribution of gravity-wave momentum flux from observations and models: Recent Developments in Gravity-Wave Effects. *Quarterly Journal of the Royal Meteorological Society*, *136*(650), 1103–1124. Retrieved 2021-05-11, from `http://doi.wiley.com/10.1002/qj.637` doi: 10.1002/qj.637

Bacmeister, J., & Schoeberl, M. (1989). Breakdown of Vertically Propagating Two-Dimensional Gravity Waves Forced by Orography. *Journal of the Atmospheric Sciences*, *46*. doi: 10.1175/1520-0469(1989)046⟨2109:BOVPTD⟩2.0.CO;2

Chen, C.-C., Durran, D. R., & Hakim, G. J. (2005). Mountain-Wave Momentum Flux in an Evolving Synoptic-Scale Flow. *Journal of the Atmospheric Sciences*, *62*(9), 3213 - 3231. Retrieved from `https://journals.ametsoc.org/view/journals/atsc/62/9/jas3543.1.xml` doi: https://doi.org/10.1175/JAS3543.1

Chen, C.-C., Hakim, G. J., & Durran, D. R. (2007). Transient Mountain Waves and Their Interaction with Large Scales. *Journal of the Atmospheric Sciences*, *64*(7), 2378 - 2400. Retrieved from `https://journals.ametsoc.org/view/`

journals/atsc/64/7/jas3972.1.xml doi: https://doi.org/10.1175/JAS3972.1

Chu, X., Zhao, J., Lu, X., Harvey, V. L., Jones, R. M., Becker, E., ... Dörnbrack, A. (2018). Lidar Observations of Stratospheric Gravity Waves From 2011 to 2015 at McMurdo (77.84°S, 166.69°E), Antarctica: 2. Potential Energy Densities, Lognormal Distributions, and Seasonal Variations. *Journal of Geophysical Research: Atmospheres*, *123*(15), 7910-7934. Retrieved from https://agupubs.onlinelibrary.wiley.com/doi/abs/10.1029/2017JD027386 doi: https://doi.org/10.1029/2017JD027386

Clark, T. L. (1977). A small-scale dynamic model using a terrain-following coordinate transformation. *Journal of Computational Physics*, *24*(2), 186-215. Retrieved from https://www.sciencedirect.com/science/article/pii/0021999177900572 doi: https://doi.org/10.1016/0021-9991(77)90057-2

Dörnbrack, A., Gisinger, S., Kaifler, N., Portele, T. C., Bramberger, M., Rapp, M., ... Jelić, D. (2018). Gravity waves excited during a minor sudden stratospheric warming. *Atmospheric Chemistry and Physics*, *18*(17), 12915–12931. Retrieved from https://acp.copernicus.org/articles/18/12915/2018/ doi: 10.5194/acp-18-12915-2018

Dörnbrack, A. (2002). Evidence for inertia gravity waves forming polar stratospheric clouds over Scandinavia. *Journal of Geophysical Research*, *107*(D20), 8287. Retrieved 2022-12-09, from http://doi.wiley.com/10.1029/2001JD000452 doi: 10.1029/2001JD000452

Dörnbrack, A., Eckermann, S. D., Williams, B. P., & Haggerty, J. (2022, February). Stratospheric Gravity Waves Excited by a Propagating Rossby Wave Train—A DEEPWAVE Case Study. *Journal of the Atmospheric Sciences*, *79*(2), 567–591. Retrieved 2022-03-20, from https://journals.ametsoc.org/view/journals/atsc/79/2/JAS-D-21-0057.1.xml doi: 10.1175/JAS-D-21-0057.1

Dörnbrack, A., Gisinger, S., & Kaifler, B. (2017, March). On the Interpretation of Gravity Wave Measurements by Ground-Based Lidars. *Atmosphere*, *8*(12), 49. Retrieved 2021-03-08, from http://www.mdpi.com/2073-4433/8/3/49 doi: 10.3390/atmos8030049

Eckermann, S. D., Doyle, J. D., Reinecke, P. A., Reynolds, C. A., Smith, R. B., Fritts, D. C., & Dörnbrack, A. (2019, September). Stratospheric Gravity Wave Products from Satellite Infrared Nadir Radiances in the Planning, Execution, and Validation of Aircraft Measurements during DEEPWAVE. *Journal of Applied Meteorology and Climatology*, *58*(9), 2049–2075. Retrieved 2023-02-12, from https://journals.ametsoc.org/view/journals/apme/58/9/jamc-d-19-0015.1.xml doi: 10.1175/JAMC-D-19-0015.1

Ehard, B., Kaifler, B., Kaifler, N., & Rapp, M. (2015, November). Evaluation of methods for gravity wave extraction from middle-atmospheric lidar temperature measurements. *Atmospheric Measurement Techniques*, *8*(11), 4645–4655. Retrieved 2022-08-27, from https://amt.copernicus.org/articles/8/4645/2015/ doi: 10.5194/amt-8-4645-2015

Ehard, B., Malardel, S., Dörnbrack, A., Kaifler, B., Kaifler, N., & Wedi, N. (2018). Comparing ECMWF high-resolution analyses with lidar temperature measurements in the middle atmosphere. *Quarterly Journal of the Royal Meteorological Society*, *144*(712), 633-640. Retrieved from https://rmets.onlinelibrary.wiley.com/doi/abs/10.1002/qj.3206 doi: https://doi.org/10.1002/qj.3206

Epifanio, C. C., & Durran, D. R. (2001). Three-dimensional effects in high-drag-state flows over long ridges. *Journal of the atmospheric sciences*, *58*(9), 1051–1065. doi: https://doi.org/10.1175/1520-0469(2001)058⟨1051:TDEIHD⟩2.0.CO;2

Ern, M., Trinh, Q. T., Preusse, P., Gille, J. C., Mlynczak, M. G., Russell III, J. M., & Riese, M. (2018, April). GRACILE: a comprehensive climatology of atmospheric gravity wave parameters based on satellite limb soundings. *Earth System Science Data*, *10*(2), 857–892. Retrieved 2022-11-19, from https://essd.copernicus.org/articles/10/857/2018/ doi: 10.5194/essd-10-857-2018

Fritts, D. C., & Alexander, M. J. (2003). Gravity wave dynamics and effects in the middle atmosphere. *Reviews of Geophysics*, *41*(1), 1003. Retrieved 2021-03-22, from http://doi.wiley.com/10.1029/2001RG000106 doi: 10.1029/2001RG000106

Fritts et al. (2016, March). The Deep Propagating Gravity Wave Experiment (DEEPWAVE): An Airborne and Ground-Based Exploration of Gravity Wave Propagation and Effects from Their Sources throughout the Lower and Middle Atmosphere. *Bulletin of the American Meteorological Society*, *97*(3), 425–453. Retrieved 2021-05-14, from https://journals.ametsoc.org/doi/10.1175/BAMS-D-14-00269.1 doi: 10.1175/BAMS-D-14-00269.1

Gettelman, A., Hoor, P., Pan, L. L., Randel, W. J., Hegglin, M. I., & Birner, T. (2011). THE EXTRATROPICAL UPPER TROPOSPHERE AND LOWER STRATOSPHERE. *Reviews of Geophysics*, *49*(3). Retrieved from https://agupubs.onlinelibrary.wiley.com/doi/abs/10.1029/2011RG000355 doi: https://doi.org/10.1029/2011RG000355

Gill, A. E. (1982). *Atmosphere-Ocean Dynamics*. New York: Academic Press.

Gille, J., Barnett, J., Arter, P., Barker, M., Bernath, P., Boone, C., ... Young, G. (2008, June). High Resolution Dynamics Limb Sounder: Experiment overview, recovery, and validation of initial temperature data. *Journal of Geophysical Research*, *113*(D16), D16S43. Retrieved 2023-02-12, from http://doi.wiley.com/10.1029/2007JD008824 doi: 10.1029/2007JD008824

Gisinger, S., Dörnbrack, A., Matthias, V., Doyle, J. D., Eckermann, S. D., Ehard, B., ... Rapp, M. (2017). Atmospheric Conditions during the Deep Propagating Gravity Wave Experiment (DEEPWAVE). *Monthly Weather Review*, *145*(10), 4249 - 4275. Retrieved from https://journals.ametsoc.org/view/journals/mwre/145/10/mwr-d-16-0435.1.xml doi: https://doi.org/10.1175/MWR-D-16-0435.1

Gisinger, S., Polichtchouk, I., Dörnbrack, A., Reichert, R., Kaifler, B., Kaifler, N., ... Sandu, I. (2022). Gravity-Wave-Driven Seasonal Variability of Temperature Differences Between ECMWF IFS and Rayleigh Lidar Measurements in the Lee of the Southern Andes. *Journal of Geophysical Research: Atmospheres*, *127*(13), e2021JD036270. Retrieved from https://agupubs.onlinelibrary.wiley.com/doi/abs/10.1029/2021JD036270 (e2021JD036270 2021JD036270) doi: https://doi.org/10.1029/2021JD036270

Goldberg, M. D., Kilcoyne, H., Cikanek, H., & Mehta, A. (2013, December). Joint Polar Satellite System: The United States next generation civilian polar-orbiting environmental satellite system: USA NEXT GENERATION SATELLITE SYSTEM. *Journal of Geophysical Research: Atmospheres*, *118*(24), 13,463–13,475. Retrieved 2023-02-12, from http://doi.wiley.com/10.1002/2013JD020389 doi: 10.1002/2013JD020389

Gupta, A., Birner, T., Dörnbrack, A., & Polichtchouk, I. (2021). Importance of Gravity Wave Forcing for Springtime Southern Polar Vortex Breakdown as Revealed by ERA5. *Geophysical Research Letters*, *48*(10), e2021GL092762. Retrieved from https://agupubs.onlinelibrary.wiley.com/doi/abs/10.1029/2021GL092762 (e2021GL092762 2021GL092762) doi: https://doi.org/10.1029/2021GL092762

Harvey, V. L., & Knox, J. A. (2019). Beware of inertial instability masquerading as gravity waves in stratospheric temperature perturbations. *Geophysical Research Letters*, *46*(3), 1740-1745. Retrieved from https://agupubs.onlinelibrary.wiley.com/doi/abs/10.1029/2018GL081142 doi: https://doi.org/10.1029/2018GL081142

Hendricks, E. A., Doyle, J. D., Eckermann, S. D., Jiang, Q., & Reinecke, P. A. (2014, May). What Is the Source of the Stratospheric Gravity Wave Belt in Austral Winter? *Journal of the Atmospheric Sciences*, *71*(5), 1583–1592. Retrieved 2021-07-05, from `https://journals.ametsoc.org/doi/10.1175/JAS-D-13-0332.1` doi: 10.1175/JAS-D-13-0332.1

Hersbach et al. (2020, July). The ERA5 global reanalysis. *Quarterly Journal of the Royal Meteorological Society*, *146*(730), 1999–2049. Retrieved 2023-02-10, from `https://onlinelibrary.wiley.com/doi/10.1002/qj.3803` doi: 10.1002/qj.3803

Hindley, N. P., Wright, C. J., Gadian, A. M., Hoffmann, L., Hughes, J. K., Jackson, D. R., ... Ross, A. N. (2021). Stratospheric gravity waves over the mountainous island of South Georgia: testing a high-resolution dynamical model with 3-D satellite observations and radiosondes. *Atmospheric Chemistry and Physics*, *21*(10), 7695–7722. Retrieved from `https://acp.copernicus.org/articles/21/7695/2021/` doi: 10.5194/acp-21-7695-2021

Hindley, N. P., Wright, C. J., Hoffmann, L., Moffat-Griffin, T., & Mitchell, N. J. (2020, November). An 18-Year Climatology of Directional Stratospheric Gravity Wave Momentum Flux From 3-D Satellite Observations. *Geophysical Research Letters*, *47*(22). Retrieved 2020-12-15, from `https://onlinelibrary.wiley.com/doi/10.1029/2020GL089557` doi: 10.1029/2020GL089557

Hindley, N. P., Wright, C. J., Smith, N. D., Hoffmann, L., Holt, L. A., Alexander, M. J., ... Mitchell, N. J. (2019, December). Gravity waves in the winter stratosphere over the Southern Ocean: high-resolution satellite observations and 3-D spectral analysis. *Atmospheric Chemistry and Physics*, *19*(24), 15377–15414. Retrieved 2021-05-13, from `https://acp.copernicus.org/articles/19/15377/2019/` doi: 10.5194/acp-19-15377-2019

Hoffmann, L., & Alexander, M. J. (2009). Retrieval of stratospheric temperatures from Atmospheric Infrared Sounder radiance measurements for gravity wave studies. *Journal of Geophysical Research: Atmospheres*, *114*(D7). Retrieved from `https://agupubs.onlinelibrary.wiley.com/doi/abs/10.1029/2008JD011241` doi: https://doi.org/10.1029/2008JD011241

Hoffmann, L., Xue, X., & Alexander, M. J. (2013). A global view of stratospheric gravity wave hotspots located with Atmospheric Infrared Sounder observations. *Journal of Geophysical Research: Atmospheres*, *118*(2), 416-434. Retrieved from `https://agupubs.onlinelibrary.wiley.com/doi/abs/10.1029/2012JD018658` doi: https://doi.org/10.1029/2012JD018658

Kaifler, B., & Kaifler, N. (2021, March). A Compact Rayleigh Autonomous Lidar (CORAL) for the middle atmosphere. *Atmospheric Measurement Techniques*, *14*(2), 1715–1732. Retrieved 2021-05-18, from `https://amt.copernicus.org/articles/14/1715/2021/` doi: 10.5194/amt-14-1715-2021

Kaifler, B., Lübken, F.-J., Höffner, J., Morris, R. J., & Viehl, T. P. (2015). Lidar observations of gravity wave activity in the middle atmosphere over Davis (69°S, 78°E), Antarctica. *Journal of Geophysical Research: Atmospheres*, *120*(10), 4506-4521. Retrieved from `https://agupubs.onlinelibrary.wiley.com/doi/abs/10.1002/2014JD022879` doi: https://doi.org/10.1002/2014JD022879

Kaifler, N., Kaifler, B., Dörnbrack, A., Rapp, M., Hormaechea, J. L., & de la Torre, A. (2020, December). Lidar observations of large-amplitude mountain waves in the stratosphere above Tierra del Fuego, Argentina. *Scientific Reports*, *10*(1), 14529. Retrieved 2020-09-30, from `http://www.nature.com/articles/s41598-020-71443-7` doi: 10.1038/s41598-020-71443-7

Kühnlein, C., Smolarkiewicz, P. K., & Dörnbrack, A. (2012, April). Modelling atmospheric flows with adaptive moving meshes. *Journal of Computational Physics*, *231*(7), 2741–2763. Retrieved 2021-03-29, from https://linkinghub.elsevier.com/retrieve/pii/S0021999111007224 doi: 10.1016/j.jcp.2011.12.012

Lane, T. P., Reeder, M. J., & Clark, T. L. (2001). Numerical Modeling of Gravity Wave Generation by Deep Tropical Convection. *Journal of the Atmospheric Sciences*, *58*(10), 1249 - 1274. Retrieved from https://journals.ametsoc.org/view/journals/atsc/58/10/1520-0469_2001_058_1249_nmogwg_2.0.co_2.xml doi: https://doi.org/10.1175/1520-0469(2001)058⟨1249:NMOGWG⟩2.0.CO;2

Le Pichon, A., Assink, J. D., Heinrich, P., Blanc, E., Charlton-Perez, A., Lee, C. F., ... Claud, C. (2015). Comparison of co-located independent ground-based middle atmospheric wind and temperature measurements with numerical weather prediction models. *Journal of Geophysical Research: Atmospheres*, *120*(16), 8318-8331. Retrieved from https://agupubs.onlinelibrary.wiley.com/doi/abs/10.1002/2015JD023273 doi: https://doi.org/10.1002/2015JD023273

Lipps, F. B., & Hemler, R. S. (1982). A Scale Analysis of Deep Moist Convection and Some Related Numerical Calculations. *Journal of the Atmospheric Sciences*, *39*, 2192–2210.

Metz, J. J., & Durran, D. R. (2021, May). Are finite-amplitude effects important in non-breaking mountain waves? *Quarterly Journal of the Royal Meteorological Society*, qj.4045. Retrieved 2021-07-07, from https://onlinelibrary.wiley.com/doi/10.1002/qj.4045 doi: 10.1002/qj.4045

Mixa, T., Dörnbrack, A., & Rapp, M. (2021, May). Nonlinear Simulations of Gravity Wave Tunneling and Breaking over Auckland Island. *Journal of the Atmospheric Sciences*, *78*(5), 1567–1582. Retrieved 2022-12-04, from https://journals.ametsoc.org/view/journals/atsc/78/5/JAS-D-20-0230.1.xml doi: 10.1175/JAS-D-20-0230.1

Mlynczak, M. G. (1997, January). Energetics of the mesosphere and lower thermosphere and the SABER experiment. *Advances in Space Research*, *20*(6), 1177–1183. Retrieved 2023-02-12, from https://linkinghub.elsevier.com/retrieve/pii/S0273117797007692 doi: 10.1016/S0273-1177(97)00769-2

Morgan, M. C., & Nielsen-Gammon, J. W. (1998). Using tropopause maps to diagnose midlatitude weather systems. *Monthly Weather Review*, *126*(10), 2555 - 2579. Retrieved from https://journals.ametsoc.org/view/journals/mwre/126/10/1520-0493_1998_126_2555_utmtdm_2.0.co_2.xml doi: https://doi.org/10.1175/1520-0493(1998)126⟨2555:UTMTDM⟩2.0.CO;2

Pahlavan, H. A., Wallace, J. M., & Fu, Q. (2023). Characteristics of Tropical Convective Gravity Waves Resolved by ERA5 Reanalysis. *Journal of the Atmospheric Sciences*, *80*(3), 777 - 795. Retrieved from https://journals.ametsoc.org/view/journals/atsc/80/3/JAS-D-22-0057.1.xml doi: https://doi.org/10.1175/JAS-D-22-0057.1

Pfister, L., Chan, K. R., Bui, T. P., Bowen, S., Legg, M., Gary, B., ... Starr, W. (1993, May). Gravity waves generated by a tropical cyclone during the STEP tropical field program: A case study. *Journal of Geophysical Research: Atmospheres*, *98*(D5), 8611–8638. Retrieved 2021-06-22, from http://doi.wiley.com/10.1029/92JD01679 doi: 10.1029/92JD01679

Plougonven, R., & Zhang, F. (2014, March). Internal gravity waves from atmospheric jets and fronts. *Reviews of Geophysics*, *52*(1), 33–76. Retrieved 2021-03-23, from http://doi.wiley.com/10.1002/2012RG000419 doi: 10.1002/2012RG000419

Polichtchouk, I., van Niekerk, A., & Wedi, N. (2023). Resolved gravity waves in the extratropical stratosphere: Effect of horizontal resolution increase from o(10) to o(1) km. *Journal of the Atmospheric Sciences*, *80*(2), 473 - 486. Retrieved from https://journals.ametsoc.org/view/journals/atsc/80/2/JAS-D-22-0138.1.xml doi: https://doi.org/10.1175/JAS-D-22-0138.1

Portele, T. C., Dörnbrack, A., Wagner, J. S., Gisinger, S., Ehard, B., Pautet, P.-D., & Rapp, M. (2018). Mountain-Wave Propagation under Transient Tropospheric Forcing: A DEEPWAVE Case Study. *Monthly Weather Review*, *146*(6), 1861 - 1888. Retrieved from `https://journals.ametsoc.org/view/journals/mwre/146/6/mwr-d-17-0080.1.xml` doi: https://doi.org/10.1175/MWR-D-17-0080.1

Preusse, P., Dörnbrack, A., Eckermann, S. D., Riese, M., Schaeler, B., Bacmeister, J. T., ... Grossmann, K. U. (2002, December). Space-based measurements of stratospheric mountain waves by CRISTA 1. Sensitivity, analysis method, and a case study: STRATOSPHERIC MOUNTAIN WAVE MEASUREMENTS BY CRISTA, 1. *Journal of Geophysical Research: Atmospheres*, *107*(D23), CRI 6–1–CRI 6–23. Retrieved 2021-03-22, from `http://doi.wiley.com/10.1029/2001JD000699` doi: 10.1029/2001JD000699

Prusa, J. M., Smolarkiewicz, P., & Garcia, R. (1996, September). Propagation and Breaking at High Altitudes of Gravity Waves Excited by Tropospheric Forcing. *Journal of the Atmospheric Sciences*, *53*. doi: 10.1175/1520-0469(1996)053⟨2186:PABAHA⟩2.0.CO;2

Prusa, J. M., & Smolarkiewicz, P. K. (2003, September). An all-scale anelastic model for geophysical flows: dynamic grid deformation. *Journal of Computational Physics*, *190*(2), 601–622. Retrieved 2021-03-21, from `https://linkinghub.elsevier.com/retrieve/pii/S0021999103002997` doi: 10.1016/S0021-9991(03)00299-7

Prusa, J. M., Smolarkiewicz, P. K., & Wyszogrodzki, A. A. (2008, October). EULAG, a computational model for multiscale flows. *Computers & Fluids*, *37*(9), 1193–1207. Retrieved 2020-12-15, from `https://linkinghub.elsevier.com/retrieve/pii/S004579300700206X` doi: 10.1016/j.compfluid.2007.12.001

Rapp, M., Dörnbrack, A., & Preusse, P. (2018). Large midlatitude stratospheric temperature variability caused by inertial instability: A potential source of bias for gravity wave climatologies. *Geophysical Research Letters*, *45*(19), 10,682-10,690. Retrieved from `https://agupubs.onlinelibrary.wiley.com/doi/abs/10.1029/2018GL079142` doi: https://doi.org/10.1029/2018GL079142

Rapp et al. (2021, April). SOUTHTRAC-GW: An Airborne Field Campaign to Explore Gravity Wave Dynamics at the World's Strongest Hotspot. *Bulletin of the American Meteorological Society*, *102*(4), E871–E893. Retrieved 2021-05-03, from `https://journals.ametsoc.org/view/journals/bams/102/4/BAMS-D-20-0034.1.xml` doi: 10.1175/BAMS-D-20-0034.1

Reichert, R. (2022). *Characterization of gravity waves in the lee of the southern Andes utilizing an autonomous Rayleigh lidar system* (Doctoral dissertation, Ludwig-Maximilians-Universität München). Retrieved 2022-11-10, from `https://edoc.ub.uni-muenchen.de/id/eprint/30211`

Reichert, R., Kaifler, B., Kaifler, N., Dörnbrack, A., Rapp, M., & Hormaechea, J. L. (2021, November). High-Cadence Lidar Observations of Middle Atmospheric Temperature and Gravity Waves at the Southern Andes Hot Spot. *Journal of Geophysical Research: Atmospheres*, *126*(22). Retrieved 2022-08-28, from `https://onlinelibrary.wiley.com/doi/10.1029/2021JD034683` doi: 10.1029/2021JD034683

Sato, K., Tateno, S., Watanabe, S., & Kawatani, Y. (2012, April). Gravity Wave Characteristics in the Southern Hemisphere Revealed by a High-Resolution Middle-Atmosphere General Circulation Model. *Journal of the Atmospheric Sciences*, *69*(4), 1378–1396. Retrieved 2021-03-21, from `https://journals.ametsoc.org/doi/10.1175/JAS-D-11-0101.1` doi: 10.1175/JAS-D-11-0101.1

Schoeberl, M. R. (1985). The Penetration of Mountain Waves into the Middle Atmosphere. *Journal of Atmospheric Sciences*, *42*(24), 2856 - 2864. Retrieved from https://journals.ametsoc.org/view/journals/atsc/42/24/1520-0469_1985_042_2856_tpomwi_2_0_co_2.xml doi: https://doi.org/10.1175/1520-0469(1985)042⟨2856:TPOMWI⟩2.0.CO;2

Smolarkiewicz, P., & Margolin, L. (1993). On Forward-in-Time Differencing for Fluids: Extension to a Curvilinear Framework. *Mon. Weather Rev.*, *121*, 1847–1859. doi: 10.1175/1520-0493(1993)121⟨1847:OFITDF⟩2.0.CO;2

Smolarkiewicz, P. K., & Margolin, L. G. (1997, January). On Forward-in-Time Differencing for Fluids: an Eulerian/Semi-Lagrangian Non-Hydrostatic Model for Stratified Flows. *Atmosphere-Ocean*, *35*(sup1), 127–152. Retrieved 2020-12-15, from http://www.tandfonline.com/doi/abs/10.1080/07055900.1997.9687345 doi: 10.1080/07055900.1997.9687345

Smolarkiewicz, P. K., & Margolin, L. G. (1998, March). MPDATA: A Finite-Difference Solver for Geophysical Flows. *Journal of Computational Physics*, *140*(2), 459–480. Retrieved 2020-12-15, from https://linkinghub.elsevier.com/retrieve/pii/S0021999198959010 doi: 10.1006/jcph.1998.5901

Strelnikova, I., Almowafy, M., Baumgarten, G., Baumgarten, K., Ern, M., Gerding, M., & Lübken, F.-J. (2021). Seasonal Cycle of Gravity Wave Potential Energy Densities from Lidar and Satellite Observations at 54° and 69°N. *Journal of the Atmospheric Sciences*, *78*(4), 1359 - 1386. Retrieved from https://journals.ametsoc.org/view/journals/atsc/78/4/JAS-D-20-0247.1.xml doi: https://doi.org/10.1175/JAS-D-20-0247.1

Vadas, S. L., Fritts, D. C., & Alexander, M. J. (2003, January). Mechanism for the Generation of Secondary Waves in Wave Breaking Regions. *Journal of the Atmospheric Sciences*, *60*(1), 194–214. Retrieved 2022-04-09, from http://journals.ametsoc.org/doi/10.1175/1520-0469(2003)060<0194:MFTGOS>2.0.CO;2 doi: 10.1175/1520-0469(2003)060⟨0194:MFTGOS⟩2.0.CO;2

Vosper, S. B. (2015). Mountain waves and wakes generated by South Georgia: implications for drag parametrization. *Quarterly Journal of the Royal Meteorological Society*, *141*(692), 2813-2827. Retrieved from https://rmets.onlinelibrary.wiley.com/doi/abs/10.1002/qj.2566 doi: https://doi.org/10.1002/qj.2566

Wedi, N. P., & Smolarkiewicz, P. K. (2004). Extending Gal-Chen and Somerville terrain-following coordinate transformation on time-dependent curvilinear boundaries. *Journal of Computational Physics*, *193*(1), 1-20. Retrieved from https://www.sciencedirect.com/science/article/pii/S0021999103003942 doi: https://doi.org/10.1016/j.jcp.2003.07.034

Wright, C. J., Hindley, N. P., Alexander, M. J., Barlow, M., Hoffmann, L., Mitchell, C. N., . . . Yue, J. (2022). Surface-to-space atmospheric waves from Hunga Tonga–Hunga Ha'apai eruption. *Nature*, *609*, 741–746. doi: https://doi.org/10.1038/s41586-022-05012-5

Yamashita, C., Chu, X., Liu, H.-L., Espy, P. J., Nott, G. J., & Huang, W. (2009). Stratospheric gravity wave characteristics and seasonal variations observed by lidar at the South Pole and Rothera, Antarctica. *Journal of Geophysical Research: Atmospheres*, *114*(D12). Retrieved from https://agupubs.onlinelibrary.wiley.com/doi/abs/10.1029/2008JD011472 doi: https://doi.org/10.1029/2008JD011472

Zhao, J., Chu, X., Chen, C., Lu, X., Fong, W., Yu, Z., . . . Dörnbrack, A. (2017). Lidar observations of stratospheric gravity waves from 2011 to 2015 at McMurdo (77.84°S, 166.69°E), Antarctica: 1. Vertical wavelengths, periods, and frequency and vertical wave number spectra. *Journal of Geophysical Research: Atmospheres*, *122*(10), 5041-5062. Retrieved from https://agupubs.onlinelibrary.wiley.com/doi/abs/10.1002/2016JD026368 doi: https://doi.org/10.1002/2016JD026368

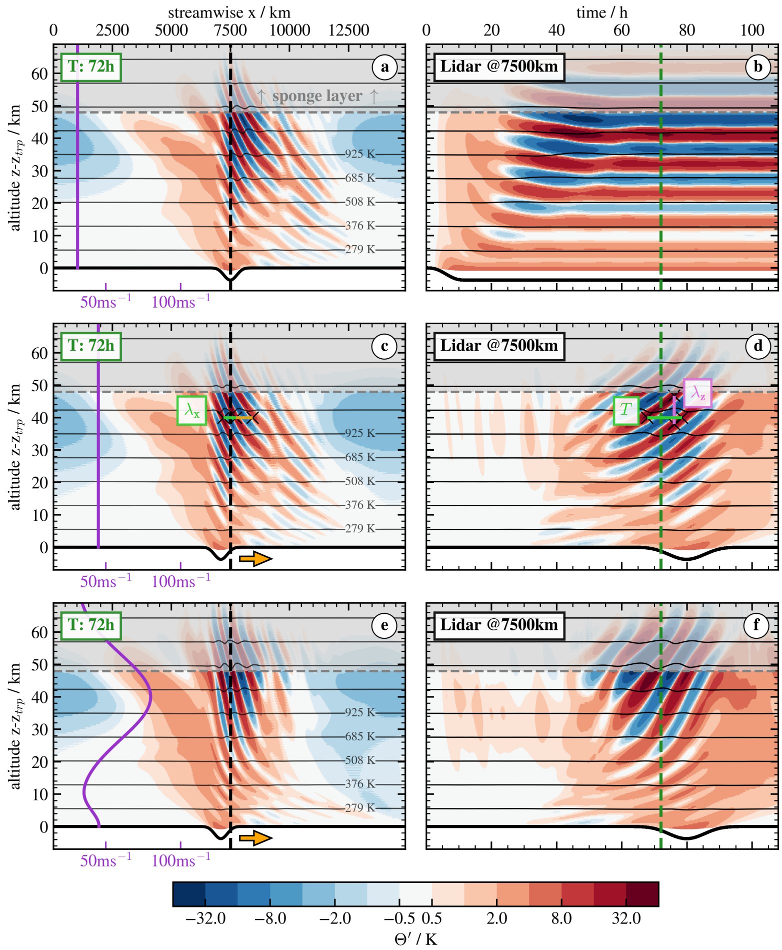

Figure 1. Vertical cross-sections (a, c, e) after $t = 72\,\mathrm{h}$ with ambient wind profiles in purple and time-height diagrams (b, d, f) at the outlined position for three different simulations. The first simulation (a, b) features a stationary obstacle at the lower boundary and a constant wind profile. In the second simulation (c, d) the trough moves to the right with a constant speed $c_{tf} = 13.88\,\mathrm{m\,s^{-1}}$ and the wind is increased by the same amount. The last simulation (e, f) represents a simulation with a more realistic stratospheric wintertime wind profile. The assessment of λ_z and period T from the time-height diagram is labeled in (d), two consecutive λ_x are labeled in (c). Contour lines represent constant potential temperature and the amplitude of the lower boundary is scaled by a factor of 5.

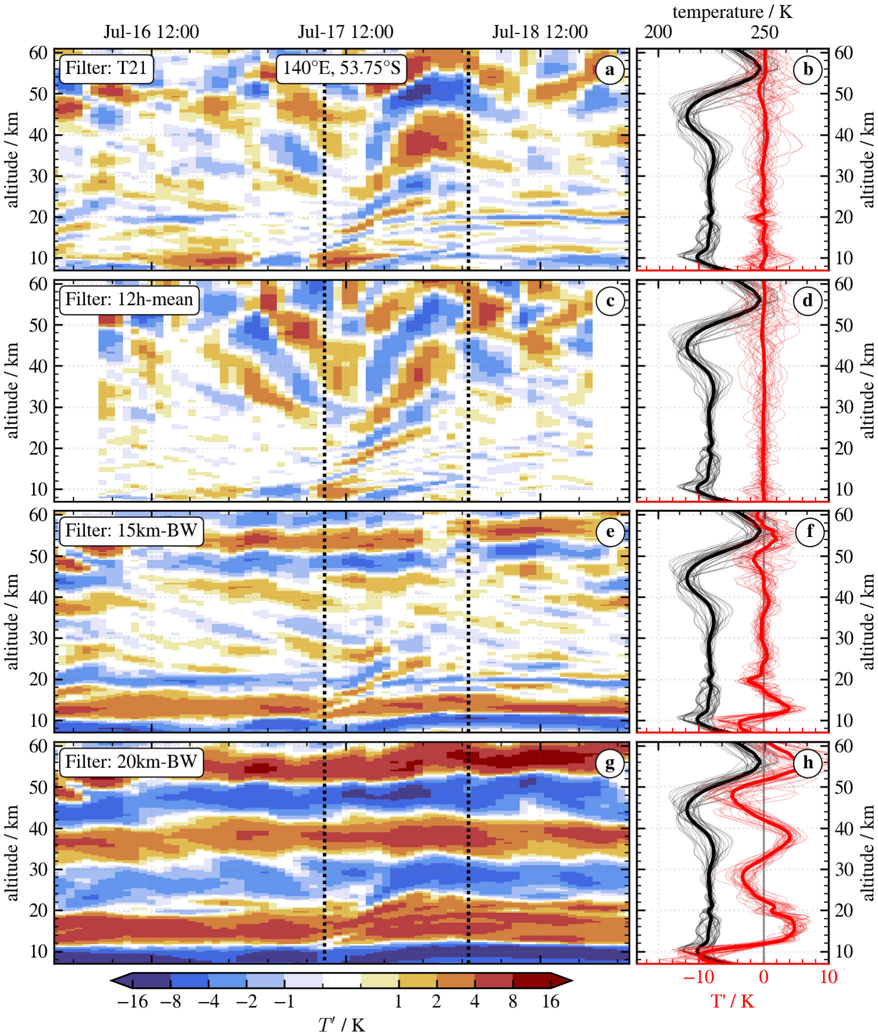

Figure 2. Time-height diagrams of stratospheric ERA5 T' for a location (140°E, 53.75°S) over the Southern Ocean (left column) and corresponding vertical profiles of absolute temperature and temperature perturbations (right column). Thick black and red lines in (b),(d),(f) and (h) are temporal mean profiles of absolute temperature and T', respectively. Thin lines are individual profiles every 2 h. Panels (a) and (b) show temperature perturbations after subtracting the truncated temperature field T21 (horizontally filtered by removing wave numbers larger than 21) of the ERA5 dataset. (c) and (d) show T' after removing a temporal running mean of 12 h. (e) and (f) display the result of a vertical highpass Butterworth filter with a cutoff wavelength $\lambda_{cut} = 15$ km and panels (g) and (h) with $\lambda_{cut} = 20$ km.

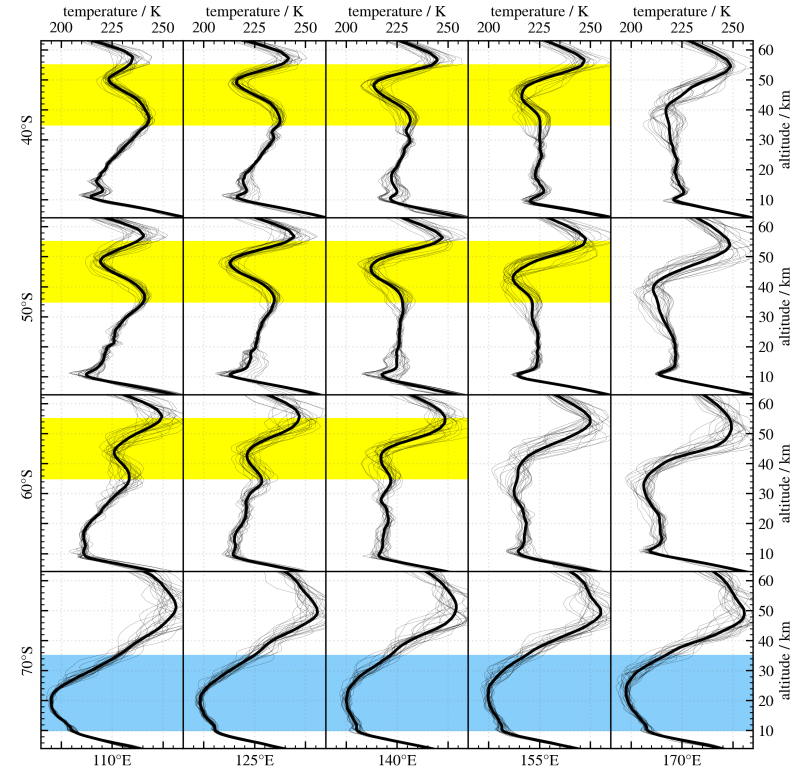

Figure 3. Latitude-longitude matrix of vertical temperature profiles of ERA5 at 20 evenly spaced locations in the Southern Hemisphere. The period July 07, 2014 - July 09, 2014 includes DEEPWAVE research flight RF25. Thick black lines are temporal mean profiles, thin black lines represent individual profiles every 2 h for the 3-day period. The yellow band indicates profiles with a pronounced temperature minimum between 35 and 55 km complicating the application of vertical filters to separate the signal into background and GWs. The blue band marks profiles with a significant temperature decrease in the stratosphere due to the polar vortex.

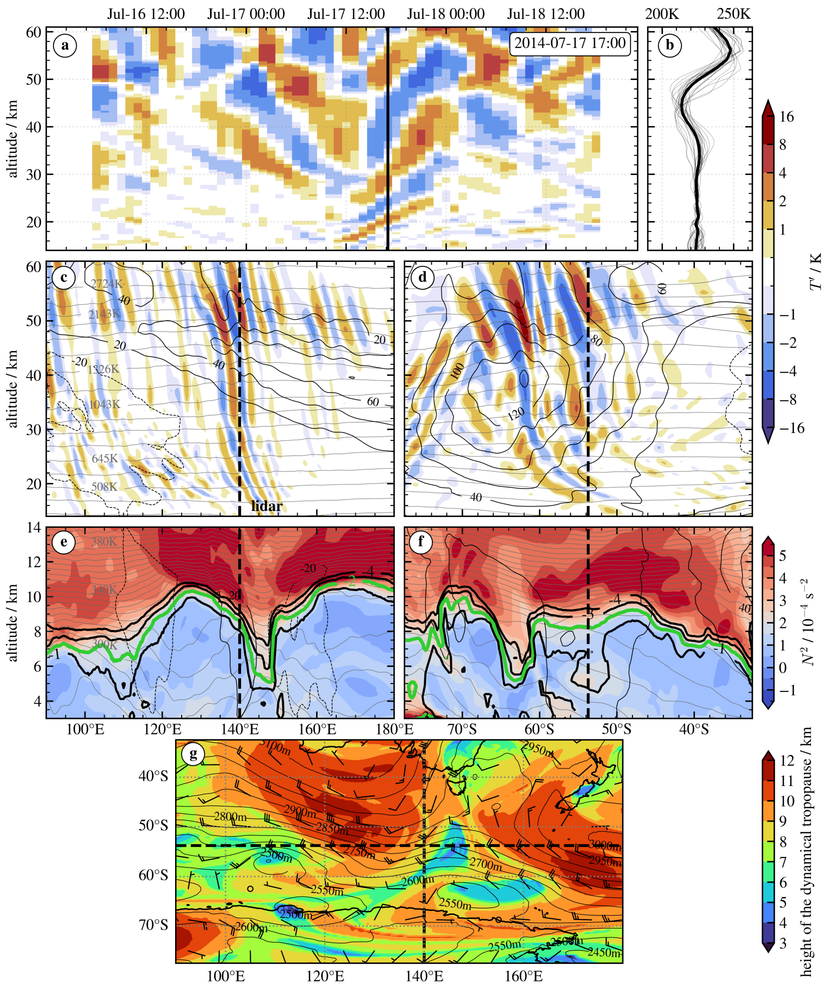

Figure 4. ERA5 overview for a location over the Southern Ocean (53.75°S, 140°E) during research flight RF25 of the DEEPWAVE campaign. Panels (a) and (b) are similar to Figure 2(c) and (d) emulating the measurements of a vertically staring ground-based lidar. Panels (c) and (d) are vertical sections of stratospheric T' along sectors of the latitude circle (c) and meridian (d) of the virtual lidar location. (e) and (f) are corresponding vertical sections of thermal stability N^2 ($10^{-4}\,s^{-2}$, color-coded), potential temperature (K, thin grey lines), and potential vorticity (1, 2, 4 PVU: black, 2 PVU: green) in the vicinity of the dynamical tropopause. Thin black lines in the vertical sections are zonal (d, f) and meridional (c, e) wind components (solid: positive, dashed: negative). Panel (g) is a horizontal section of the height of the 2 PVU surface (km, color-coded), geopotential height (m, solid lines) and wind barbs at the 850 hPa level. The black vertical line in (a) marks the time (July 17, 2014, 17 UTC) for (c)-(g) and dashed lines in (c)-(g) highlight the location of the virtual lidar and profiles in (a) and (b).

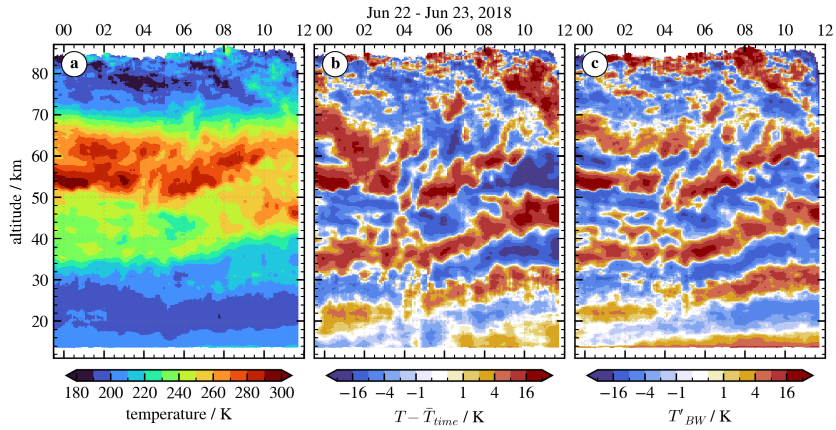

Figure 5. Night-time temperature measurements of CORAL located in Río Grande, Argentina (53.79°S, 67.75°W) from June 22 to 23, 2018. Shown are retrieved temperature profiles (a), temperature perturbations $T' = T - \bar{T}_{time}$ after subtracting a nightly (temporal) mean (b) and T' after applying a vertical high-pass Butterworth filter with a cutoff wavelength of $\lambda_{z,cut} = 20$ km (c).

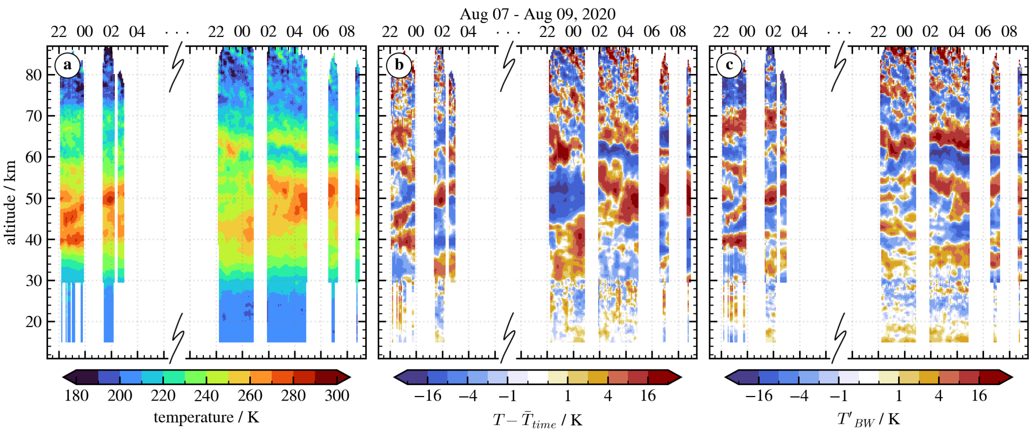

Figure 6. Identical to Figure 5 showing night-time measurements for two consecutive nights from August 7 to 9, 2020. The time frame between the measurements (06:00-20:00 UTC on August 8, 2020) is removed and periods of missing data are related to cloud coverage.

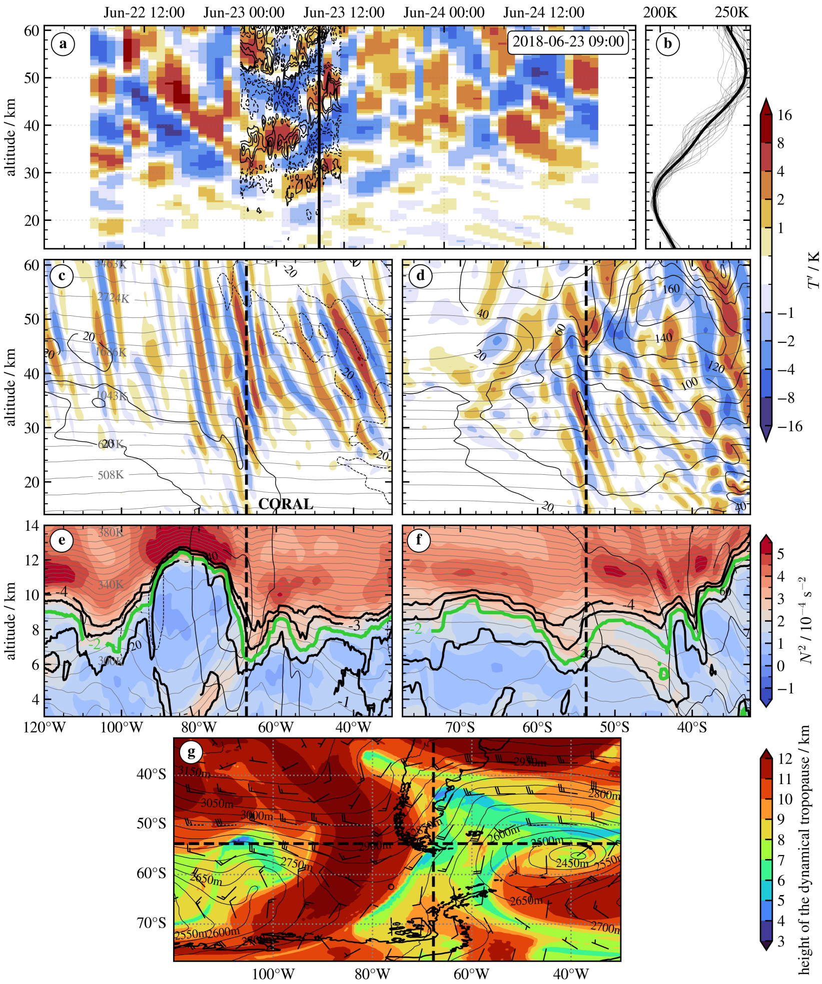

Figure 7. ERA5 overview similar to Figure 4 for CORAL's location and a period around the nightly measurement from June 22 to 23, 2018 in Figure 5. Thin black lines in (a) overlay CORAL observations (solid lines: $T' > 0$, dashed lines: $T' < 0$).

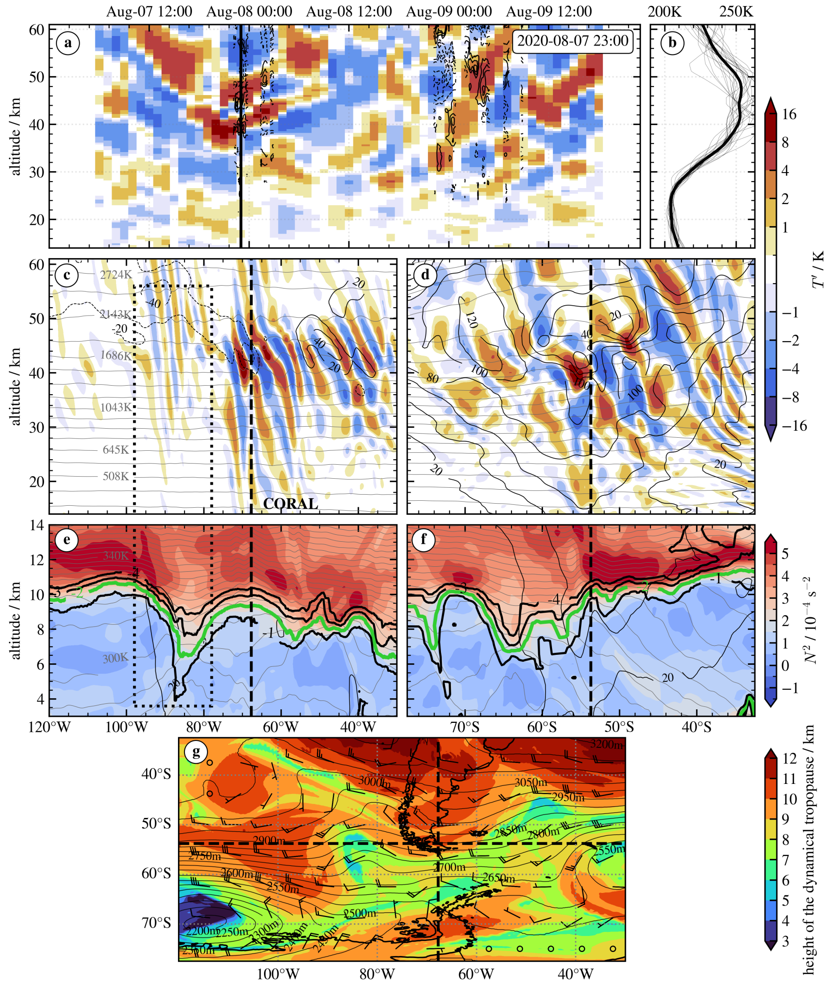

Figure 8. Identical to Figure 7 showing an ERA5 overview for two consecutive nights with CORAL measurements from August 7 to 9, 2020. The dotted rectangle in (c) and (e) frames NOGWs in the stratosphere above an upper-level trough upstream of CORAL's location over the Pacific Ocean.

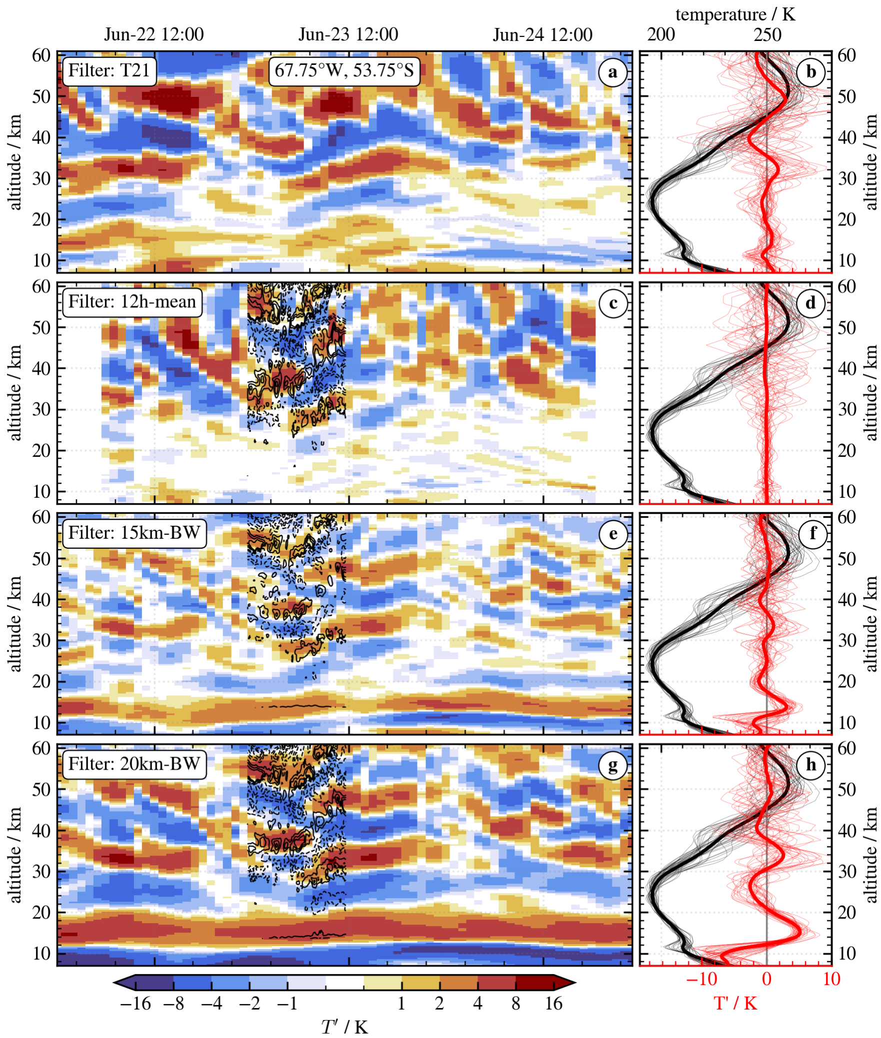

Figure 9. Similar composition as Figure 2 showing time-height diagrams for CORAL's location for a 3-day period in June 2018. Thin black lines show corresponding temperature perturbations from CORAL measurements. Solid lines refer to positive, dashed lines to negative perturbations.

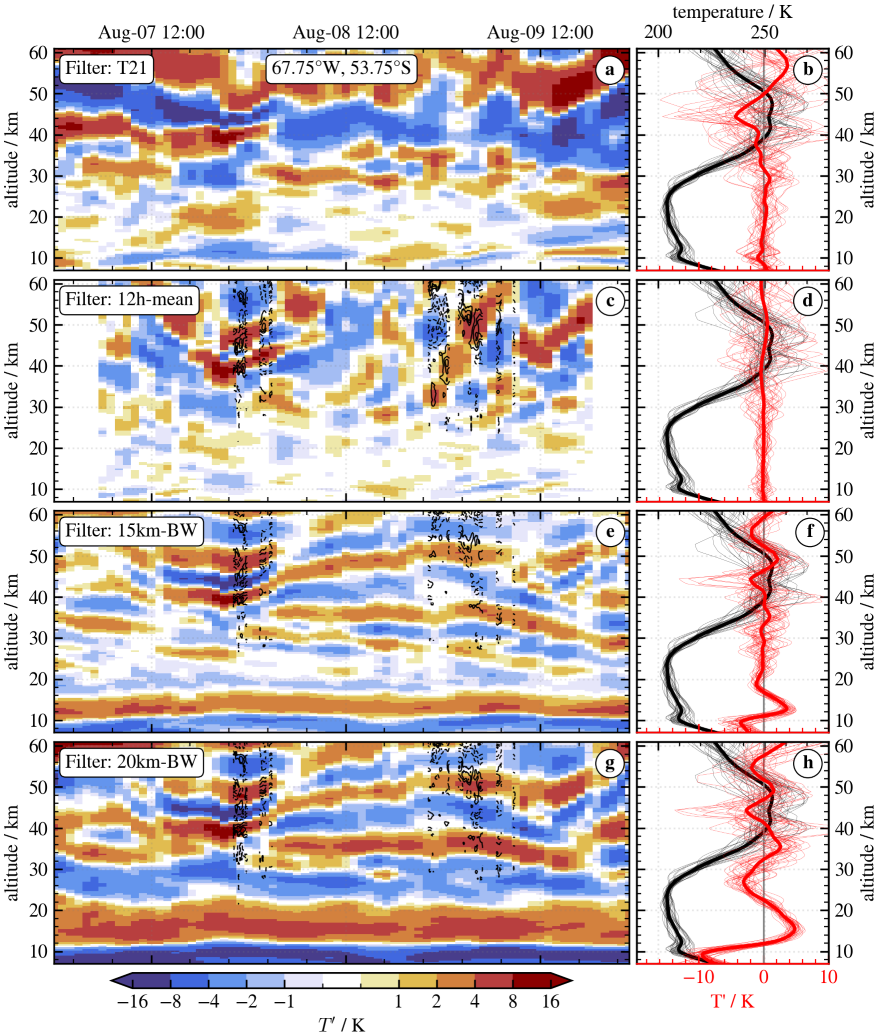

Figure 10. Identical to Figure 9 showing time-height diagrams for CORAL's location for a 3-day period in August 2020 with two consecutive nights with CORAL measurements.